Active Pitch Control of a Vertical Axis Wind Turbine

Enhancing performance in terms of power and loads including dynamic stall effects

D.P. Houf

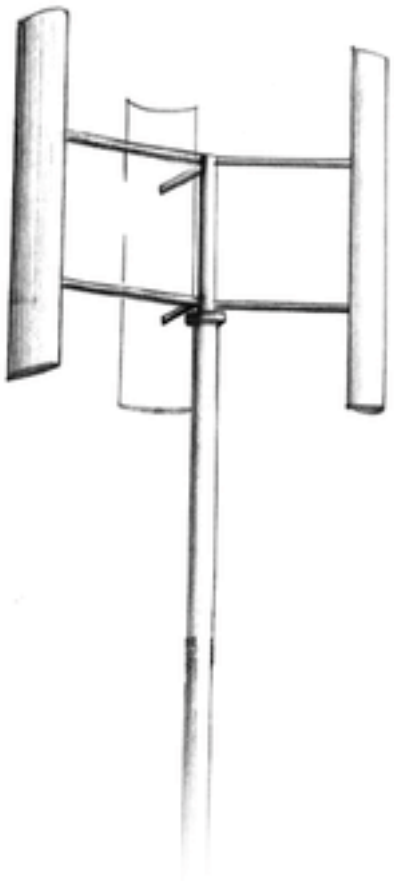

Master of Science Thesis

September 29, 2016

EWEM

TU Delft Delft University of Technology

DTU

Active Pitch Control of a Vertical Axis Wind Turbine

Enhancing performance in terms of power and loads including dynamic stall effects

Master of Science Thesis

For obtaining the degree of Master of Science in Engineering Wind Energy at Technical University of Denmark and in Aerospace Engineering at Delft University of Technology.

D.P. Houf

September 29, 2016

European Wind Energy Master - EWEM
DUWIND - Delft University of Technology
Risø - Denmark Technical University

European Wind Energy Master - EWEM

Rotor Design Track

The undersigned hereby certify that they have read and recommend to the European Wind Energy Master - EWEM for acceptance a thesis entitled **"Active Pitch Control of a Vertical Axis Wind Turbine"** by **D.P. Houf** in partial fulfillment of the requirements for the degree of **Master of Science**.

Dated: September 29, 2016

Supervisor: _____
Dr.ir. Carlos J. Simão Ferreira of TU Delft

Supervisor: _____
Dr. Mac Gaunaa of DTU Wind Energy

Reader: _____
Dr. Richard P. Dwight of TU Delft

Abstract

Due to its inherent dynamic stability the Vertical Axis Wind Turbine (VAWT) is a strong candidate for large (10-20 MW) floating offshore applications. However, there is room for improvement considering the VAWT's aerodynamic and structural performance, so as to increase its cost-effectiveness. This thesis explores the VAWT's potential of enhancing its performance, using active pitch control, in terms of the following three objectives: 1.) power maximization, 2.) power minimization, and 3.) thrust relief. For this purpose the Modified-Linear Actuator Cylinder Model (Mod-Lin ACM) [30][32] is used as optimization tool. Another inherent feature of the VAWT is that its blades experience large angles of attack, and it is believed that dynamic stall effects will play a significant role in the optimization. The quasi-steady aerodynamic force coefficients in the Mod-Lin ACM are therefore replaced by their dynamic equivalents, which are obtained from a Beddoes-Leishman type dynamic stall model [21]. The phenomenon of leading edge separation is modelled separately, as "plug-in" to this dynamic stall model, following the formulation presented in [26]. The analysis in this work is carried out for the symmetrical *NACA0018* airfoil.

The achievable increase of maximum power is only 1%, which is even less when unsteady effects are considered in the optimization. For power coefficients at tip-speed ratios and solidities other than the initial optimum point, increases up to 15% are documented. This implies that values close to the initial maximum power can be achieved for lower solidities, decreasing the total weight, and therefore the cost, of the VAWT. A close correlation between the potentials of power increasal and thrust alleviation is found, which is caused by the fact that local power losses due to thrust relief must be compensated on other peripheral positions. Therefore, in order to obtain the highest trust reductions the optimizer will maximize the local power production on the energy efficient parts of the rotor, similar to the power maximization target. Depending on tip-speed ratio and solidity, the given pitch allowance is able to decrease the power production between 65% and 100%. Generally, the decrement is only enhanced by any occurring unsteady effects. This reveals the potential of using the VAWT's blades as air brake.

Acknowledgements

Throughout this thesis I have had the pleasure of working with two supervisors, Carlos Simão Ferreira from TU Delft and Mac Gaunaa from DTU. I would like to thank Carlos for his help in grasping the concept of VAWTs and his critical perspective on my implementation of the coupled actuator cylinder / dynamic stall model. His insight in the matter has pushed me to critically assess my own results. To an equal extend, a big thank you to Mac for being as involved in this project as possible from Denmark. I have enjoyed the lively conversations over Skype and his creativity has been the inspiration for a lot of topics adressed in this thesis. Additionally, I would like to thank Helge Aagaard Madsen and Sercan Erthem for being very responsive to e-mails. This has helped me a lot, especially, during the implementation of the actuator cylinder model.

Besides demonstrating the work I have done over the past nine months, this document marks the end of my life as a student. I am immeasurably thankful to my mom and dad, Gisela and Hans, for their love and their support both in- and outside of my academic life. To my sister and brother, my girlfriend and all of my friends: Thank you.

Delft, The Netherlands
September 29, 2016

D.P. Houf

Contents

List of Figures

List of Tables

Nomenclature

Latin symbols

a	Induction factor
α_0	Zero-lift angle of attack
a_d	Downwind induction factor
a_u	Upwind induction factor
$A_i,\ b_i$	Geometry dependent constants
B	Number of blades
c	Chord length
C_T	Thrust coefficient
C_P	Power coefficient
C_{Pi}	Ideal power coefficient
C_d	Drag coefficient
C_d^{dyn}	Dynamic drag coefficient
C_d^{st}	Quasi-steady drag coefficient
C_l	Lift coefficient
$C_{l,\alpha}$	Slope of lift polar
C_l^{dyn}	Dynamic lift coefficient
$C_l^{\mathrm{dyn,tot}}$	Total dynamic lift coefficient including leading edge separation effect
C_l^p	Lift coefficient for unsteady attached flow
C_l^{st}	Quasi-steady lift coefficient
$C_{l,v}$	Lift coefficient increment due to leading edge separation
ΔC_l	Difference between C_l^{dyn} and C_l^p
f	Nondimensional distance between leading edge and separation point
$f_{\Delta Q_n}^{\mathrm{local}}$	Local allowance for loadform deviation from reference
$f_{\Delta Q_n}^{\mathrm{global}}$	Global allowance for loadform deviation from reference
F_n	Normal blade force
F_t	Tangential blade force
k	Reduced frequency

k_a	Induction-based correction factor used in the Mod-Lin ACM
m	Arbitrary exponent for analytic loadform creation
N	Number of control points along the rotor periphery
Δp	Pressure jump over actuator cylinder surface
Q_n	Nondimensional normal rotor loading
Q_t	Nondimensional tangential rotor loading
R	Rotor radius
R_{w_x}	Axial induction influence coefficient
R_{w_y}	Lateral induction influence coefficient
Re	Reynolds number
t	Time
Δt	Time step size
T_f	Time constant with respect to lag in the boundary layer
T_p	Time constant with respect to pressure
T_u	Time constant with respect to velocity
U	Velocity
V_∞	Free-stream velocity
$V_{\infty,d}$	Downwind inflow velocity
V_n	Normal velocity
V_r	Relative velocity
V_t	Tangential velocity
w_x	Axial induction velocity
w_y	Lateral induction velocity
x_i	The i^{th} aerodynamic state variable

Greek symbols

α	Angle of attack
$\dot{\alpha}$	Angle of attack rate
$\alpha_{(3/4)}$	Angle of attack at three-quarter chord length
α_E	Effective angle of attack
α_s	Angle of attack at which stall starts
α_v	Angle of attack at which leading edge vortex passes the trailing edge
Γ	Bound vorticity strength
θ	Azimuthal position
θ_p	Pitch angle
$\theta_{p,range}$	Allowance on pitch angle
λ	Tip-speed ratio
τ	Nondimensional parameter indicating the location of the travelling leading edge vortex
τ_p	Nondimensional time constant with respect to pressure
τ_f	Nondimensional time constant with respect to the lag in the boundary layer
ϕ	Indicial response function
ω	Rotational velocity
ω_a	Airfoil's angular frequency
$\Delta\theta$	Shift in azimuthal position
σ	Rotor solidity

Abbreviations

ACM	Tip-speed ratio
B-L	Angle of attack
CFD	Computational Fluid Dynamics
CoE	Cost of Energy
DES	Detached Eddy Simulation
DNS	Direct Numerical Simulation
HAWT	Horizontal Axis Wind Turbine
LES	Large Eddy Simulation
L-N-K	Larsen-Nielsen-Krenk
Mod-Lin	Modified-linear
N-S	Navier-Stokes
(U)RANS	(Unsteady) Reynolds-Averaged Navier-Stokes
S-G-C	Sheng-Galbraith-Coton
VAWT	Vertical Axis Wind Turbine
VT	Vorticity Transport

Chapter 1

Introduction

As stated by the European Wind Energy Technology Platform, there is a serious need for decreasing the Cost of Energy (CoE) of large floating offshore wind farms through advanced and innovative rotor design [13]. The European Wind Energy Association (EWEA) included the development of very large scale wind turbine design in their strategic technology area list for 2020 [12]. Contrary to a Horizontal Axis Wind Turbine (HAWT), the center of gravity of a Vertical Axis Wind Turbine (VAWT) is close to the ground, the center of rotation coincides with the turbine's geometric center, and the blades experience less fatigue loading due to gravity. Furthermore, manufacturing and maintenance are relatively easy. Due to these inherent features, interest in the VAWT concept has regained for large offshore applications in the future [46]. On the other hand, the fact that VAWT blades have a low power production at some azimuthal positions (and therefore a low turbine efficiency), relatively large aerodynamic fatigue loads and create noise polution, are some of the reasons that the HAWT concept has achieved a higher commercial succes so far. However, it is believed that the VAWT's aerodynamic performance can potentially be increased significantly through innovative airfoil design and circulation control, making it a realistic competitor.

Circulation control of a wind turbine can be executed with various objectives in mind, such as maximizing power output or minimizing the cyclic loading encountered by the blades. Currently applied circulation control systems are active/passive pitch and flap control, where the former has widely been used already in the context of HAWTs. It must be kept in mind, however, that pitching of these increasingly large offshore wind turbine blades sets serious demands on the actuation system and could result in very large response times. On the other hand, active flap control, which has mostly been circumvented due to the increased blade complexity, would reduce the required actuation force and response times. However, actuation systems and blade inertias are not taken into account in this thesis project, as the focus is on optimization of the 2D case.

The main target of this thesis project is decreasing the CoE of a VAWT using active pitch control. In doing so, optimum pitch sequences will be derived for the following three objectives: 1.) power maximization, 2.) power minimization and 3.) thrust reduction.

The first objective is set to have the turbine produce more power under the same rotor geometry and operational conditions. This objective therefore directly decreases the CoE of the VAWT. The second objective is chosen to explore the VAWT's capabilities in reducing its power when it exceeds the generator's rated value. The third objective aims at increasing the VAWT's (fatigue) life and therefore also decreases the CoE.

The Actuator Cylinder Model (ACM), as derived by Madsen [30], will be used to carry out the analysis. A description of its implementation, as well as an elaboration on the model's characteristic results, is presented in Chapter 3. The ACM on its own does not take into account unsteady aerodynamic effects that might result from the large angles of attack encountered by the airfoil. For this purpose, a simplified form of the Beddoes-Leishman (B-L) dynamic stall model, derived by Hansen et al. [21], will be implemented as a submodel to the ACM. The effect of leading edge separation will be modelled seperately according to the formulation of Larsen et al. [26]. Dynamic modelling of the aerodynamic force coefficients as well as incorporating this subroutine within the ACM will be the subject of Chapter 4. The implemented ACM will then be used as optimization tool for the three objectives mentioned. First, the maximum design potential of the VAWT is explored by optimization of ideal rotor performance in Chapter 5. Second, the impact on the optimization of having a realistic airfoil polar, including viscosity and drag, will be investigated in Chapter 6. Finally, this chapter will also assess the impact of replacing the quasi-steady lift and drag coefficients by their dynamic equivalents throughout the optimization. Self-evidently, this final section will provide the most realistic optimization results, since it includes both viscous and unsteady aerodynamic effects.

1.1 Research question and aim

Research question: What are the optimum active pitch sequences for a VAWT in terms of aerodynamic performance and load reduction?

1. What are the purposes that circulation control can be used for? And can it be used for multiple purposes simultaneously?
   (a) What kind of tasks can be executed with pitch control?
   (b) What are the limitations of an active pitch control system?
   (c) What is a proper methodology to obtain optimum pitch sequences?
2. Which aerodynamic models are appropriate for analyzing the VAWT's performance for various pitch sequences?
   (a) What are the assumptions behind the existing aerodynamic models? And can they be justified for the current application?
   (b) How are the existing models classified in terms of fidelity and computational effort?
3. Do the effects of dynamic stall significantly influence the operational window for pitch control of a VAWT?

   (a) What are the effects of dynamic stall on a VAWT?
   (b) How do the various existing models treat the dynamic stall effects?
   (c) Does the chosen model sufficiently treat dynamic stall effects?

4. Are the existing dynamic stall models directly implementable to existing engineering models for the VAWT?

   (a) What are the characteristic flow phenomena of the VAWT?
   (b) How significant are these phenomena compared the assumed flow conditions of the dynamic stall model?
   (c) Can these flow phenomena be accounted for by the dynamic stall model through relatively simply modifications?

Research aim: The main goal of the project is decreasing the VAWT's CoE by active pitch control.

1. Update the ACM by implementing unsteady effects. For this purpose, a combination of the Risø model and the L-N-K model will be utilized.
2. Verify the impact of unsteady effects on the solution of the ACM.
3. Utilize the ACM to find optimum pitch sequences in terms of the various objectives.
4. Investigate whether the ACM can be utilized for simultaneous optimization of multiple purposes.
5. Verify the performance of the pitch control sequences against a higher-fidelity model.

1.2 Methodology

The current section will provide a brief overview of the various methodologies introduced and applied in this thesis. It will serve as a brief overview and the reader is referred to the corresponding chapters for a more detailed elaboration.

- Chapter 2: Review of literature in order to gain knowledge about relevant background theory and existing research projects, as well as establish a clear purpose for the work to be carried out.
- Chapter 3: Investigate the performance and aerodynamic characteristics of a VAWT with infinite number of blades, i.e., the Actuator Cylinder.
  - Implement the modified-linear (Mod-Lin) Actuator Cylinder Model (ACM) in Matlab according to the formulation of Madsen et al. [32]. A qualitative comparison of results will serve as validation of this implementation.
  - Use the implemented model to compute the power and thrust curves as well as the local behaviour of relevant aerodynamic quantities along the rotor's circumference - such as the angle of attack, relative velocities and blade loadings.

- CHAPTER 4: Replace the quasi-steady lift and drag coefficients in the Mod-Lin ACM by their dynamic equivalents and analyze the effects of unsteady aerodynamic phenomena on the results.
  - Implement a Beddoes-Leishman type dynamic stall model, an indicial formulation of which is given by Hansen et al. [21]. Validate against results from HAWC2.
  - Implement the effect of leading edge separation, according to Larsen et al. [26], as "plug-in" to the Beddoes-Leishman implementation. A qualitative comparison of results will serve as validation.
  - Couple the implemented dynamic stall model to the Mod-Lin ACM, in such a way that the user has the following options for flow conditions: 1.) steady flow, 2.) unsteady attached flow, 3.) unsteady attached flow and trailing edge separation, and 4.) full dynamic stall model.
  - Investigate the effects of various unsteady phenomena on the VAWT's performance for different geometries and operational conditions.
- CHAPTER 5: Explore the potential of enhancing ideal rotor performance (thus not taking into accounts tangential loading, viscosity and unsteadt aerodynamics) by optimizing the nondimensional normal load distribution Q_n.
  - Implement a numerical optimizer (`fmincon`) that uses the reference loading Q_n from the Mod-Lin ACM to create an optimum load distribution, referred to as the *loadform*, for the various optimization targets. The allowance on the deviation from the reference Q_n is user-defined.
  - Analyse the derived loadforms and use them to inversely obtain the corresponding pitch sequences. Check the pitch sequences for feasibility.
- CHAPTER 6: Explore the potential of a rotor under realistic flow conditions, including effects of tangential loading, viscosity and unsteady aerodynamics.
  - Implement a numerical optimizer (`fmincon`) that searches ideal pitch sequences for the various optimization targets. In order to ensure continuous, periodic pitch curves a 10^{th} order Bezier curve is used as optimization tool.
  - Analyze the resulting pitch sequences and rotor loadings, and draw conclusions with respect to optimum design points.
  - Compare the results of the quasi-steady ACM to those with dynamic load coefficients and analyze the local and global impact of unsteady aerodynamics on the optimization.

Chapter 2

Literature Review

This chapter will present an overview of relevant background theories and research considering VAWTs and their (unsteady) aerodynamics. Focus will first be on understanding the VAWT's working principles in terms of geometry and energy conversion. Second, the various unsteady phenomena that are inherent to the layout and operation characteristics of the VAWT will be adressed and described, with a primary focus on dynamic stall. Third, a more in-depth description of various existing dynamic stall models will be presented. Last, a trade-off between the various existing aerodynamic models for VAWTs will be made. The chosen model will serve as analysis and optimization tool for the remainder of the thesis.

2.1 Working principles of the VAWT

In this brief first section, various VAWT layout possibilities will be given, together with their main advantage and disadvantage. Additionally, the energy conversion of Darrieus-type (lift-driven) VAWT's will be explained.

2.1.1 Types and layout

There are two types of modern-day VAWTs, which are the Savonius- and Darrieus-type turbine. The Savonius turbine is a drag-driven machine, consisting of two open half drums attached to a central rotating shaft in opposite direction. Due to its low power coefficient this type of wind turbine is mostly used for wind speed measurements [22]. The Darrieus VAWT is lift-driven and consists of two or more airfoil-shaped blades, which can either be curved or straight, attached to a central rotating shaft. Its power coefficient is higher than that of the Savonius type, making the Darrieus concept more applicable for the purpose of power generation. The remainder of this Literature Review will therefore solely focus on the Darrieus-type VAWT. The VAWT concepts are illustrated in Figure 2.1.

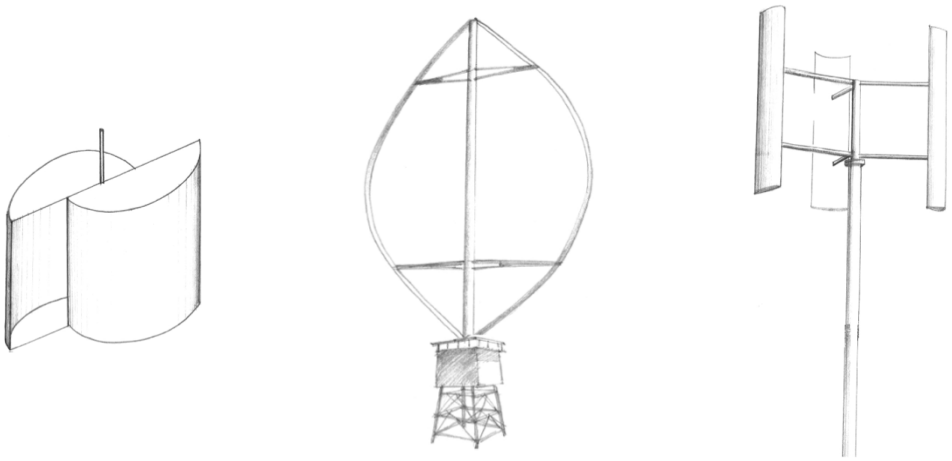

(a) *Savonius-type* (b) *Curved-blade Darrieus* (c) *Straight-bladed Darrieus*

Figure 2.1: *Three modern VAWT concepts [22].*

2.1.2 Energy conversion

The total energy extracted from a VAWT is directly related to its torque, which is a function of the momentary blade loadings caused by lift and drag. An alternative explaination is offered by Ferreira [15], stating that the energy conversion is based on the azimuthal variation of the blade's bound circulation. The continuously varying bound circulation, and therefore the continuous shedding of vortices, is an inherent feature of the VAWT due to its unsteady operation. This implies that the rate of shed vorticity - or, equivalently the generation of the wake - is strongly related to the energy conversion.

Another inherent feature of the VAWT is that the instantaneous 2D blade loadings are decoupled from the rotor's power generation, which was demonstrated by Ferreira and Scheurich [16] for potential flow. This is attributed to the fact that a change in bound circulation simply results in a transer of loading between the upwind and downwind part of the rotor, without changing the overall torque.

2.2 Unsteady aerodynamic phenomena

VAWT aerodynamics requires modelling of unsteady aerodynamics due to large variations in relative wind speed and angle of attack. It is therefore expected that unsteady aerodynamic effects have a significant impact on airfoil forces and moments. This section will highlight the main unsteady aerodynamic phenomena that will be encountered by a VAWT blade in operation.

2.2.1 Dynamic stall

A major flow phenomenon that is typical for the unsteady aerodynamics of a VAWT is dynamic stall. Specific dynamic stall models have therefore been developed in the past, some of which will be discussed in Section 2.3. The name *dynamic stall model* can be

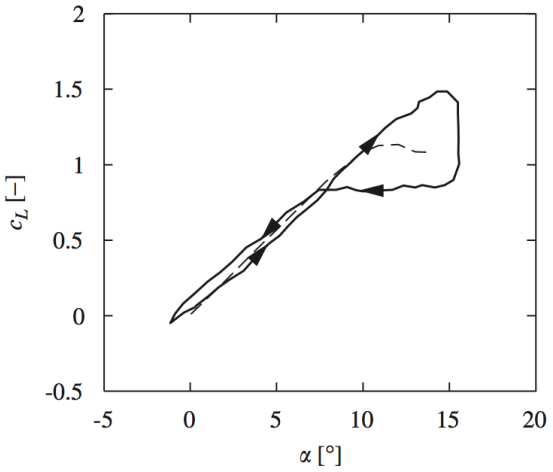

Figure 2.2: *Lift coefficient as a function of angle of attack under static (- -) and dynamic (—) stall conditions [27].*

confusing, since these models do not calculate stall-related phenomena only. In this thesis, a dynamic stall model is built up of three submodels: one for unsteady attached flow, one for an airfoil experiencing trailing edge separation, and one to account for leading edge separation effects. The typical *dynamic stall effect* is characterized by a coupling between trailing edge separation and the shedding of a leading edge vortex as a result of flow reversal in the boundary layer. This effect will only occur if the angle of attack and its rate is above certain critical airfoil-dependent values. Typical for dynamic stall is a delay in the onset of flow separation to a higher angle of attack than that for the static case, as can be seen in Figure 2.2. Dynamic stall causes significant differences in aerodynamic forces with respect to static stall, potentially even exceeding structural fatigue limits. The complete dynamic stall process of an airfoil is visualized in Figure 2.3b and is interaction between unsteady attached flow, trailing edge separation and leading separation, which will be treated seperately in the subsequent paragraphs. The effect of leading edge separation occurs once a critical angle of attack rate is met and takes place in the following four stages:

1. Onset of leading edge separation;
2. Formation of the leading edge vortex;
3. Convection of the leading edge vortex and formation of the trailing edge vortex;
4. Breakdown of the leading edge vortex.

Once leading edge separation is initiated it immediately becomes the dominant unsteady effect, i.e., it directly overtakes the effect of trailing edge separation that occured just before.

Attached flow

The unsteady aerodynamic lift force of an harmonically pitching and plunging airfoil in attached flow is approximated using Theodorsen Theory, which divides the lift in a

circulatory part and a non-circulatory part due to acceleration of the air mass [42]. A slight change in angle of attack will result in a change in bound circulation of the airfoil, which in its turn will change the lift force. The delay of the change in lift follows from a characteristic response function $\phi(t)$. For a thin profile in incompressible flow $\phi(t)$ takes the form of Wagner's indicial response function, implying that half of the increment is felt instantaneously, i.e. $\phi(0) = \frac{1}{2}$, and the full response shows after a certain time delay, depending on the geometry variables A_1, A_2, b_1, b_2 according to

$$\phi(t) = 1 - A_1 \mathrm{e}^{-b_1 t} - A_2 \mathrm{e}^{-b_2 t}. \tag{2.1}$$

According to Bergami et al. [4] airfoil thickness and trailing edge angle influence the terms A_i, b_i and therefore $\phi(t)$. However, it was shown that deviations from the thin airfoil approximation remain insignificant for wind turbine applications.

Trailing edge separation

Stall is a 2D airfoil phenomenon which describes the decrease in lift after a certain angle of attack, due to the loss of circulation caused by flow separation. The degree of stall is characterized by the separation point f, indicating the distance from the LE on the suction side of the airfoil where separation starts. There exists a delay for nonstationary flow conditions with respect to stationary conditions as the separation angle takes some time to approach its stationary value. Due to this delay the generated lift in the nonlinear regime is higher for increasing than for decreasing angles of attack, as is visible in Figure 2.2. It is also observed that this nonstationary effect is significantly smaller and reversed for attached flow. The nonstationary effect is accounted for by modelling the dynamic separation point f', including the aforementioned time lag.

Leading edge separation

Leading edge separation typically occurs for aggressive pitching of airfoils, where a separation bubble forms near the leading edge on the airfoil's suction side. This is usually followed by the building up of a leading edge vortex due to flow reversal in the boundary layer. At some point the leading edge vortex detaches, convects downstream, and a trailing edge vortex starts building up. Eventually, the trailing edge vortex detaches and the detached leading edge vortex breaks down. These stages are indicated on the polar in Figure 2.3a and visualised in Figure 2.3b. Research of Leishman [27] has pointed out that the sudden forward movement of the separation point introduces an extra suction force and therefore an increase in linear lift, which is visible in Figure 2.2. It is assumed that the lift coefficient follows the linear lift profile as long as the leading edge vortex is attached to the profile and thus an additional lift contribution is provided.

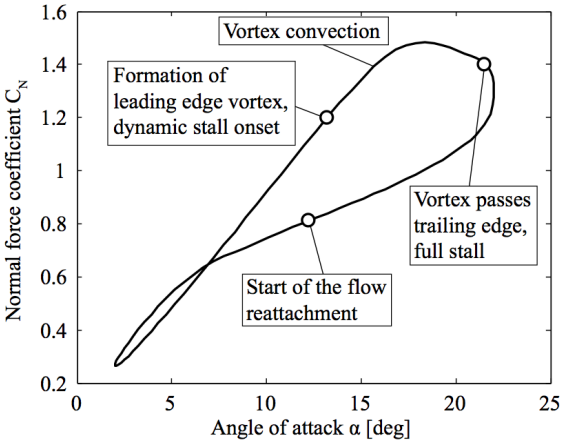

(a) *Normal force coefficient for periodically pitching NACA0021 airfoil [10].*

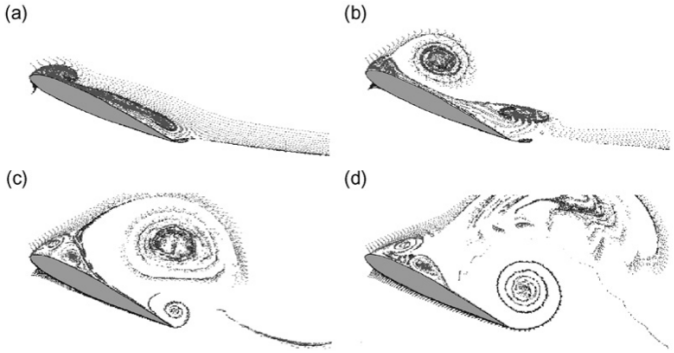

(b) *CFD calculation of NACA-0015 airfoil under dynamic stall conditions [45].*

Figure 2.3: *The dynamic stall process: Figure 2.3b(a) shows the onset of leading edge separation, Figure 2.3b(b) illustrates the formation of the leading edge vortex, the dynamic stall onset, Figure 2.3b(c) shows leading edge vortex convection and formation of the trailing edge vortex and Figure 2.3b(d) shows the leading edge vortex passing the trailing edge and breaking down.*

2.2.2 Flow curvature

An inherent phenomenon to the aerodynamics of a VAWT is that of flow curvature, which arises due the blade's rotation around an offset center. The airfoil therefore not only prescribes a translational, but also an added rotational motion, encountering curvilinear streamlines that cause a chordwise variation in angle of attack. An analogy is often made between the geometric airfoil subject to flow curvature and a virtual cambered airfoil in rectilinear flow. This analogy is shown in Figure 2.4. Migliore et al. [33] investigated the effects of flow curvature by means of this virtual airfoil and found that the added camber and added angle of incidence will result in a shift of the lift curve, respectivily, upward and to the left. Furthermore, the minimum drag coefficient of a symmetrical airfoil in orbit is not experienced at a geometric angle of attack of zero degrees, which is indeed typical for a cambered airoil. According to Migliore et al. [33] the amount of flow curvature influence is strongly dependent of the chord-to-radius ratio c/R.

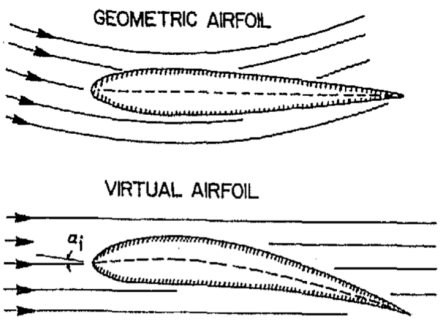

Figure 2.4: *Virtual airfoil approximation [33].*

2.2.3 Blade-wake interaction

Due to its geometry, blade-wake interaction is an inherent feature for any type of VAWT. For a one-bladed VAWT, the blade in the downwind part crosses the wake it has shed in the upwind part. For the more commonly used two- or three-bladed VAWT, a blade can cross both its own wake and the wakes shed by other blades. The process of blade-wake interaction is comprised of the following to two physical processes: (1.) the generation of a wake in the upwind part and its convection downstream, and (2.) the rotational speed of the rotor. The ratio of wake convection to rotor speed determines the amount of wakes crossed by the blade, so the amount of blade-wake interactions in a single revolution is dependent of the tip-speed-ratio λ and the upwind axial induction factor a_u. Ferrer and Willden [17] exploited this idea and analytically derived blade-wake interaction limits in terms of certain λ-values.

Scheurich et al. [37] investigated the effect of blade-wake interaction on the aerodynamic angle of attack and airloads. It was found that blade-wake interaction enhances unsteady flow phenomena in the downwind part of the rotor as it causes sudden changes in local blade loads. These impulsive forces decrease the aerodynamic performance and the fatigue life of the blade. Furthermore, blade-wake interaction can cause transients in local angle of attack which can initiate a local dynamic stall process.

2.3 Models for dynamic stall

Dynamic stall was first identified in helicopter rotor aerodynamics and current applied models are adapted from this industry. Some of these models are empirical, as they are a form of resynthesis of unsteady load measurements on 2D oscillating airfoils in wind tunnel experiments [28]. Pure resynthesis methods are the UTRC α, A, B method, described by Carta and Ham [8] and Bielawa [6], and the Boeing-Vertol "Gamma" Function method, developed by Gross and Harris [20] and Gormont [19]. Other models for dynamic stall are semi-empirical, only partly relying on experiments in the form of empirical coefficients that appear in the physical equations for aerodynamic quantities. These include Beddoes' Time-Delay method [1], Gangwani's method [18], Johnson's method [23], the ONERA method [44] and the Beddoes-Leishman method [29].

All of the above-mentioned methods have initially been developed for helicopter rotor applications. Wind turbine airfoils are thicker than those of helicopter rotors and, moreover, wind turbine rotors operate at significantly lower Mach number and rotational speeds. Since these models are (partly) empirical, they may not be directly applicable for wind turbine airfoils. The most general of the methods is the Beddoes-Leishman method, aiming to provide a complete physical representation of unsteady aerodynamics at relatively low computational cost. Another widely used dynamic stall model is the Gormont model, which has been adapted by Berg [2] specifically for VAWT applications.

2.3.1 Gormont model

In the Gormont model, initially derived by Gormont [19] in 1973, the influence of the airfoil motion is modelled by computing an effective angle of attack. This effective angle of attack

is obtained by correcting the geometric angle of attack with the gamma function. This gamma function is a function of Mach number and empirically determined from oscillating airfoil tests. The reference angle of attack is then used to calculate the dynamic airloads. By using the effective angle of attack, the onset of dynamic stall is delayed to higher angles of attack for increasing pitch rates [28]. Figure 2.6, taken from a comparative study of the Gormont and B-L model by Dyachuk and Goude [10], illustrates the accuracy gained by using a Gormont model compared to using no dynamic stall model.

2.3.2 Beddoes-Leisman model

The complete B-L model, initially derived by Leishman and Beddoes [29] in 1989, is comprised of four submodels: (1.) a non-linear attached flow model, (2.) a non-linear trailing edge separation model, (3.) a dynamic stall onset model and (4.) a model for the vortex induced airloads [28]. The submodels are connected as shown in Figure 2.5. Loads in the linear flow regime are obtained from indicial response functions, taking into account compressibility effects. Non-linear airloads follow from the separation point, which is calculated from the angle of attack using Kirchhoff flow theory [43]. Dynamic stall effects are modelled by taking into account the dynamic effects of a concentrated leading edge vortex that convects downstream along the upper surface of the airfoil. The dynamic stall process is initiated when an equivalent leading edge pressure parameter exceeds a certain critical value. The vortex lift accumulation, as well as the breaking down of this vortex, is handled through a first-order dynamic system with an empirically derived time constant. In Figure 2.6 it is shown qualitatively that the B-L model outperforms the Gormont model. For a more detailed comparison of the B-L model with the Gormont model the reader is referred to Dyachuk and Goude [10].

The models by Sheng et al. [38], Hansen et al. [21] and Larsen et al. [26], presented in the subsequent paragraphs, are all adaptions from the B-L model. The S-G-C model is a modification for low Mach numbers, whereas the Risø and L-N-K models are simplifications with respect to leading edge separation and compressibility.

Sheng-Galbraith-Coton model

In conjunction with University of Glasgow, Sheng et al. [38] found that the original B-L model performs less well in reconstructing unsteady airloads at low Mach numbers than at high Mach numbers. To overcome this, modifications in the Sheng-Galbraith-Coton (S-G-C) model are made with respect to the stall onset criterion, return from stall modelling, the chordwise-force formula and dynamic vortex modelling. In a paper by Dyachuk et al. [11] three versions of the B-L dynamic stall model are presented and evaluated for VAWT operational conditions. These include the original Beddoes-Leishman model, a third generation version of the original model, and the S-G-C model. It was found here that the S-G-C model showed the most accurate results for a VAWT due to its modifications for low Mach numbers.

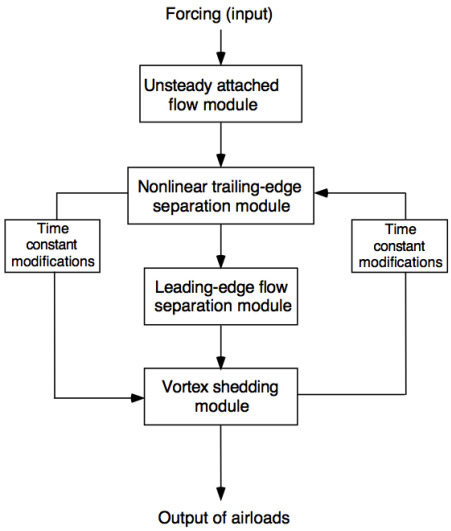

Figure 2.5: *Flow chart of Beddoes-Leishman dynamic stall model [28].*

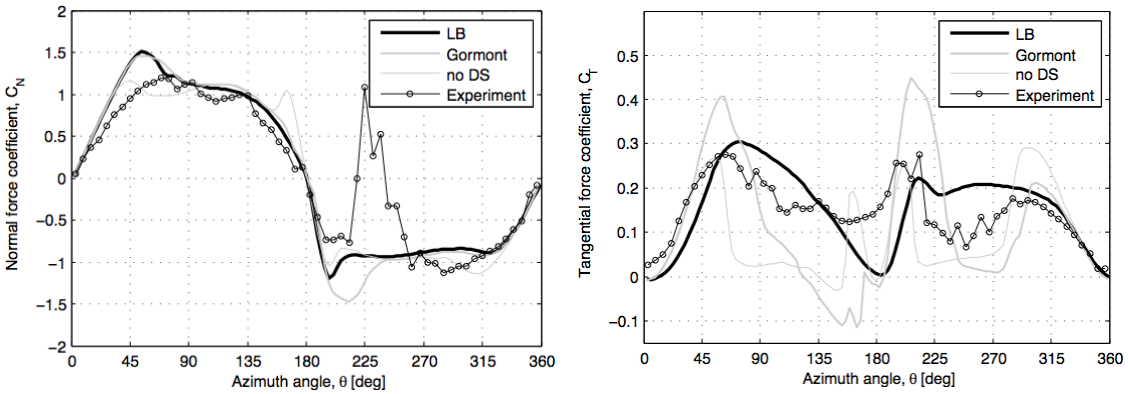

(a) *Normal force.* (b) *Tangential force.*

Figure 2.6: *Comparison of B-L, Gormont, no DS and experimental force response at a tip speed ratio of 2.20 [10].*

Risø model

The Risø model is a simplified version of the B-L model, originally intended for horizontal axis wind turbine aeroelasticity. Due to a relatively low maximum tip-speed ratio ($70 - 80\ m/s$), relatively small oscillations of the angle of attack, and the usage of relatively thick airfoils ($> 15\%$) on wind turbines, the model is simplified by assuming incompressible flow and neglecting the effects of LE separation and vortex shedding. However, next to the simplifications, the B-L model is extended to account for the unsteady lift due to the variable flow velocity for a lead-lag vibrating airfoil, since this effect is typical for wind turbines and was not included in the original model. The Risø model uses a total of four aerodynamic state variables: two to model the unsteady lift for attached flow (b_1, b_2) and two to model the dynamics of trailing edge separation (b_3, b_7).

Larsen-Nielsen-Krenk model

Contrary to the Risø model the L-N-K model does not ignore unsteady effects due to LE separation. Larsen et al. argues that wind turbine blades get increasingly slender, hence LE separation is becoming a more dominant player and must be taken into account. Since the L-N-K model is developed mainly with wind turbine flows in mind, compressibility effects are still omitted. The L-N-K model can therefore be regarded as an extension of the Risø model, including an extra state variable (b_4) describing the diminishing rate of the vortex lift for angles of attack higher than the criticle angle α_v. However, the L-N-K model only uses one state variable to model the dynamics of trailing edge separation (b_3). In the paper by Larsen et al. [26] it is demonstrated that the L-N-K model performs equally well or even better than more complicated models like the full B-L and ONERA model, both under fully attached flow and dynamic stall conditions.

2.4 Aerodynamic models for VAWTs

This section will elaborate on various aerodynamic models that estimate the VAWT's performance. A brief explaination of their working principle will be provided and their advantages and drawbacks with respect to VAWT application will be discussed and compared.

2.4.1 Blade element momentum models

Blade element momentum (BEM) models are commonly used for estimating the aerodynamic performance of VAWTs. BEM theory, mainly established by Betz and Glauert in 1935, is a combination of blade element theory, where the blade is discretized into elements for which the local aerodynamic forces are calculated, and momentum theory, where the rotor is modelled as an infinitely thin actuator disk, with body forces, across which momentum is conserved. By coupling these theories an iterative process is established where the induction is calculated by balancing thrust forces from the the blade elements and the thrust resulting from the momentum conservation law.

The first applicable BEM model for VAWTs was derived by Templin [41]. Similarly to BEM models for HAWTs, the VAWT is placed inside a single streamtube, within which flow conditions are uniform and momentum is conserved. This model was enhanced by Strickland [39] by dividing the flow into multiple independent streamtubes to account for the non-uniform inflow velocity across the turbine width. Conservation of momentum is then imposed separately on each stream tube, allowing for an arbitrarily chosen inflow variation. The most state-of-the-art and commonly used BEM model for VAWT application is the double multiple streamtube (DMST) model, derived by l. Paraschivoiu [25], which takes into account the difference between the upwind and downwind passes of a blade accross a streamtube. The turbine is divided into an upwind and a downwind part, where the assumption is made that the wake of the upwind part fully expands within the turbine's circumference. The downwind part therefore experiences a reduced free-stream velocity which is equal to the ultimate wake velocity of the upwind part $V_{\infty,d} = V_\infty(1 - 2a_u)$, as calculated from actuator disk theory. However, the effect that the downward part of the rotor has on the upward part is still neglected here.

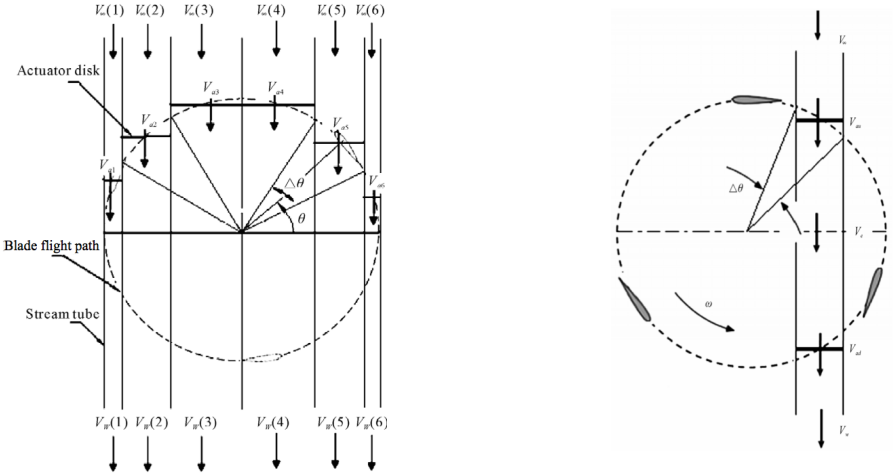

(a) *Multiple streamtube model with six streamtubes divided by a uniform* $\Delta\theta$.

(b) *Double-multiple streamtube model with two actuator disks per streamtube, equilibruim velocity and two induced velocities.*

Figure 2.7: *Schematic of streamtube models [5].*

2.4.2 Actuator cylinder model

The actuator cylinder model (ACM) was derived by Madsen [30] and describes a straight-bladed VAWT as a 2D cylinder surface under radial and tangential volume forces, as shown in Fig. 2.8. The radial forces create a pressure jump $\Delta p(\theta)$ over the cylinder surface, which is used in combination with the relative velocity $V_r(\theta)$ at the cylinder to obtain the power extracted across the surface.

In order to find the relation between $\Delta p(\theta)$ and $V_r(\theta)$ it is assumed that the flow is purely 2D and nonviscous. These assumptions allow the application of the steady-state Euler equations. Introducing perturbation velocities w_x, w_y and subjecting the Euler equations to the equation of continuity, a Poisson-type equation is obtained where the pressure field is balanced by volume forces and induced forces. The perturbation velocities are therefore functions of the prescribed volume forces and the second order induced forces, respectivily referred to as the linear and non-linear solution. The linear solution can be solved analytically whereas the non-linear solution must be solved on a rectangular mesh and is therefore computationally expensive. Madsen et al. [32] found that the shapes of the velocity curves from the linear model and the full model are in good agreement but that the linear model underestimates the induced velocities at high loading. Therefore, the accuracy of the linear model can significantly be increased by amplifying its computed induced velocities as the loading increases. The amplification factor k_a solely depends on the induction factor a and the modified-linear (Mod-Lin) model is iterated until a is fully converged.

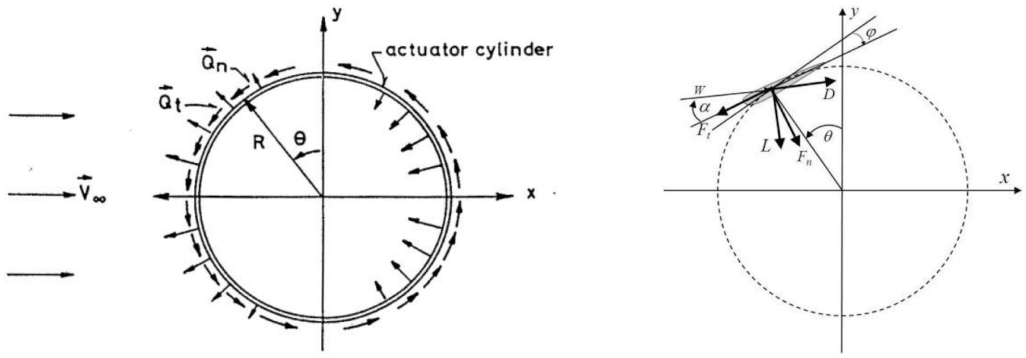

(a) *Definition of the non-dimensionalized volume forces.* (b) *Definition of the blade forces and angles.*

Figure 2.8: *The AC flow model representation of a VAWT [32].*

2.4.3 Vortex models

Prandtl's lifting-line model models the chordwise circulation along the span as a concentrated vortex along a single lifting-line, positioned at the blade's quarter-chord. Following Helmholtz's second theorem, stating that a vortex filament cannot begin or end in a fluid, a closed vortex system is established, consisting of the airfoil's bound vorticity along the lifting line, the trailing vorticity along the wingtips and the shed vorticity in the far wake closing the system. This vortex system is called a horseshoe vortex. Helmholtz's vortex theorems are imposed on the horeshoe vortex and the relation with the lift is found from Kutta-Joukowski theorem. This implies that temporal changes in lift, i.e. temporal changes in bound vorticity, will result in vortex shedding. Induced velocities are found using the Biot-Savart law, which was originally developed to describe the magnetic field generated by an electric current, or vice versa. An analogy is often made between a vortex induced velocity and a magnetically induced current.

A single horseshoe vortex is not a realistic representation of reality since it assumes constant bound vorticity Γ, and therefore constant lift, along the span. Prandtl therefore enhanced this basic system by introducing multiple spanwise horeshoe vortices, allowing for a variable bound vorticity $\Gamma(y)$. The above theorems are then imposed on each individual horseshoe vortex. Prandtl's lifting-line model is visualized in Fig. 2.9 for steady flow, so the influence of the shed vorticity is negligible since it is at a large distance from the trailing edge.

The first commercially developed 3D vortex model for VAWT applications was the VDART3 code, developed by Strickland et al. [40] under contract to Sandia National Laboratories. The VDART3 code was used as a basis by Murray and Barone [34] for the development of the CACTUS vortex method code, taking into account dynamic stall effects by means of a Beddoes-Leishman type dynamic stall model.

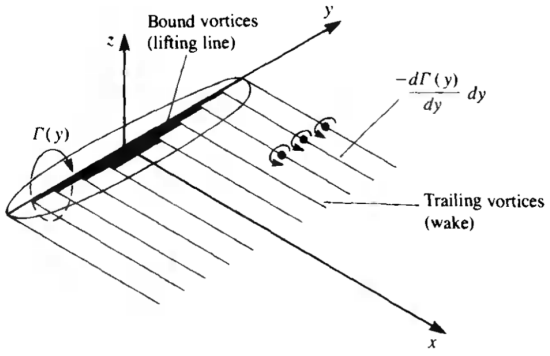

Figure 2.9: *Lifting line model consisting of horseshoe vortices [24].*

2.4.4 Panel models

The lifting-line approach uses thin airfoil theory to approximate the lift on the wing surface. Airfoil thickness is therefore not taken into account. With respect to this issue, the panel method can be viewed as an extension of the lifting-line method as it discretizes the body surface by means of singularity panel elements, which is visualized in Fig. 2.10. Such a panel can arbitrarily be chosen as a source, sink, doublet or vortex panel.

The main assumption behind panel models is that of potential flow, which describes the velocity field as the gradient of the velocity potential Φ. Since potential flow theory allows the superposition of elementary solutions, the airfoil surface can be represented as a sum of source and doublet panels. A unique solution for the velocity potentials is then found by imposing the boundary condition of impermeability and the Kutta condition on each of the surface panels' collocation point. Additionally, in case a lift force is present, modelling the wake strength and shape is necessary to determine the amount of circulation on each of the panels.

Drela [9] developed the semi-empirical XFOIL code, which utilizes an inviscid linear vorticity panel model with a Karman-Tsien compressibility correction in combination with semi-empirical boundary layer equations. More advanced panel codes use a double-wake model, where an additional vortex sheets are created from the point of boundary layer

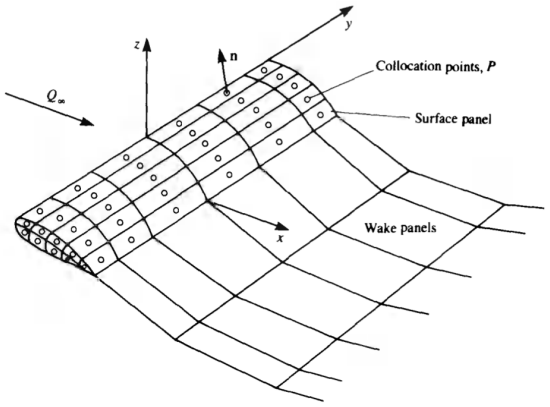

Figure 2.10: *Discretization of the body surface by panel elements [24].*

separation. Such panel codes were developed by Ramos-García et al. [36] and, specifically for the VAWT, by Zanon et al. [47].

2.4.5 Computational fluid dynamic models

Computational fluid dynamics (CFD) models are known as high-fidelity but computationally expensive models. In CFD models a mesh is created of the body and the far-field, which can be done through various discretization methods, i.e. finite volume (FV), finite element (FE) and finite difference (FD). The fundamental basis of each CFD solver then lies in solving the Navier-Stokes (N-S) equations on each mesh element. CFD models are particularly used for quantitative predictions of turbulent flows for engineering purposes. Classification of such turbulence models is based on their refinement, that is the range of turbulence scales present in the model.

The Reynolds-Averaged Navier-Stokes (RANS) model solves a time-averaged version of N-S equations, allowing for Reynolds decomposition of an instantaneous quantity into a time-averaged and a fluctuating part. This decomposition leads to a closure problem, which can be solved by one of the various transport models that have been derived: Prandtl's Mixing Length model, $k-\epsilon$ model and $k-\omega$ model. Time-averaging the N-S equations is favorable in terms of computational cost, but will decrease the accuracy of the model.

Models solving the full N-S equations are Large Eddy Simulation (LES) and Direct Numerical Simulation (DNS). LES filters out the smallest scales of turbulence, which significantly decreases the computational cost, and resolves these scales empirically. DNS solves the full N-S equations down to the Kolmogrov scale and is therefore the most accurate and computationally expensive turbulence model. The computational cost of DNS is determined by the number of grid points in three dimensions and the required number of time steps (as a function of these grid points), hence it scales with Re^4.

Hybrid CFD methods also exist, an example of which is the Detached Eddy Simulation (DES). This model combines the unsteady RANS (URANS) for the region close to the wall with LES for the outer flow solution. Alternatively, a hybrid model between a vortex and a CFD model is formulated by Brown [7]. This model is known as the vorticity transport (VT) model and uses a vorticity-velocity formulation.

2.4.6 Discussion of models

When selecting an appropriate model the engineer has to keep in mind the assumptions behind the model, the model's fidelity and the corresponding computational cost. Tab. 2.1 summarizes these features for the models discussed in this section.

Clearly, BEM models provide inaccurate results for VAWTs when compared to the alternatives. The main reason for this, as mentioned by Madsen [30], is that BEM models are initially designed for HAWTs, only calculating the axial force components. Since tangential force components are of significant influence for VAWTs, BEM models lack fidelity here. The ACM performs better than BEM models, mainly because it models the VAWT as a 2D actuator cylinder instead of a 1D actuator disk. The ACM is not widely used

Table 2.1: *General overview of the various aerodynamic models.*

	Assumptions	**Fidelity**	**Cost**
BEM	– 1D actuator disk – Homogeneous, incompressible, steady flow – DMST: wake fully expands inside cylinder	−	+
ACM	– 2D actuator cylinder – Homogeneous, incompressible, steady flow	−/+	+
Vortex	– Incompressible, inviscid, irrotational flow – Small angle approximation	+	−
Panel	– Incompressible, inviscid, irrotational flow – Small angle approximation	+	−
CFD	– RANS: ensemble averaging – LES: space-filtering	++	−−

yet but it is implemented in the aeroelastic code HAWC2 [32]. Vortex and panel models are an intermediate between ACM and N-S solvers in terms of fidelity. CFD models are very accurate but at the expense of the required computational effort. These models are used to provide an insight in the complex VAWT aerodynamics, including the effects of viscosity and turbulence.

Ferreira et al. [14] carried out a comparative study between six different aerodynamic models for VAWTs, including the BEM, ACM, vortex and panel models. The models were subjected to three cases with varying tip-speed ratio, solidity and fixed pitch angle. An overall conclusion of the study was that BEM models provide inaccurate results, and that correct power and thrust predictions could be attributed to error cancellation. It was found that the MST gives inaccurate results due to its simple induction model. The DMST isolates the upwind from the downwind part of the rotor and is therefore unable to model a zero net effect of adding a constant force. Therefore, the DMST is unable to predict the effect of a changing fixed pitch angle on power, thrust and induction. Additionally, since the DMST assumes full wake expansion within the actuator, it is limited at an upwind streamwise induction factor of 0.5. Results of the other models were in good agreement, except for the ACM's prediction of the power coefficient at high loading. This can be attributed to the Mod-Lin solution becoming less accurate at high loading. A final difference between ACM and the vortex/panel models was observed in the estimated induction factors, since the ACM uses a time-averaged actuator loading and the vortex/panel models consider instantaneous loads.

Chapter 3

Performance of the Actuator Cylinder

This brief chapter describes the implementation of the Actuator Cylinder Model (ACM) as formulated by Madsen [30], which forms the backbone of this thesis. The ACM models the reactional blade loadings in normal and tangential direction, respectivily $Q_n(\theta)$ and $Q_t(\theta)$, non-dimensionalized by rotor solidity and free-stream velocity. The former blade loading Q_n is related to the pressure jump accross the rotor and therefore a key measure for the performance. The tangential blade loading Q_t is related to the drag forces as a result of the airfoil-relative velocity, which equals zero in case of an *ideal rotor assumption*.

First, the implementation procedure of the model will be described. This will be done in a similar fasion to its implementation in *HAWC2*, documented in [32]. Second, the converged solution of the Mod-Lin ACM will be presented and elaborated on. This solution will be refered to as the *reference performance* throughout the optimization in Chapter 5 and 6.

3.1 Implementation procedure

A step-by-step description of the ACM implementation is presented in this section. For a flowchart of the model the reader is referred to Figure 4.5 in Section 4.3. Note that this flowchart includes the option of dynamic modelling of lift and drag coefficients, the implementation of which is the subject of Chapter 4. Definitions and directions of θ, x, y, α, V_r, Q_n and Q_t are given in Figure 2.8.

1. The rotor periphery is divided into N pieces using an uniform spacing $\Delta\theta = 2\pi/N$. The mid-points of those pieces are taken as control points, i.e. (x, y) positions with a corresponding angle θ. To avoid singularities on the periphery the control points are moved slightly in- or outside the actuator cylinder by a scaling factor f. This

way, the control points are defined according to

$$\theta_i = i\Delta\theta - \frac{1}{2}\Delta\theta \tag{3.1}$$

$$x_j = -f\sin(j\Delta\theta - \frac{1}{2}\Delta\theta) \tag{3.2}$$

$$y_j = f\cos(j\Delta\theta - \frac{1}{2}\Delta\theta), \tag{3.3}$$

with $i, j = 1, ..., N$. The index j indicates the control point, the solution of which is a summation of influences of the other azimuthal positions, indicated by index i.

2. The degree by which the loading at azimuthal positions θ_i influences the velocities at control points (x_j, y_j) is described by the influence coefficients R_{w_x}, R_{w_y}, defined as

$$\begin{aligned} R_{w_x}(i,j) &= -\int_{\theta_i - 1/2\Delta\theta}^{\theta_i + 1/2\Delta\theta} \frac{-(x_j + \sin\theta_i)\sin\theta_i + (y_j - \cos\theta_i)\cos\theta_i}{(x_j + \sin\theta_i)^2 + (y_j - \cos\theta_i)^2}\mathrm{d}\theta \\ R_{w_y}(i,j) &= -\int_{\theta_i - 1/2\Delta\theta}^{\theta_i + 1/2\Delta\theta} \frac{-(x_j + \sin\theta_i)\cos\theta_i - (y_j - \cos\theta_i)\sin\theta_i}{(x_j + \sin\theta_i)^2 + (y_j - \cos\theta_i)^2}\mathrm{d}\theta. \end{aligned} \tag{3.4}$$

These influence coefficients depend solely on rotor geometry and the chosen number of control points, and can therefore be calculated outside of the iteration.

3. In this step the local flow conditions are calculated for each azymuthal position and iterated until the solution of the induced velocities has fully converged. The local velocities V_x, V_y - or, equivalently, V_n, V_t - are a summation of the free-stream velocity V_∞, the rotational speed ω and the induced velocities w_x, w_y. From the local velocities, the perceived angle of attack is obtained, from which the non-dimensional forces F_n, F_t and loadings Q_n, Q_t are calculated. The loadings are calculated for all azimuthal positions $i = 1, ..., N$ and multiplied with corresponding influence coefficient to obtain the induced velocities at control point j. The fully converged solution is referred to as the linear solution.

$$V_x = V_\infty + V_\infty w_{x,i} + V_\infty\lambda\cos\theta_i \tag{3.5}$$

$$V_y = V_\infty w_{y,i} + V_\infty\lambda\sin\theta_i \tag{3.6}$$

$$V_n = V_x\sin\theta_i - V_y\cos\theta_i \tag{3.7}$$

$$V_t = V_x\cos\theta_i + V_y\sin\theta_i \tag{3.8}$$

$$V_r = \sqrt{V_n^2 + V_t^2} = \sqrt{V_x^2 + V_y^2} \tag{3.9}$$

$$\alpha = \tan^{-1}\left(\frac{V_n}{V_t}\right) - \theta_p \tag{3.10}$$

$$C_n(\alpha) = C_l(\alpha)\cos\alpha + C_d(\alpha)\sin\alpha \tag{3.11}$$

$$C_t(\alpha) = C_l(\alpha)\sin\alpha - C_d(\alpha)\cos\alpha \tag{3.12}$$

$$F_n(\theta) = 0.5\ \rho\ c\ V_r^2\ C_n \tag{3.13}$$

$$F_t(\theta) = 0.5\ \rho\ c\ V_r^2\ C_t \tag{3.14}$$

$$Q_n(\theta) = B\frac{F_n(\theta)\cos\theta_p - F_t(\theta)\sin\theta_p}{2\pi R} \tag{3.15}$$

$$Q_t(\theta) = B\frac{F_t(\theta)\cos\theta_p + F_n(\theta)\sin\theta_p}{2\pi R} \tag{3.16}$$

$$w_{x,j} = \frac{1}{2\pi}\sum_{i=1}^{i=N} Q_{n,i}R_{w_x}(i,j) + Q^*_{n,j} - Q^{**}_{n,N+1-j} \tag{3.17}$$

$$w_{y,j} = \frac{1}{2\pi}\sum_{i=1}^{i=N} Q_{n,i}R_{w_y}(i,j) \tag{3.18}$$

The star terms in equation (3.17) are added to the calculation of w_x to ensure a continuous solution without velocity jumps across the cylinder surface. If the control point lies inside the actuator cylinder the single star term (*) is added, and if the control point lies in the wake of the actuator cylinder the double star term (**) is added.

4. The linear solution becomes a Mod-Lin solution when the induced velocities are multiplied by correction factor k_a. This correction factor is calculated from the thrust coefficient, which is found from the linear solution. The correction factors are included in the iteration to ensure convergence of the Mod-Lin solution.

$$C_T = \int_0^{2\pi}(Q_n(\theta)\sin\theta - Q_t(\theta)\cos\theta)\mathrm{d}\theta \tag{3.19}$$

$$a = 0.0892C_T^3 + 0.0544C_T^2 + 0.2511C_T - 0.0017 \tag{3.20}$$

$$k_a = \frac{1}{1-a} \tag{3.21}$$

5. When a converged solution is obtained, thrust and power coefficients are calculated. The power coefficient is found by integrating the torque along the rotor's periphery. Resulting power and thrust curves are shown in Figure 3.1. Underlying angles of attack, loads and (induced) velocity distributions are shown in Figure 3.2.

$$C_{Pi} = \frac{\int_0^{2\pi} Q_n(\theta)V_n(\theta)\mathrm{d}\theta}{\rho V_\infty^3} \tag{3.22}$$

$$C_P = \frac{\frac{1}{2\pi}\int_0^{2\pi} B\left(F_t(\theta)\cos\theta_p + F_n(\theta)\sin\theta_p\right)\omega\mathrm{d}\theta}{\rho V_\infty^3} \tag{3.23}$$

6. The converged solution can also be utilized to compute velocity field around the actuator cylinder. The control points (x_j, y_j) in equation (3.4) are replaced by the coordinates of the respective grid points, enabling the induced velocity field to be established. When following a particle along a certain $y-$coordinate that crosses the cylinder surface, the single star term $-Q_n(\arccos y)^*$ is added for all grid points along that line inside the cylinder. When that particle crosses the cylinder surface again, it will be positioned inside the wake and the double star term $Q_n(-\arccos y)^{**}$ is added as well. The nondimensional velocity field is then found fromuti

$$v_x = 1 + w_x \tag{3.24}$$

$$v_y = w_y \tag{3.25}$$

3.2 The converged solution

Two definitions of power are provided in equation (3.22) and equation (3.23). The first corresponds to the power production of an *ideal rotor*, i.e., a rotor with an infinite number of blades and zero tangential loading. The second expression does account for the tangential loadings, consisting out of drag and the tangential component of lift. The power and thrust curves of both an ideal and a real rotor are plotted in Figure 3.1. Note that the ideal C_T is obtained by setting Q_t in equation (3.19) equal to zero.

The Betz limit of $C_P = 0.593$ is clearly approached in the ideal power curve. The power coefficient increases with rotational velocity, and so does the axial induction. When the axial induction factor is closest to 0.33, which happens around a tip-speed ratio of 5.5, the maximum C_P value is obtained. When the rotational speed is increased beyond this optimum point, the axial induction factor further increases and a drop in C_P is whitnessed. Where the ideal power production is limited by its induction factor the real power production is limited by its loads. A maximum value of 0.47 is found at a tip-speed ratio of 3, and decreases for both lower and higher rotational speeds. Due to its definition the thrust is less affected by a non-zero tangential component.

Figure 3.2 shows the behaviour of aerodynamic quantities along the rotor periphery for a $\sigma = 0.1$ rotor. The angle of attack will start at its minimum absolute value at $\theta = 0°$

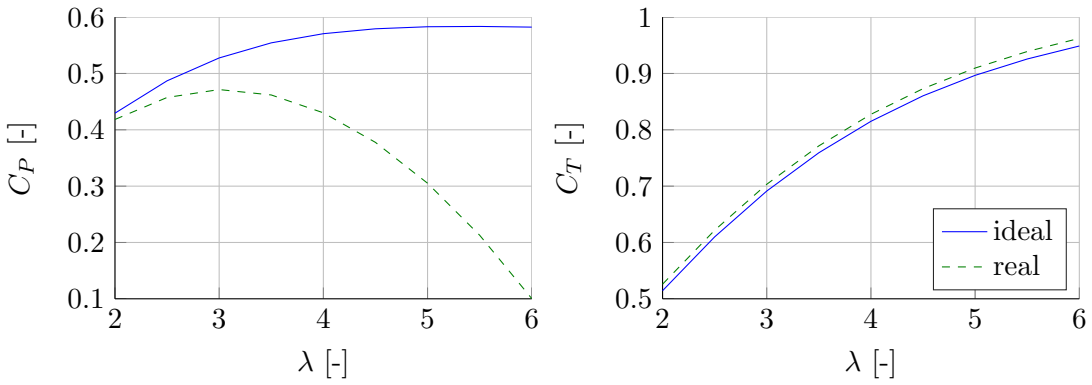

Figure 3.1: *Ideal and real power and thrust curves for* $\sigma = 0.1$.

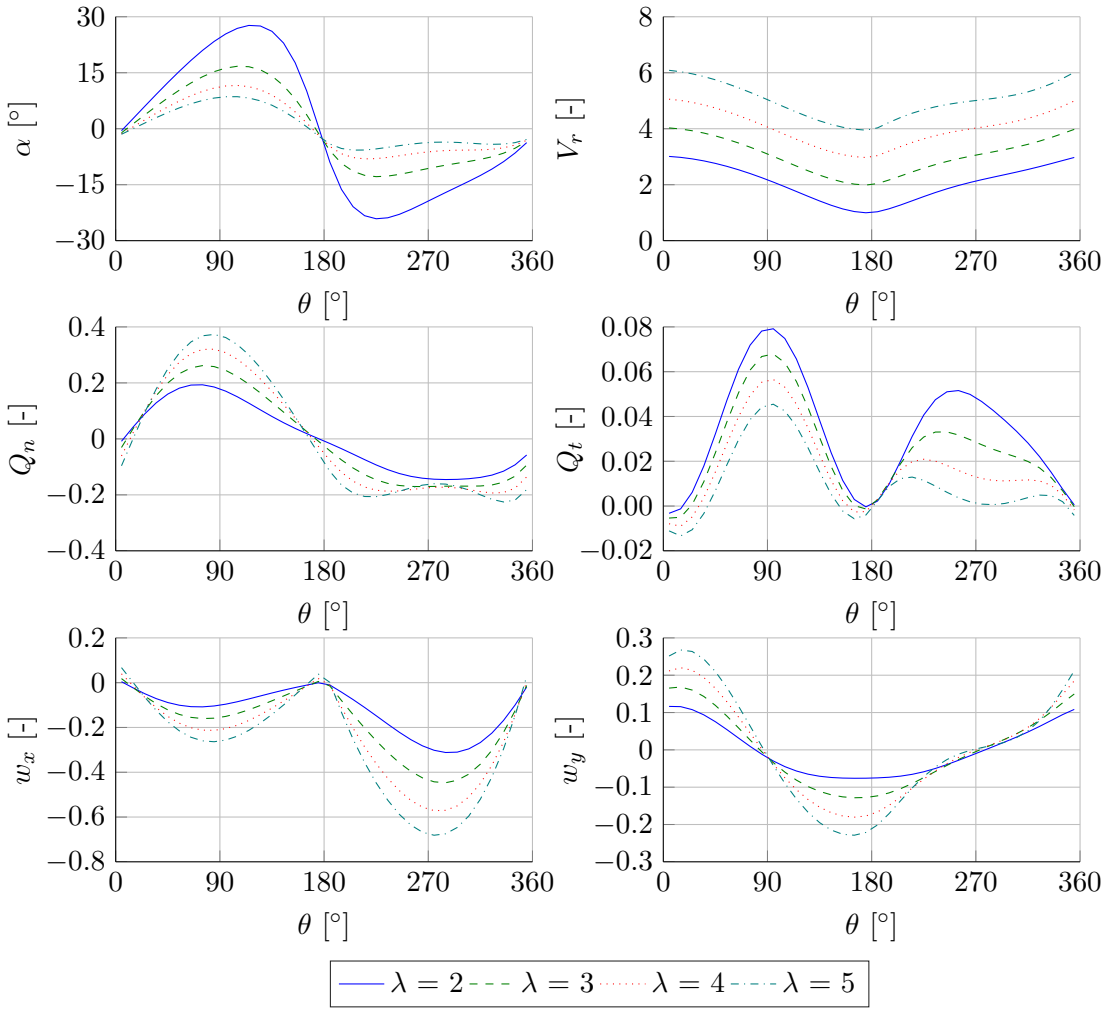

Figure 3.2: *Converged solution of the Mod-Lin Actuator Cylinder Model with rotor solidity* $\sigma = 0.1$*, lift coefficient* $C_l = 2\pi \sin\alpha$ *and drag coefficient* $C_d = 0.023$*.*

since the direction of V_r is line with that of V_∞ here. At an azimuthal position around $\theta = 120°$ the normal velocity direction is most dominant with respect to the tangential component, which explains the occurance of the maximum angle of attack at this location. This phenomenon repeats itself, mirrored, around 90° later, hence the negative angle of attack. After this second maximum the influence of the normal velocity component slowly diminishes, until at $\theta = 360°$ the relative velocity is in line with the free-stream velocity again. It is observed that absolute angles of attack are reduced beyond $\theta = 180°$. The reason for this is that a lower free-stream velocity is experienced on the downwind part of the rotor, hence a relative reduction of the normal velocity component.

The relative velocity starts at its maximum value since the rotational velocity and free-stream velocity have the same direction here. Self-evidently, a minimum value occurs around $\theta = 180°$ due to opposite directions of these velocities. This trend is observed for all tip-speed ratios, although the tangential velocity components becomes more dominant with increasing λ, hence the upward shift of the velocity curve. A slight reduction of velocity magnitude in the downwind half of the rotor due to a lower inflow velocity is also

visible here. This effect becomes more pronounced for higher tip-speed ratios due to the higher induction velocities, which are also visible in the figure.

Both the dimensionless normal and tangential blade loadings increase to their maximum absolute value in the first quarter of the rotor circumference. From the expressions for power it follows that this is the part of the rotor where the highest energy extraction takes place. It is observed that Q_n increases with λ, whereas the opposite holds for Q_t. Large angles of attack are obtained for low λ, which, according to respectivily equation (3.11) and equation (3.12), result in a small normal loading and a large tangential loading. Opposite behaviour is observed as λ is increased.

In the axial induction distribution the reduction of free-stream velocity on each part of the rotor is visible. When observing the curve, it must be kept in mind that the model assumes that a particle travels along a line at a certain y-coordinate. Therefore, the location of maximum reduction on the upwind part will also be the location on the downwind half where maximum reduction takes place. It is concluded that on the interval $\theta = [270°; 90°]$ the free-stream velocity is slowed down the most, which confirms the statement that more energy is extracted from the flow in the top half of the cylinder with respect to the bottom half. Zero reduction (or even a very slight increase) of velocity is observed near the cylinder's edges at $\theta = 0°$ and 180°. The tangential induction is a direct result of the rotational velocity, hence the increase in absolute values with λ.

3.3 Chapter conclusions

The targets of this chapter were to describe the implementation method of the Mod-Lin ACM as well as identifying the most relevant aerodynamic characteristics and performance features. A summery of the main findings, together with some relevant conclusions, is listed below.

- The original linear ACM Madsen [30] underestimates the induced velocities at high loadings. In Madsen [30] a correction factor k_a is derived, based solely on the rotor's local induction factor which, in its turn, is based entirely on the thrust C_T. This modified version of the linear ACM is referred to as the Mod-Lin ACM.
- The ideal power ignores tangential loading effects and is therefore a general measure for the maximum achievable VAWT performance, given a certain solidity σ.
- The real power, as its name indicates, provides a more realistic estimate for a VAWT's power production since the effect of drag is taken into account.
- The aerodynamic quantities α, V_r, Q_n and Q_t are reduced in the downwind half of the rotor with respect to the upwind part as the inflow velocity is lower here.
- The most efficient part of the rotor in terms of energy exchange is the first quarter section.

Chapter 4

Modelling Dynamic Stall Effects

The ACM, implemented in the previous chapter, is capable of calculating the performance of an actuator cylinder in terms of power and loads, as well as its impact on the free-stream velocity by means of induction velocities. The rotor geometry is described according to one single dimensionless parameter: the rotor solidity σ. According to Madsen [30] the actuator cylinder is defined as a rotor with infinite number of blades, which would yield zero chord length for a fixed σ. However, any other definition for an actuator cylinder, keeping a fixed solidity, will still have the same results as modelled by the ACM. Naturally, in reality there will be a difference in performance between, for instance, a two-bladed and a three-bladed machine, even when the respective rotor solidities are the same. In order to take into account these discrepancies modelling of unsteady aerodynamics is required, for which a Beddoes-Leishman type dynamic stall model will be utilized.

This chapter will first shine light on the implementation procedure of unsteady attached flow and trailing edge separation dynamics, as described by the Risø dynamic stall model [21]. Second, the formulation of leading edge separation dynamics, as proposed by Larsen et al. [26], is rewritten into the same indicial formulation as the Risø model so that it can easily be implemented as plug-in. After a brief validation and demonstration of the model, for which a NACA 0018 airfoil is used, the dynamic stall model will be implemented as subroutine to the ACM. The quasi-steady formulations of C_l and C_d will thus be replaced by their unsteady equivalents C_l^{dyn} and C_d^{dyn}, respectivily. Finally, the impact of unsteady aerodynamics on the ACM simulations will be assessed and some potential compatibility issues will be identified.

4.1 Implementing the dynamic stall model

This section will elaborate on the implementation of the dynamic stall model within the ACM. First, the dynamics of attached flow and trailing edge separation is modelled, which is done according to the Risø model [21] [3]. This model is also included in the ACM used in the aeroelastic solver HAWC2. Second, the dynamics of leading edge separation is added following the Larsen-Nielsen-Krenk procedure [26].

4.1.1 Preprocessing - steady lift decomposition

The dynamic stall model requires input data in the form of a Beddoes-Leishman formulation of steady polar data, where the steady lift coefficient is decomposed as the weighted sum of the lift coefficient under attached flow conditions, C_l^{att}, and the lift coefficient under fully separated flow conditions, C_l^{fs} [3]. The weight function here is called the steady separation function, f^{st}, and relates the steady lift coefficient to its two components according to

$$C_l^{\text{st}} = C_l^{\text{att}} f^{\text{st}} + C_l^{\text{fs}}(1 - f^{\text{st}}). \tag{4.1}$$

Above equation indicates that a separation function of $f^{\text{st}} = 1$ corresponds to a fully attached flow and a separation function of $f^{\text{st}} = 0$ corresponds to a fully separated flow. The steady input data has to be computed as a function of angle of attack and can be regarded as a preprocessing procedure. The preprocessor algorithm, as described by Hansen et al. [21] and Bergami and Gaunaa [3], is summarized here for convenience.

The separation function is computed from

$$f(\alpha) = \left(2\sqrt{\frac{C_l^{\text{st}}}{C_{l,\alpha}(\alpha - \alpha_0)}} - 1\right)^2, \tag{4.2}$$

which follows from the expression for the lift of a flat plat in Kirchoff flow. In equation (4.2), α_0 is the angle of attack which gives zero lift and $C_{l,\alpha} = \max\left\{C_l^{\text{st}}/(\alpha - \alpha_0)\right\}$ is the slope of the linear part of the lift curve. An additional note to the separation function is that it should be real and bounded $0 \leq f^{\text{st}} \leq 1$.

The lift coefficient corresponding to full separation is computed from equation (4.1), assuming that the steady lift polar is given. Rewriting this expression gives

$$C_l^{\text{fs}}(\alpha) = \frac{C_l^{\text{st}} - C_{l,\alpha}(\alpha - \alpha_0) f^{\text{st}}}{1 - f^{\text{st}}}. \tag{4.3}$$

For the fully attached region, i.e. $f^{\text{st}} = 1$, it is derived that $C_l^{\text{fs}}(\alpha) \to \frac{C_l^{\text{st}}(\alpha)}{2}$.

The resulting steady lift decomposition is shown in Figure 4.1 for DU30 airfoil data. The plotted data will be used as *lookup data* for the computation of the dynamic coefficients, which will be the subject of the subsequent sections.

4.1.2 Dynamics of attached flow and trailing edge separation

The coupled set of ODEs that form the backbone of the Risø model for the attached flow and trailing edge separation are presented here. Input to this system is the airfoil motion, i.e. the geometric angle of attack α, the angle of attack at three-quarter point $\alpha_{3/4}$, the pitch rate $\dot{\alpha}$, the free-stream velocity U and acceleration $\dot{U}$. It must be noted here that the free-stream velocity U corresponds to the airfoil relative velocity V_r, which follows

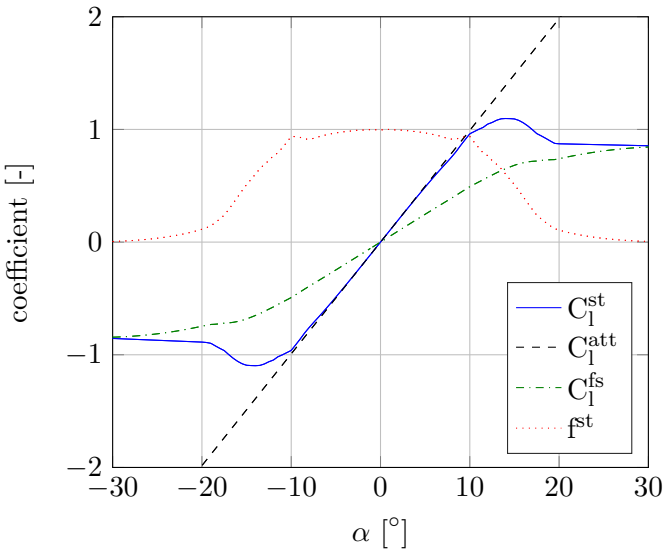

Figure 4.1: *Example of Beddoes-Leishman decomposition for the lift of the NACA0018 airfoil.*

from the ACM (equation (3.9)).

$$\dot{x}_1 + T_u^{-1}\left(b_1 + c\dot{U}/(2U^2)\right)x_1 = b_1 A_1 T_u^{-1}\alpha_{3/4} \tag{4.4}$$

$$\dot{x}_2 + T_u^{-1}\left(b_2 + c\dot{U}/(2U^2)\right)x_2 = b_2 A_2 T_u^{-1}\alpha_{3/4} \tag{4.5}$$

$$\dot{x}_3 + T_p^{-1}x_3 = T_p^{-1}(C_{l,\alpha}(\alpha_E - \alpha_0) + \pi T_u\dot{\alpha}) \tag{4.6}$$

$$\dot{x}_4 + T_f^{-1}x_4 = T_f^{-1}f^{\mathrm{st}}(x_3/C_{l,\alpha} + \alpha_0) \tag{4.7}$$

The system of ODEs includes a total of four aerodynamic state variables, $x_1, ..., x_4$, each of which corresponds to a certain dynamic effect. The first two state variables are used to model the the lift coefficient of unsteady attached flow, C_l^p. The third state variable is a delayed lift coefficient for attached flow, $x_3(t) = C_l^{p\prime}$, used to determine an equivalent quasi-steady separation point $f' = f^{\mathrm{st}}\left(x_3/C_{l,\alpha} + \alpha_0\right)$, which is obtained from equation (4.2). The fourth state variable describes the time lag of the separation point with respect to the quasi-steady value f', caused by the dynamics of the boundary layer, i.e. $x_4(t) = f''$. Similar to the decomposition of the steady lift coefficient in equation (4.1), the unsteady lift coefficient is expressed as the weighted sum of the unsteady lift coefficient under attached and fully separated flow conditions, plus a non-circulatory added mass contribution. The following expressions for total dynamic lift and total dynamic drag are given as:

$$C_l^{\mathrm{dyn}} = C_{L,\alpha}(\alpha_E - \alpha_0)x_4(t) + C_L^{\mathrm{fs}}(\alpha_E)(1 - x_4(t)) + \pi T_u\dot{\alpha} \tag{4.8}$$

$$\begin{aligned} C_d^{\mathrm{dyn}} =& C_D^{\mathrm{st}}(\alpha_E) + (\alpha - \alpha_E)C_L^{\mathrm{dyn}} \\ &+ \left(C_D^{\mathrm{st}} - C_{D_0}\right)\left(\frac{\sqrt{f^{\mathrm{st}}(\alpha_E)} - \sqrt{x_4}}{2} - \frac{f^{\mathrm{st}} - x_4}{4}\right). \end{aligned} \tag{4.9}$$

The variables $T_u = c/(2U)$, $T_p = \tau_p c/(2U)$ and $T_f = \tau_f c/(2U)$ are time constants with respect to velocity, lag in pressure and lag in the boundary layer, respecitvely. Values for the non-dimensional time constants τ_p and τ_f are airfoil dependent, but not very much.

The Risø model is implemented in Matlab following the implicit indicial method formulation [21]. The response of the system is expressed in terms of exponential functions, which is very numerically efficient since the solution of the state variables for a time step is found by decaying the solution from the previous time step and adding an increment:

$$x_i(t + \Delta t) = C_{dec,i}\ x_i(t) + I_{new,i}. \tag{4.10}$$

Writing the system of linear ODEs in the form $\dot{x}_i + P_i x_i = Q_i$, values for the decay and increment are found in terms of P_i and Q_i by employing Duhamel's integral:

$$C_{dec,i} = e^{-\int_t^{t+\Delta t} P_i \mathrm{d}t} \tag{4.11}$$

$$I_{new,i} = \int_t^{t+\Delta t} Q_i e^{-\int_t^{t+\Delta t} P_i \mathrm{d}\tau} \mathrm{d}t. \tag{4.12}$$

The expressions for $C_{dec,i}$ and $I_{new,i}$ are discretized assuming a piecewise constant P_i and parabolic Q_i, giving

$$C_{dec,i} = e^{-P_i^j \Delta t} \tag{4.13}$$

$$\begin{aligned} I_{new,i} =& \frac{Q_i^{j-1}}{P_i^j}(1 - e^{-P_i^j \Delta t}) \\ &+ \frac{Q_i^j - Q_i^{j-2}}{2\Delta t P_i^j}\left(\Delta t - \frac{1}{P_i^j}(1 - e^{-P_i \Delta t})\right) \\ &+ \frac{Q_i^j - 2Q_i^{j-1} + Q_i^{j-2}}{2\Delta t^2 P_i^j}\left(\Delta t^2 - \frac{2\Delta t}{P_i^j} + \frac{2}{(P_i^j)^2}(1 - e^{-P_i \Delta t})\right), \end{aligned} \tag{4.14}$$

with the terms

$$P_{1,2}^j = b_{1,2}\frac{U^j + U^{j-1}}{c} + \frac{\dot{U}^j + \dot{U}^{j-1}}{U^j + U^{j-1}} \tag{4.15}$$

$$P_3^j = (T_p^j)^{-1} \tag{4.16}$$

$$P_4^j = (T_f^j)^{-1} \tag{4.17}$$

$$Q_{1,2}^j = (T_u^j)^{-1} b_{1,2} A_{1,2} \alpha_{3/4}^j \tag{4.18}$$

$$Q_3^j = (T_p^j)^{-1} C_l^{p,j} \tag{4.19}$$

$$Q_4^j = (T_f^j)^{-1} f^{\mathrm{st}}\left(\frac{x_3^j}{C_{l,\alpha}} + \alpha_0\right). \tag{4.20}$$

Once the decay and increment are found, the state variables are updated using equation (4.10). Attached flow dynamics must be computed first, since the state variables related to TE separation depend on this solution, as can be seen in equation (4.19). This is done according to

$$\alpha_E^j = \alpha_{3/4}^j(1 - A_1 - A_2) + x_1^j + x_2^j \tag{4.21}$$

$$C_l^{p,j} = C_{l,\alpha}(\alpha_E^j - \alpha_0) + \pi T_u^j \dot{\alpha}^j. \tag{4.22}$$

The delay in attached lift, x_3^j, is then used to compute an equivalent angle of attack, $(x_3^j/C_{l,\alpha} + \alpha_0)$, for which the corresponding delayed separation point is found from equation (4.2). Boundary layer dynamics is then taken into account in equation (4.20), and x_4^j is used to compute $C_l^{\mathrm{dyn},j}$ from equation (4.8). The procedure is then repeated for the new time step $t = t^{j+1}$.

4.1.3 Dynamics of leading edge separation

Larsen et al. [26] introduces an extra state variable, $C_{l,v}$, to model the vortex and pressure peak induced lift under leading edge separation. This state variable is added to the previously computed dynamic lift under trailing edge separation, C_l^{dyn}, to obtain the total lift $C_l^{\mathrm{dyn,tot}}$. The leading edge separation induced lift is calculated from the following first-order ODE:

$$\dot{C}_{l,v}(t) + b_4 C_{l,v}(t) = \begin{cases} \Delta\dot{C}_l(t) & \text{for } \tau < 1 \text{ and } \dot{\alpha} > 0, \\ 0 & \text{otherwise.} \end{cases} \tag{4.23}$$

where b_4 is a profile dependent parameter that controls the lift decreasal of vortex induced lift beyond the critical angle (α_v) and ΔC_l is calculated from

$$\Delta C_l(t) = C_l^{\mathrm{dyn}}(t) - C_l^p(t). \tag{4.24}$$

The parameter τ in equation (4.23) controls the position of the travelling vortex along the upper surface of the airofoil. It is a non-dimensional parameter that equals 0 when the vortex is at the leading edge and 1 when the vortex is at the trailing edge. So from equation (4.23) it is clear that the vortex-induced lift builds up for positive pitch rates, and as soon as τ hits 1 the vortex detaches and its effect diminishes. When $\dot{\alpha} < 0$, a new cycle starts with $\tau = 0$, which starts increasing again when $\alpha > \alpha_v$ according to

$$\dot{\tau} = \begin{cases} \frac{U}{3c} & \text{for } \alpha > \alpha_v, \\ 0 & \text{otherwise.} \end{cases} \tag{4.25}$$

In a VAWT, the airfoil will oscillate between positive and negative angles of attack. Therefore, a vortex will also start to build up when $\dot{\alpha} < 0$ and $\tau < 1$. For the case of a symmetrical airfoil, the critical angle in equation (4.25) will simply be $-\alpha_v$. For a cambered airfoil the vortex behaviour for $\dot{\alpha} < 0$ will differ from that of $\dot{\alpha} > 0$, hence a different α_v will apply.

The fifth state variable, $x_5 = C_{l,v}$, is implemented in Matlab following the indicial formulation of equation (4.10), with

$$P_5^j = b_4, \tag{4.26}$$

$$Q_5^j = \begin{cases} \Delta\dot{C}_l^j & \text{for } \alpha_E^j > \alpha_v \text{ and } \dot{\alpha}^j > 0, \\ 0 & \text{otherwise,} \end{cases} \tag{4.27}$$

Note that since $C_{l,v}$ is by its definition an increment added to $C_l^{\mathrm{dyn}}(t)$ on each time step, there exists no decay term for this variable, hence $C_{l,v} = I_{new,5}$.

4.2 Assessment of the model with the NACA0018 airfoil

In this section the lift and drag polars of the symmetrical NACA0018 airfoil will be subjected to the dynamic stall model. The polar data of this airfoil is given in Appendix A. First, a quantative validation of the attached flow and leading edge separation submodel, that is, the *Risø model*, will be carried out against data from the aeroelastic solver *HAWC2*. Second, the complete model, including the impact of leading edge separation, as computed by the *Larsen-Nielsen-Krenk (L-N-K) model*, will be addressed by analyzing different oscillation ranges and frequencies.

Validation of attached flow and trailing edge separation

The input parameters for the validation of the Risø model are shown in Table 4.1 and the timeseries of the angle of attack and airfoil-relative velocity are displayed in Figure 4.2. This validation data corresponds to a VAWT and therefore $\dot{\alpha}$ is chosen as $-\omega$. The characteristic hysteresis loops of the lift and drag coefficients are plotted in Figure 4.2 and an almost one-to-one similarity between the implemented model and the results from *HAWC2* is observed. Note that the applied airfoil is symmetrical and applied in the context of a VAWT, hence the values for C_l^{dyn} and C_d^{dyn} can be both positive and negative, the latter of which is the case in Figure 4.3.

Table 4.1: *Input data for verification of dynamic stall model, based on Larsen et al. [26].*

Parameter	Symbol	Unit	Value
Time step size	Δt	s	0.02
Chord length	c	m	1.17
Rotational velocity	ω	rad/s	3.456
Profile dependent parameters	A	[-]	[0.165; 0.335]
	b	[-]	[0.0455; 0.3; 0.1; 0.075]
	τ_p	[-]	1.5
	τ_f	[-]	6

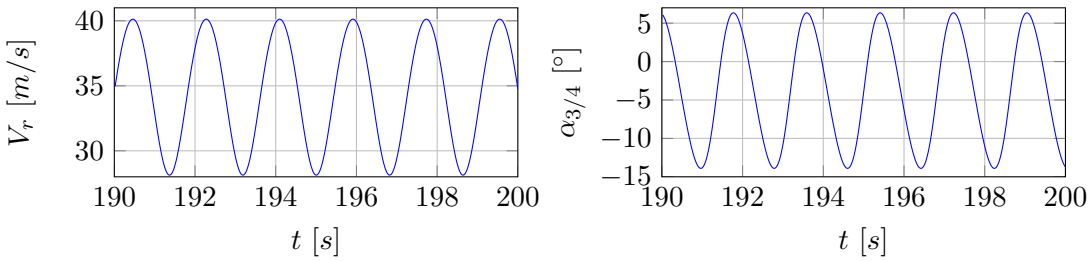

Figure 4.2: *Timeseries of angle of attack and relative velocity for validation of the Risø model implementation.*

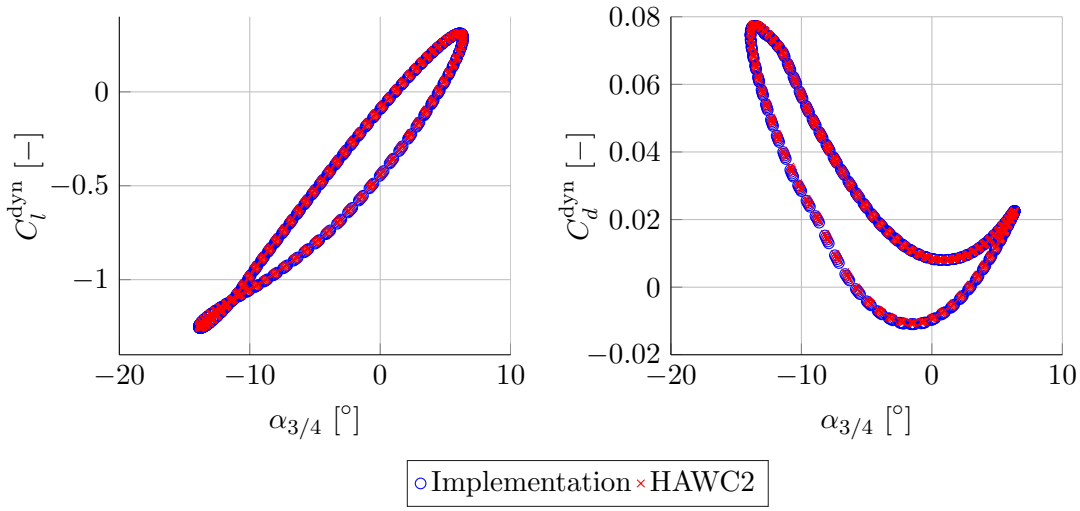

Figure 4.3: *Validation of the dynamic lift and drag coefficients for the NACA0018 airfoil.*

4.2.1 Demonstration of the complete model

This section will bring to light the impact of unsteady flow phenomena on the aerodynamic force coefficients and reveal some key parameters that influence the degree of unsteadyness. This section will only deal with the simple case of a pitching airfoil in rectilinear flow, hence the relative velocity will be constant and, therefore, its derivative zero.

First, Figure 4.4 shows the loops for an amplitude of $\Delta\alpha = \pm 4°$, about three different mean values. Since the airfoil at issue is a symmetrical airfoil, the C_l and C_d loops for the mean values of 13° and −13° are similar but mirrored. For these mean values the induced lift addition, due to the accumulation of leading edge vortex strength, is clearly visible. The dependency on the critical angle α_v is obvious: when this angle is low, around ±12°, the vortex detaches at an early stage and the vortex-induced lift diminishes. One can imagine that such a sudden sudden drop in lift can cause a small, but present, fatigue loading on the blade if it occurs at every revolution. On the other hand, when α_v is high, the induced lift continues to accumulate until $\dot{\alpha}$ changes sign. Since the lift-induced drag term in equation (4.9) is only a very small portion of the total dynamic drag ($< 1\%$), the effect of leading edge separation on the dynamic drag coefficient is close to zero.

The arrows in Figure 4.4 indicate the direction of the hysteresis loops. It can be seen that if the airfoil pitches at angles around the stall region, the lift will be higher for increasing absolute angle of attack than for decreasing angles. This can be explained as the airfoil accumulating lift for increasing absolute α, and the flow needing time to reattach after stall has occured. An opposite behaviour in loop direction is witnessed when the airfoil does not encounter stall while pitching. In this case, the flow is attached throughout and the airfoil needs time to loose its accumulated lift.

The degree of unsteadiness of a flow is determined by the reduced frequency, that is, $k = \omega_a c/(2U)$ with ω_a the airfoil's angular frequency. In Figure 4.4 for example, the reduced frequency $k = 0.0698$, which is catagorized as unsteady flow (for values $k > 0.05$ the flow is regarded as unsteady and for $k > 0.2$ the flow is highly unsteady). This

implies that, by altering either the chord, the angular frequency or the relative velocity, the degree to which unsteady effects are dominant in a flow can be controlled. A more extensive investigation of this feature will be carried out in the subsequent section, where the dynamic stall model is coupled to the ACM.

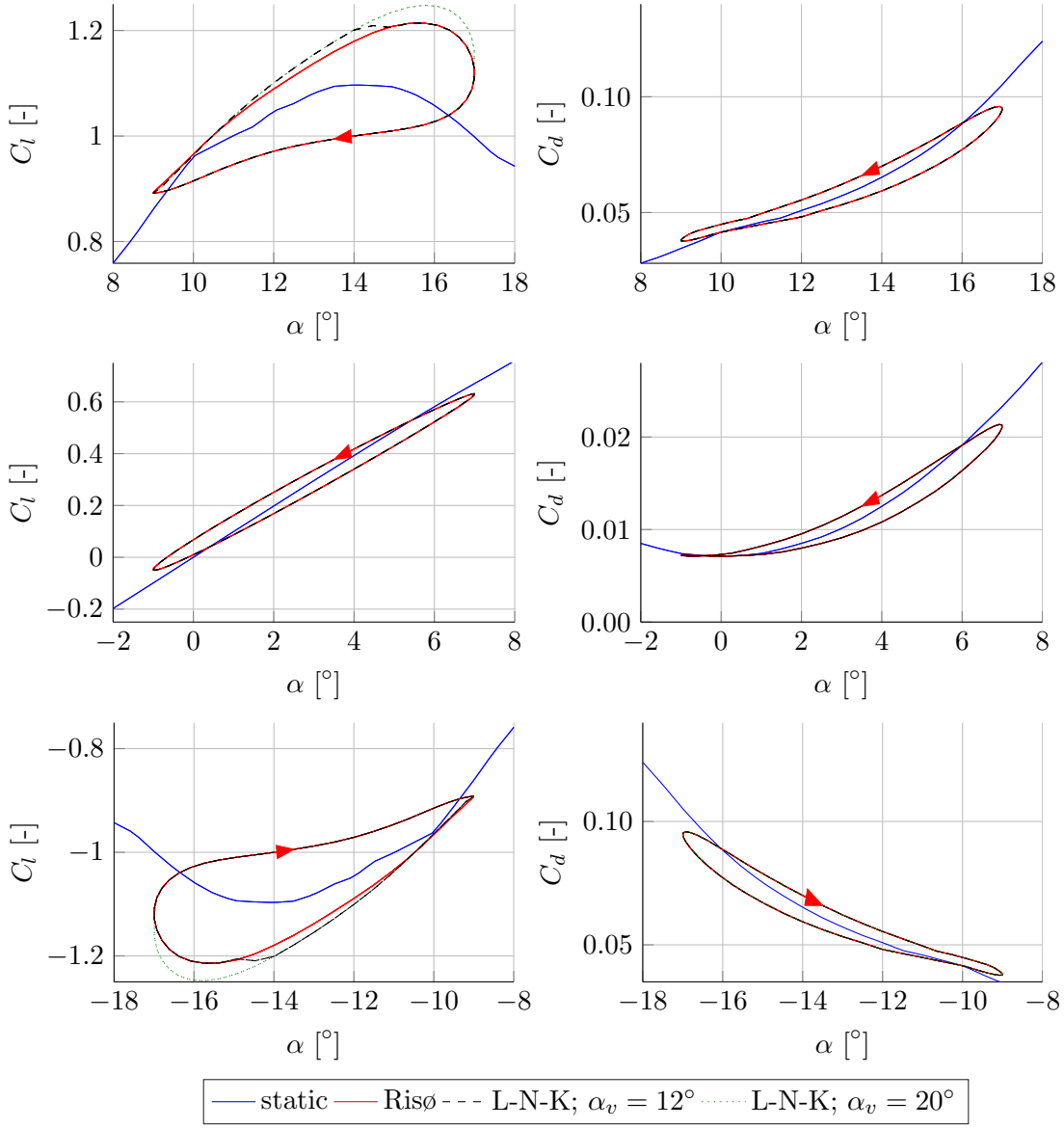

Figure 4.4: *Dynamic stall behaviour of the NACA0018 airfoil, with* $k = \omega c/(2U) = 0.0698$.

4.3 Coupling the dynamic stall model to the Actuator Cylinder Model

This section will focus on the implementation of the dynamic stall model as a submodel to the ACM. The complete routine of the ACM with unsteady flow option is visualized in

Figure 4.5. The flowchart clearly exposes the instantaneousness of the correction factor and induction velocities, which means that a change in any flow parameter upstream of the rotor will be felt directly, without any transient, downstream of the rotor. Naturally this is not the case in reality, but this assumption significantly reduces the complexity of the model. Implementation of unsteady effects will be carried out such that the user has the following options for flow conditions:

1. Steady flow;
2. Unsteady attached flow;
3. Unsteady attached flow with TE separation;
4. Full dynamic stall model.

Having these options allows identification of those unsteady phenomena that will be critical for the VAWT's performance at certain flow conditions and solidities.

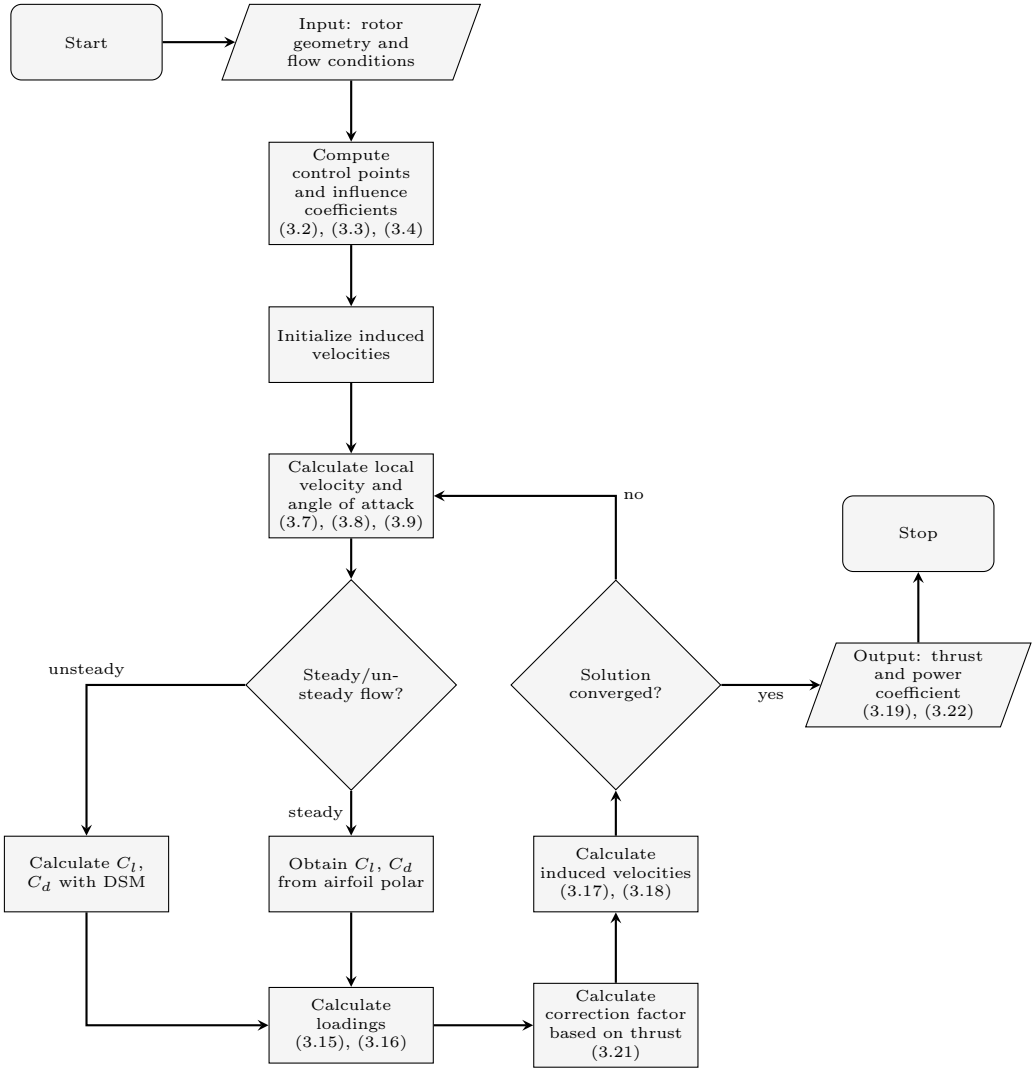

Figure 4.5: *Flowchart of the ACM implementation with dynamic stall option.*

The dynamic stall model, developed in Section 4.1, is now re-written into a Matlab function which requires the following inputs: the steady lift C_l^{st}, the lift slope $C_{l,\alpha}$, the geometric angle of attack α, the zero-lift angle of attack α_0, the relative velocity V_r, and the chord length c. For each step in azimuthal position ($i = i + 1$) the dynamic stall function is called to compute unsteady lift and drag coefficients, $C_l^{\text{dyn,tot}}$ and $C_d^{\text{dyn,tot}}$, and the effective angle of attack (a_E), which will be inserted in equation (3.11) and equation (3.12) to calculate the unsteady blade loadings. The conversion between $\Delta\theta$, employed by the ACM, and Δt, used by the dynamic stall function to calculate the time history-dependent aerodynamic loads, is carried out according to

$$\Delta t = \frac{\Delta\theta}{\omega} = \frac{R\Delta\theta}{\lambda V_\infty}. \tag{4.28}$$

Furthermore, dynamic stall function requires the time derivatives $\dot{V}_r$, $\dot{\alpha}$ and $\Delta\dot{C}_l$, for which a first-order forward difference scheme is used:

$$\dot{y}(t) = \frac{y(t) - y(t - \Delta t)}{\Delta t}. \tag{4.29}$$

4.4 Compatability of the models

This section will focus on some important topics considering the compatability of the two models. The critical parameters will be identified and an analysis of their influence on the rotor performance will be carried out. This analysis will first focus an inviscid flat plate, where $C_l^{\text{st}} = 2\pi\alpha$ and $\alpha_0 = 0°$, so that the separation function is always equal to 1 (see equation (4.2)). Therefore, the effects of trailing edge and leading edge separation are not taken into account. After this primary analysis, the model will be extended to account for (dynamic) stall effects, following the NACA0018 airfoil polar.

4.4.1 Rotor solidity and reduced frequency

Each of the two models has its own non-dimensional quantity that governs a large part of its behaviour. For the ACM at a given tip-speed ratio, the calculated induced velocities and blade loadings mainly depend on the rotor solidity, given by equation (4.30). The level of significance of the unsteady effects modelled by the dynamic stall model is mainly determined by the airfoil's reduced frequency, which is calculated according to equation (4.31). It must be noted that, unlike the original Beddoes-Leishman formulation, the relative velocity V_r is used here since this is the velocity encountered by the airfoil.

$$\sigma = \frac{Bc}{2R} \tag{4.30}$$

$$k = \frac{\omega_a c}{2V_r} \tag{4.31}$$

Comparing above non-dimensional expressions it is observed that the chord length c forms a bridge between the two. Therefore, if the solidity σ and radius R are kept constant, and

the number of blades B is adjusted, this will inversely affect the reduced frequency and therefore the unsteady aerodynamics of the rotor. This implies that the steady results that follow from Madsen's initial formulation of the ACM, which are a function of σ only, can now be extended such that they account for the number of blades as well, through modelling of unsteady shed vorticity effects. For an infinite number of blades the chord length approaches zero and it follows from Kelvin's circulation theorem that there will be zero bound circulation. Without a bound circulation the Kutta condition implies that there will be no shed vorticity effect on the angle of attack, so $\alpha_E \to \alpha$ for $B \to \infty$. The diminishing of the unsteady effect for increasing number of blades is visible in Figure 4.6, where it is visible that there is no unsteady vortex-induced effect on the lift coefficient either.

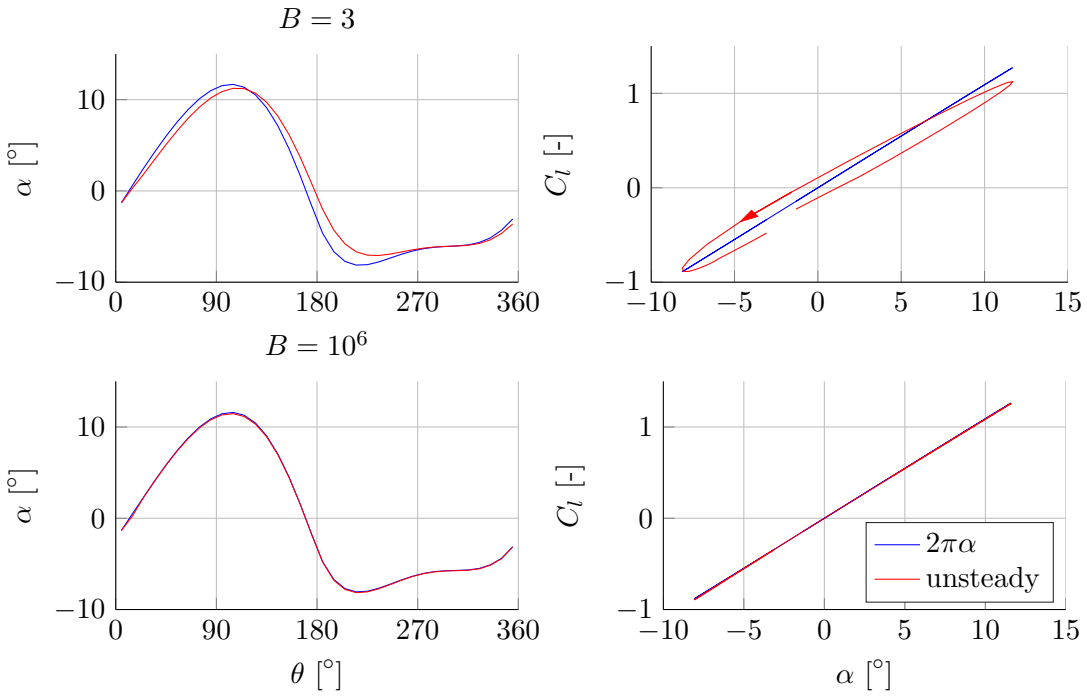

Figure 4.6: *Unsteady effect on lift coefficient for a single revolution, with* $\lambda = 4$, $\sigma = 0.1$ *and* $B = 3$ *–* $k = \mathcal{O}(10^{-1})$ *– and* $B = 10^6$ *–* $k = \mathcal{O}(10^{-9})$.

Figure 4.7 shows the unsteady shed vorticity effect for a finite bladed machine on the global power and thrust . From these curves it is seen that the unsteady effect is more or less constant with respect to the tip-speed ratio. Therefore, in a sense the dynamic stall function can be regarded as a correction factor to the ACM for finite number of blades. For $B = 3$, the global power production sees a reduction of ~ 0.04 (around 8% of $C_{P_{\max}}$) and the global thrust sees a reduction of ~ 0.02 (around 2% of $C_{T_{\max}}$). Furthermore, it is again confirmed that the unsteady effect diminishes for increasing number of blades. The small deviation that still occurs is due to their different numerical computations.

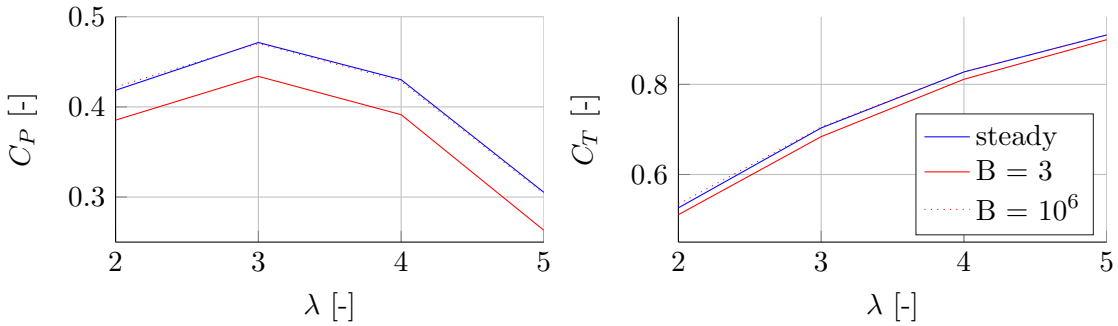

Figure 4.7: *Unsteady effect on power and thrust coefficient, with* $\sigma = 0.1$ *and* $B = 3$ *–* $k = \mathcal{O}(10^{-1})$ *– and* $B = 10^6$ *–* $k = \mathcal{O}(10^{-9})$.

4.4.2 Bound circulation and local blade efficiency

This section will focus on the local power production for each azimuthal blade position. In Figure 4.8, the local power distribution under steady and unsteady flow assumption are compared to the ideal power distribution for $\lambda = 4$. The ideal curve is obtained under *ideal rotor assumption*, that is, the assumption of a zero-drag 2D actuator with infinite number of blades, and follows from equation (3.22). The steady curve coincides with the converged Mod-Lin solution of the ACM, equation (3.23), where aerodynamic drag is taken into account. The unsteady shed vorticity effect as a result of a finite number of blades is incorporated in the dynamic stall submodel.

On the interval $\theta \in [30°, 90°]$ a constant difference is visible between the ideal and the steady curve, which is caused by the drag term being ignored in the ideal curve. On this same interval, there is an increasing difference between the unsteady curve and the other two curves. This is attributed to the gain in bound circulation on this interval caused by the increasing angle of attack, so there will be an increase of the unsteady shed vorticity effect. On the interval $\theta \in [90°, 170°]$ both the steady and unsteady curve approach the ideal curve. This is due to the fact that the angle of attack decreases on this interval, hence the effect of drag and vortex-induced loads diminishes. The difference between the unsteady curve and the ideal curves on the interval $\theta \in [180°, 270°]$ is caused by the delay in effective angle of attack (α_E) with respect to the geometric angle of attack (α), visible

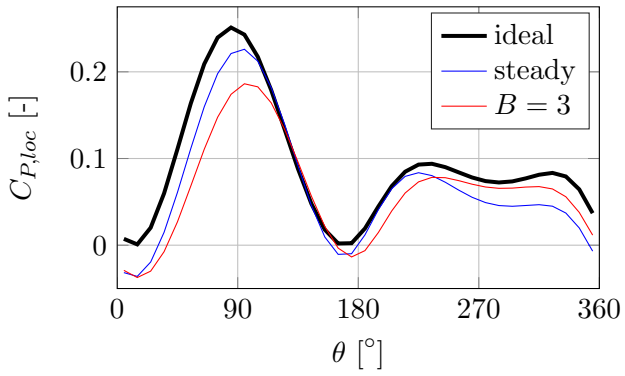

Figure 4.8: *Ideal, steady and unsteady* ($B = 3$) *local power production, with* $\lambda = 4$ *and* $\sigma = 0.1$

in the upper left-hand corner of Figure 4.6. At $\theta = 270°$ the angle of attack (and bound circulation) starts increasing again and the cycle repeats itself at $\theta = 0°$. Furthermore it is observed that the unsteady power production is actually higher than that of the steady case at $225° < \theta < 360°$. The explaination for this lies in the hysteresis curve plotted in the upper right-hand corner of Figure 4.6, which shows a higher C_l on this interval for unsteady flow than for steady flow.

4.4.3 Double-counting the near-wake vorticity

When implementing the dynamic stall model within the ACM as described here, a questionable issue regarding the computation of the effective angle of attack arises. In the ACM, the angle of attack is modelled as the ratio of normal to tangential local velocity (V_n/V_t), which follows directly from the induced velocities in the near-wake. The dynamic stall model then calculates an effective angle of attack, which is based on the local velocity, angle of attack and their respective time-derivatives. Thus, the impact of local velocity on the angle of effect is computed twice, which implies there might be an overlap in this combined model that results in a double-counting of the near-wake vorticity. This effect is only enhanced if the model is iterated until the induced velocities have converged, since his double-counting effect will accumulate over the iteration steps. Mitigation of this problem is not included in this thesis project, so this section is merely intended to identify the issue for future research.

4.4.4 Higher-order unsteady effects on the VAWT

In the preceding sections focus was on the first-order unsteady effect on a VAWT blade during a single revolution, based on the inviscid lift polar of a flat plate. This section will expand that research by taking into account the effects of unsteady flow separation (both at the leading edge and the trailing edge). The objective is to obtain a clear picture of the significance of the unsteady effects for various tip-speed ratios. For this analysis, again, the NACA0018 viscous airofoil polar will serve as reference data. The chosen number of blades $B = 3$ and the rotor solidity $\sigma = 0.1$.

It is observed that the unsteady effect of vortex-induced lift under leading edge separation disappears for $\lambda > 3$. The reason for this is simply that the necessary α and $\dot{\alpha}$ are not met. The higher tip-speed ratio gets, the higher the tangential velocity with respect to the normal component, and the lower the angle of attack range encountered by the airfoil. At some point, the airfoil will therefore only operate in its linear region and separation effects will be omitted.

It should be noted that a recent study by Pirrung and Gaunaa [35]* identifies some erroneous results in the Beddoes-Leishman modelling of dynamic stall properties, when applied to a VAWT. In their paper, Pirrung and Gaunaa propose corrections to the formulation of the effective angle of attack, introduce a contribution to the total lift due to the airfoil's radial acceleration, and include the torsion rate between the evaluation points of the angle of attack and lift in the formulation of the total drag. These modifications, however, are not be a taken into account in the current report.

*currently in review

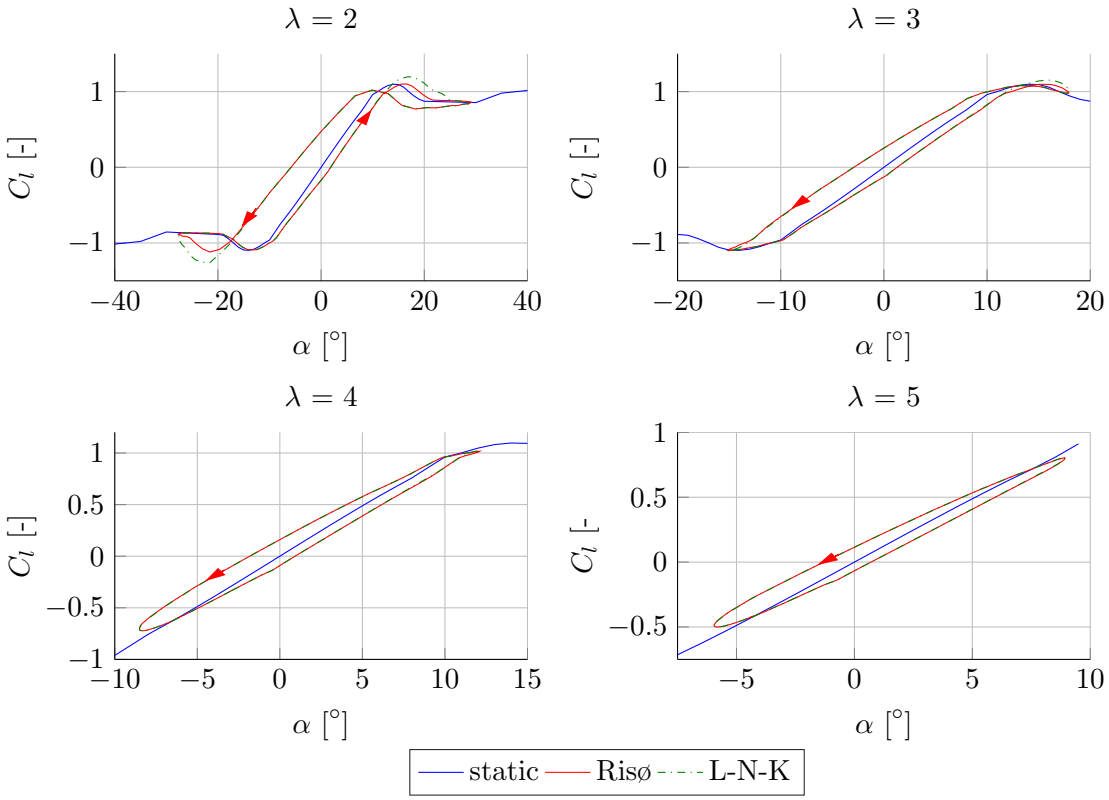

Figure 4.9: *Dynamic stall loops for the NACA0018 airfoil on a VAWT in operation.*

4.5 Chapter conclusions

The Risø model [21] models the dynamics of unsteady attached flow and trailing edge separation of an airfoil, using a total of four aerodynamic state variables (two for each unsteady phenomenon). For the purpose of this thesis the model is implemented in its implicit indicial formulation since this allows solving the ODEs on each time step by decaying the values of the precious time step and adding an increment. This is a numerically efficient solution, especially within the context of a full aeroelastic model such as the ACM. The dynamics of leading edge separation, as formulated by Larsen et al. [26], is rewritten into a similar indicial formulation and implemented as plug-in to the original Risø model. The impact of replacing the quasi-steady aerodynamic force coefficients in the ACM by their dynamic equivalents, computed by the implemented dynamic stall model, is described below.

- The degree of unsteadiness of the flow around an airfoil is determined by the reduced frequency, which is directly dependent of the chord length. Therefore, for a fixed solidity and radius the unsteady effect diminishes when $B \to \infty$.
- The higher the degree of unsteadiness, the larger the power loss with respect to an ideal rotor's power will be.
- Comparing the unsteady local power production to the steady case, it is found that on those intervals where the circulation increases the vortex-induced power loss

grows. When the circulation decreases the unsteady local power production will approach the steady value again. This effect will be larger for larger chord lengths, since the change in bound circulation, and therefore ΔC_L, is directly dependent on this parameter.

- Losses in thrust due to unsteady flow phenomena also increase with unsteadiness, but to a smaller degree than the rotor's power loss. The reason for this is that the unsteady loads will sometimes be smaller, and other times be larger, than the steady coefficients. Therefore the integral value, i.e., the thrust, will only be affected to a small degree.

- When the converged solution of the ACM including the dynamic stall subroutine is analyzed, it is found that the phenomena of leading and trailing edge separation only occur for small tip-speed ratios ($\lambda < 3$). For low the rotational velocities the tangential velocity will be small compared to the inflow velocity, hence larger angles of attack will be encountered, sometimes driving the airfoil into its nonlinear region. For large λ the airfoil stays within the linear region, where the flow will be attached.

Chapter 5

Optimization of Ideal Rotor Performance

In this chapter an exploratory study into the design space of an *ideal rotor* will be carried out. This type of rotor is characterized by an infinite number of blades and zero tangential loading, i.e., $Q_t = 0$. The optimization method applied in this chapter comes down to finding optimum distributions of pressure jumps (Q_n) accros the cylinder surface, which will be referred to as the *loadforms*. The loadforms will be created from a λ- and σ-dependent set of reference Q_n, which have been created in Chapter 3. For the optimization a numerical optimizer will be used that creates optimum loadforms from the reference loadings, staying within a user-determined allowance. The difference between the reference and optimum Q_n is then a direct measure of the necessary pitch sequence to achieve the created loadforms.

The optimization will be carried out for the targets of: 1.) power maximization, 2.) power minimization, and 3.) thrust relief while maintaining power. The first target directly decreases the CoE of the turbine (more power for the same conditions). The second objective is relevant for power control, so to ensure the rotor's power production does not exceed the rated power set by the generator. The third objective aims at decreasing the loading on the blades, and therefore increasing the VAWT's (fatigue) life. Furthermore, thrust minimization results in a more dynamically stable machine, which is favorable considering its potential offshore application.

This chapter is built up as follows. First, a parametric study into the design region of the VAWT is carried out. Second, the implementation of the *loadform optimizer* is described and a sanity check is performed on its results. Third, the actual optimization is carried out for the three targets. Finally, the required pitch sequences are obtained from the loadforms.

5.1 Exploring the $C_P - C_T$ region

Madsen et al. [31] studied the ideal energy conversion of a VAWT-type rotor by prescribing

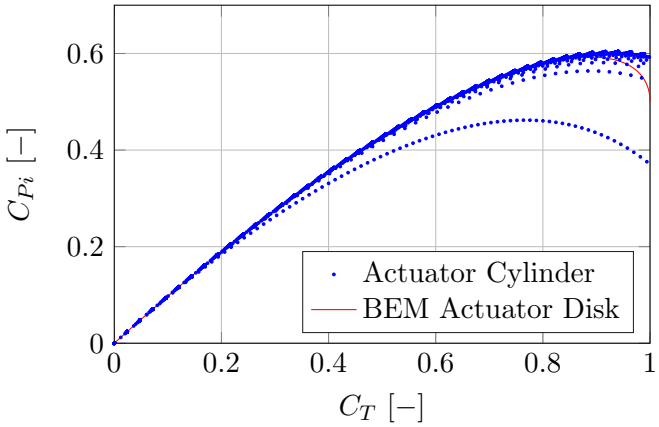

Figure 5.1: *The $C_{Pi} - C_T$ region as computed by the ACM.*

certain loadforms $Q_n(\theta)$ that approach a uniform distribution, which has proved to be the optimal distribution in the derivation of the Betz limit for HAWT-type rotors. It must be noted here that, due to the ideal rotor assumption, the tangential loading $Q_t(\theta)$ is set to zero. The ACM is then used to calculate the local velocities and assess the rotor performance in terms of C_{Pi} and C_T. Different loadforms are created according to equation (5.1) by setting different peak ($Q_{n,max}$) and shape (m) values [31]. A higher value for m yields a more uniform distribution. By selecting a wide range of inputs, i.e. $Q_{n,max} \in [0, 0.6]$ and $m \in [1,\ 300]$, a global overview of the ideal VAWT performance is created and shown in Figure 5.1, where each dot represents a certain combination of input values. The ideal power coefficient resulting from BEM theory for a uniform loading on an actuator disk is plotted in the figure as well.

$$Q_n(\theta) = Q_{n,max} \frac{\sin\theta}{|\sin\theta|} \left(1 - |\cos\theta|^m + \frac{1}{2\pi} \sin\left(2\pi|\cos\theta|^m\right)\right) \tag{5.1}$$

Two striking differences are observed when comparing ACM results to those of BEM. The first is that the Betz limit of $C_{Pi} = 0.593$, that occurs ar a C_T of around 0.9, is slightly exceeded by the VAWT's performance. Similar results are obtained by Madsen et al. [31], who partly attribute this exceedance to numerical uncertainties of the ACM at high loadings. Another difference is an increasing design space for increasing C_T. This is a key feature of the VAWT that enables similar power production for different azimuthal loading distributions, which significantly increases rotor design possibilities. This phenomenon is adressed by Madsen [30] and Simão Ferreira [15] [16].

The decoupling of the rotor's power production and its instantaneous loads implies that optimal *loadforms* can be derived for multiple purposes, e.g. power maximization/minimization and thrust minimization. These optimal loadforms can then inversely be transformed into required pitch sequences.

5.2 Loadform optimization

For the optimization Matlab's Optimization Toolbox will be used. The built-in function `fmincon` applies a Sequential Quadratic Programming (SQP) scheme to search for the for

a minimum value in a certain function, in this case the ACM. In this fashion, the reference Q_n from Chapter 3 will be updated until the design target is reached. As mentioned, the optimized Q_n will be then referred to as the loadform.

The loadform optimization problem can be regarded as a nonlinear optimization problem since its objective function ($C_{P,opt}$ or $C_{T,opt}$) and constraints are nonlinear. The backbone of the SQP algorithm is Newton's method for unconstrained optimization, as each next approximation in the iteration is found by minimizing a quadratic model of the objective function. This search for the mimimum value is performed using the method of Lagrange multipliers. By repeating this quadratic programming, a (hopefully) converging sequence of approximations is established, hence the name Sequential Quadratic Programming. The user must be critical with respect to the obtained mimimum after the optimization has terminated in the sense that it must indeed be the global minimum instead of a local one. In case of the latter, the optimizer's initial conditions or step size must be altered so as to circumvent the local minima at which it gets stuck.

A set of reference loadforms is created for different tip-speed ratios and solidities - $\lambda = [2, 3, 4, 5, 6]$, $\sigma = [0.06, 0.08, 0.10, 0.12]$ - which will serve as initial guess for the optimizer. The reference loadings for a $\sigma = 0.1$ rotor are shown in Figure 5.2, together with their corresponding ideal power production. A complete overview of the reference performance is shown in Figure 5.4. For the optimization, two types of loadform bounds will be investigated: global bounds and local bounds. The former will be applied just to demonstrate the validity of the optimizer, whereas the latter will provide the actual target loadforms. The optimization targets investigated here will be: 1.) maximizing C_P without increasing C_T, 2.) minimizing C_P and 3.) minimizing C_T while maintaining a certain C_P.

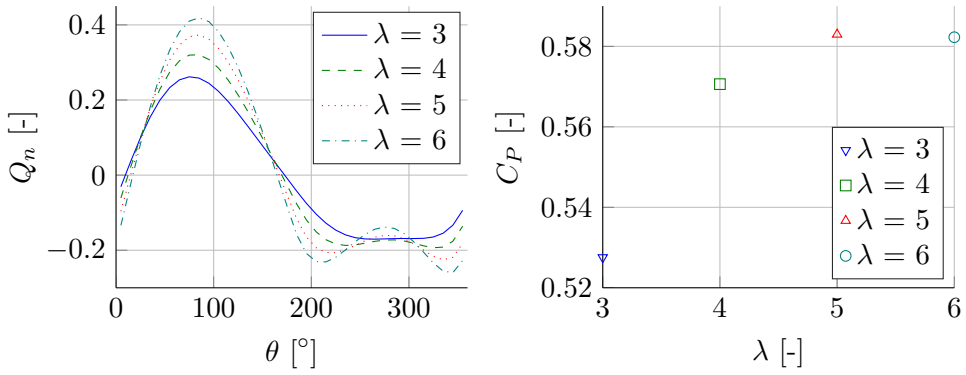

Figure 5.2: *Reference loadforms and corresponding ideal power production for* $\sigma = 0.1$.

Depending on the case, nonlinear constraints exist to ensure that the optimizer looks for maximum/minumum power (or thrust) while maintaining the same thrust (or power). In other words, this constraint has to keep the optimizer from simply changing the thrust (or power) in order to obtain maximum/minimum power (or thrust). An overview of the various cases and corresponding nonlinear constraints is given in Table 5.1, in which $f(x)$ is the optimization function and x is the underlying variable.

Table 5.1: *Overview of optimization cases and corresponding constraints.*

Case	Target	$f(x)$	x	Nonlinear constraint
1	$C_{P,max}$	$-C_P$	Q_n	$\int_0^{2\pi} Q_n \sin\theta \, \mathrm{d}\theta = C_{T,ref} \pm f_{C_{T,margin}}$
2	$C_{P,min}$	C_P	Q_n	$\int_0^{2\pi} Q_n \sin\theta \, \mathrm{d}\theta = C_{T,ref} \pm f_{C_{T,margin}}$
3	$C_{T,min}$	C_T	Q_n	$\int_0^{2\pi} Q_n \frac{V_n}{V_\infty} \mathrm{d}\theta = C_{P,ref} \pm f_{C_{P,margin}}$

5.2.1 Sanity check - power maximization with global bounds

In this optimization procedure, a global bound is chosen as a percentage of the maximum occuring loading of the reference loadform. This bound then applies to all 36 control points, i.e.

$$Q_{n,opt} \in [\pm f_{\Delta Q_n}^{\text{global}} \cdot \max(Q_{n,ref})]. \tag{5.2}$$

In the work of Madsen et al. [31] it was found that the optimum loadform for maximum power will approach a uniform distribution. A similar result is found here, as is visible in Figure 5.3. This result is rather arbitrary, since the loadforms will just assume a uniform distribution at a chosen percentage of the reference loadform's maximum. The user therefore indirectly defines the power increase by choosing $f_{\Delta Q_n}^{\text{global}}$. This result does, however, function as a sanity check of the optimizer, since it provides the expected uniform loadform for a given global bound.

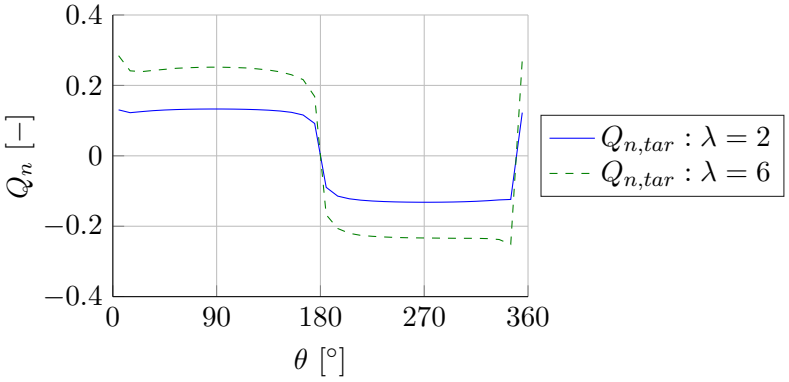

Figure 5.3: *Loadforms with* $f_{\Delta Q_n}^{\text{global}} = 75\%$ *and* $\sigma = 0.1$.

5.2.2 Optimization with local bounds

Contrary to global bounds, when defining local bounds the maximum allowed deviation from the reference loadform is constant for all control points, i.e.

$$Q_{n,tar} \in [Q_{n,ref} \pm f_{\Delta Q_n}^{\text{local}} \cdot \max(Q_{n,ref})]. \tag{5.3}$$

In this section, different values for $f_{\Delta Q_n}^{\text{local}}$ will be tested for the various optimization targets to investigate its influence on the actuator cylinder's performance, for $\sigma \in [0.06,\ 0.12]$ and $\lambda \in [2,\ 6]$. In Figure 5.4 an overview of the ideal performance of the reference turbine is shown. It is known for the ACM's results to become less accurate for an increasing rotor

loading. Results obtained in the region of high λ, σ (where C_T is high) are considered to be less trusthworthy than those obtained for lower rotor loadings and must therefore be critically assessed.

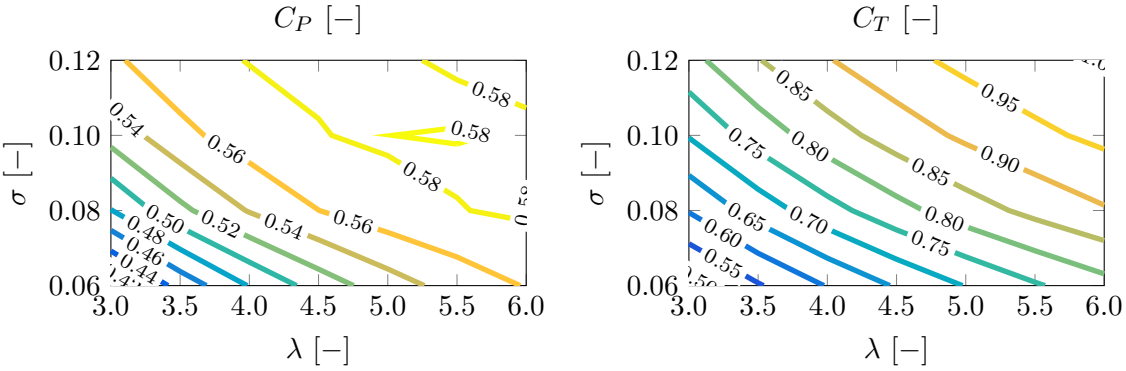

Figure 5.4: *Reference C_P and C_T.*

Power maximization

In Figures 5.5, 5.6 and 5.7, the maximized C_P and its relative improvement with respect to the reference C_P is plotted for different bounds. Comparing the three figures, it is found that the C_P improvement increases when the allowance in deviation of $Q_{n,tar}$ from $Q_{n,ref}$ is relaxed. This can be attributed to the fact that the loadform is more free to choose a specific shape that yields a larger power increment. However, the difference in power increment potential between allowances of 30% and 50% is negligible, which more clearly visible in Figure 5.16. A striking phenomenon that occurs in each of the figures is that of a higher achievable C_P increase for high values of λ and/or σ. For an ideal rotor this can be explained as follows. High tip-speed ratios cause the airfoil's tangential velocity, V_t, to be relatively large compared to the airfoil-normal component, V_n, which results in a reduced angle of attack. However, the higher tangential velocity will result in a higher absolute relative velocity and therefore a higher normal body loading Q_n, and thus it follows from equation (3.22) that a higher C_P increase is possible.

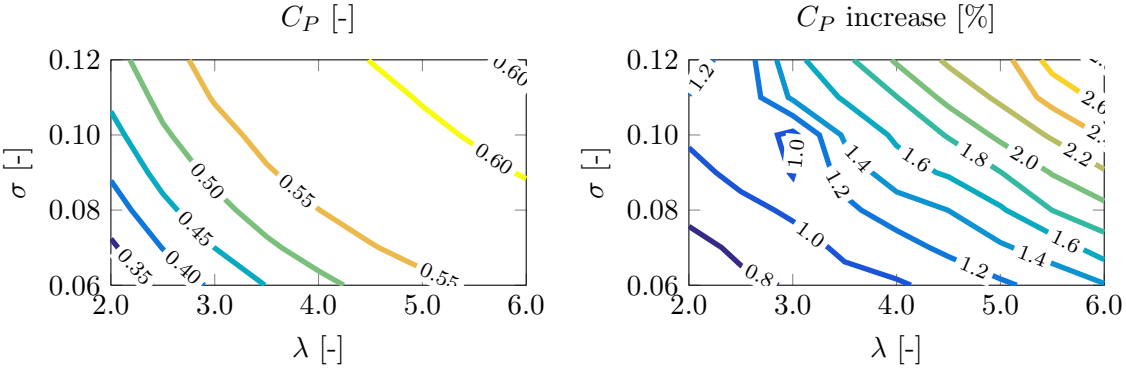

Figure 5.5: *Optimized C_P and its relative improvement for $f_{\Delta Q_n}^{\text{local}} = 15\%$*

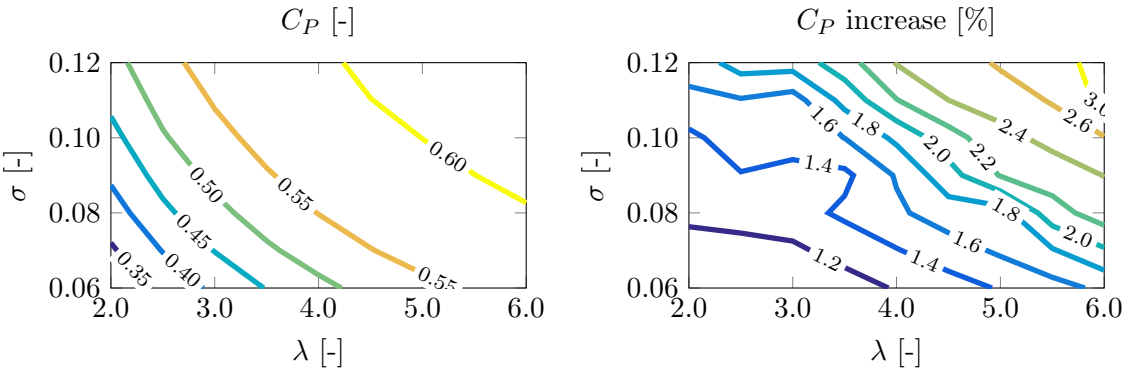

Figure 5.6: *Optimized C_P and its relative improvement for $f_{\Delta Q_n}^{\text{local}} = 30\%$*

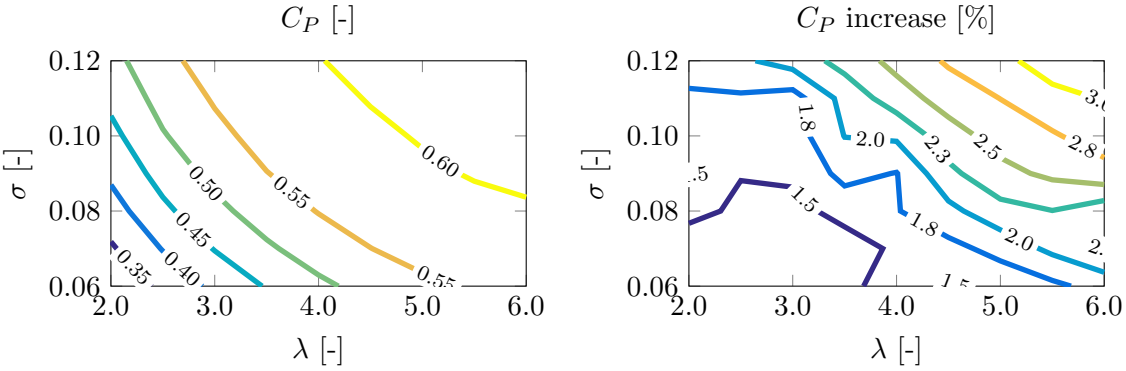

Figure 5.7: *Optimized C_P and its relative improvement for $f_{\Delta Q_n}^{\text{local}} = 50\%$*

An increase in σ simply results in larger pressure jumps over the cylinder surface, hence a bigger C_P maximization potential.

Power minimization

Comparing the results for the case of C_P minimization - Figures 5.8, 5.9 and 5.10 - to those that belong to C_P maximization, it can be concluded that alleviating C_P is more easily achieved than increasing it. For a loadform allowance of 50%, ideal power decrements of 15% are documented, whereas increments only went up to around 3%. Therefore, the necessary allowance on the loadform deviation for a significant ΔC_P is less for power alleviation than for its increment. It is therefore concluded that there is a high control potential for the VAWT to decrease its C_P when it operates beyond rated power. Regions that yield the highest power relief potential are that of either high σ and low λ or low σ and high λ.

The optimization is carried out under the same nonlinear constraint as for the C_P improvement (see Table 5.1). However, while it is important that during the C_P increase the total thrust is maintained (and not increased), alleviating C_P while simultaneously relieving the rotor from an amount of loading is only beneficial. For now, the constraint is there to allow for a proper comparison between the optimization cases. Furthermore,

completely removing this constraint will cause the optimizer to choose a loadform corresponding to zero thrust, which will probably not be achievable from a pitch-rate point of view. Therefore, the possibility of power alleviation and simultaneous thrust relief will be addressed in Chapter 6, since the active pitch behaviour will directly be assessed here.

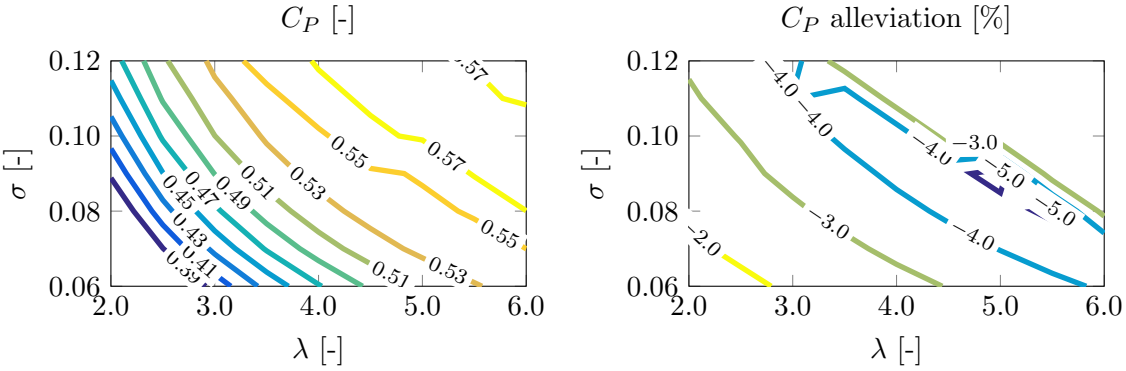

Figure 5.8: *Optimized C_P and its relative alleviation for $f^{\text{local}}_{\Delta Q_n} = 15\%$*

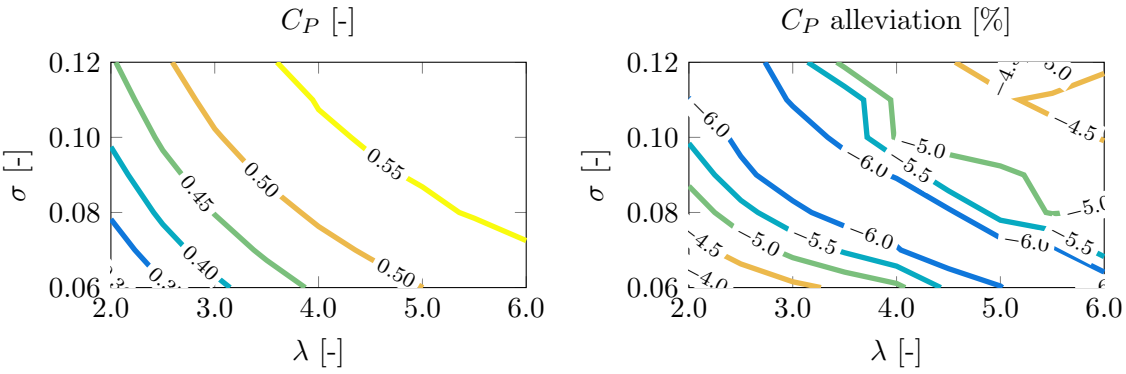

Figure 5.9: *Optimized C_P and its relative alleviation for $f^{\text{local}}_{\Delta Q_n} = 30\%$*

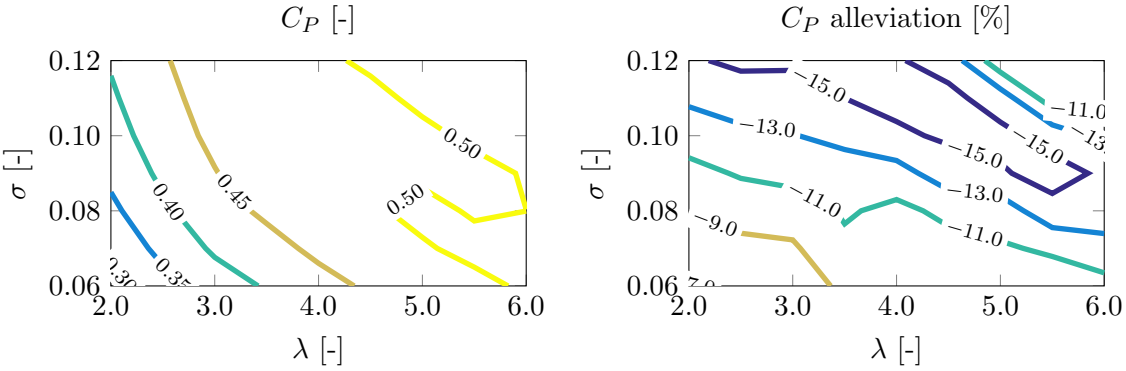

Figure 5.10: *Optimized C_P and its relative alleviation for $f^{\text{local}}_{\Delta Q_n} = 50\%$*

Thrust minimization

Relieving the rotor from thrust will lead to a lower cyclic loading on the blades. From Figures 5.11, 5.12 and 5.13 it is observed that, similar to the power maximization case,

the most effective area for alleviating the thrust is that of a high $\lambda - \sigma$. This is due to the fact that in this area the normal blade loading Q_n will be high compared to lower $\lambda - \sigma$, and it follows from equation (3.19) that a relatively large decrement ΔC_T is possible. This phenomenon is also visible in Figure 5.1, where the design space for thrust relief is large at high C_P.

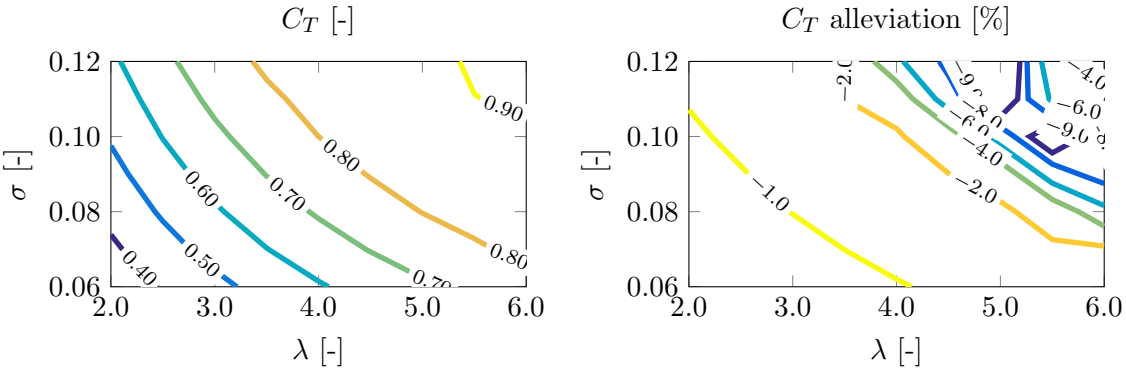

Figure 5.11: *Optimized C_T and its relative alleviation for $f^{\text{local}}_{\Delta Q_n} = 15\%$*

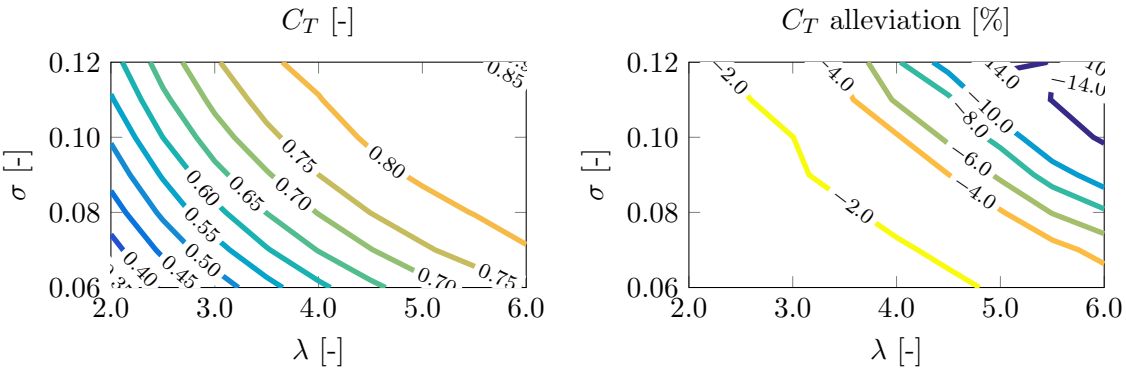

Figure 5.12: *Optimized C_T and its relative alleviation for $f^{\text{local}}_{\Delta Q_n} = 30\%$*

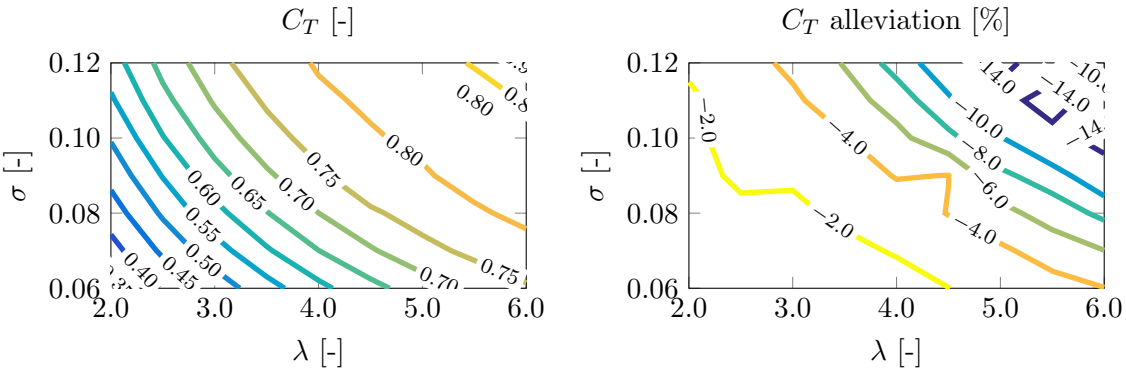

Figure 5.13: *Optimized C_T and its relative alleviation for $f^{\text{local}}_{\Delta Q_n} = 50\%$*

5.2.3 Elaboration on the aerodynamic quantities

In order to properly understand how the VAWT's aerodynamic quantities are changed from their reference value for the optimization purpose, this section will evaluate and discuss various siginificant parameters. Focus will be on the most critical cases, that is, with the highest allowance $f_{\Delta Q_n}^{\text{local}}$. Figure 5.14 provides an overview of relevant local blade parameters for varying tip-speed ratio and fixed solidity. This enables a proper comparison between the impact of the three optimization cases as a function of λ.

For each of the three cases, the direct output of the optimizer is the blade loading Q_n. It is observed that the loadform of Case 2 shows a considerable different behaviour than that of the other two cases. This can be explained according to the axial induction, w_x. The larger the induction velocity, the smaller the windspeed downwind of the turbine and

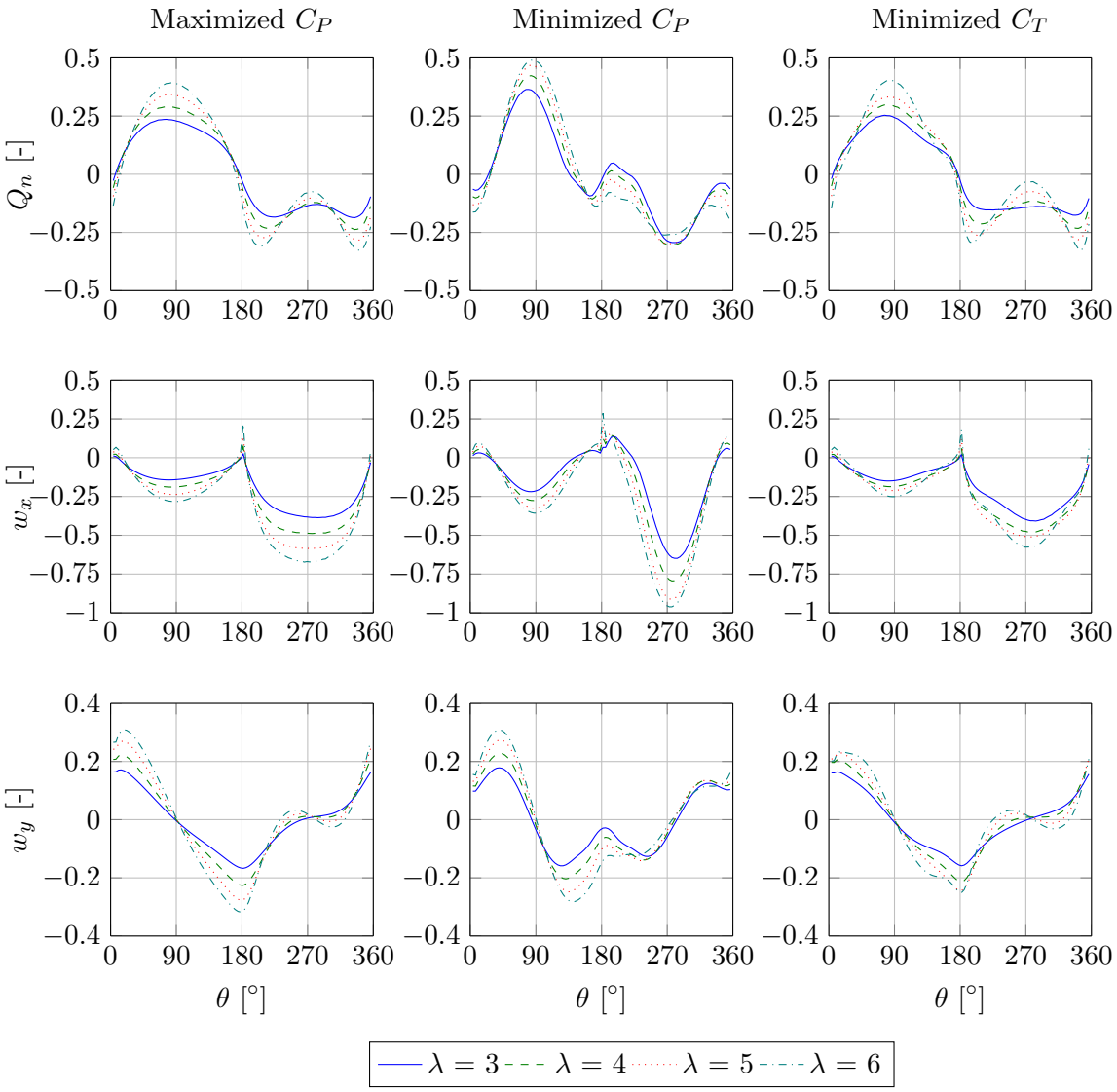

Figure 5.14: *Optimized loadforms for* $\sigma = 0.1$ *and* $f_{\Delta Q_n}^{\text{local}} = 50\%$.

the larger the power extracted from the wind.

So for the power minimization case small axial induction velocities are expected. However, the constraints defined in Table 5.1 ensure a similar integral value of the loadform, and therefore a similar integral induction. The optimizer therefore tactically chooses certain azimuthal positions at which it reliefs some if its induction, but has to compensate for this by increasing this value at other control points. It is observed that Case 2 shows an especially large axial induction on the downwind side of the rotor, at $\theta = 270^\circ$ azimuth, resulting in a negative local power production. If the integral thrust had been allowed to decrease as well while alleviating the power coefficient, the difference in induction would have been more pronounced. However, the limiting factor in alleviating C_P and C_T simultaneously is the necessary pitch to achieve this goal, and during loadform optimization this parameter can not directly be assessed. This topic will therefore be addressed in Chapter 6.

A certain similarity is observed between the resulting loadforms and induction velocities of Case 1 and Case 3. When the power coefficient is improved, the $C_T - C_P$ curve experiences an upward vertical translation (the C_P increment). Effectively this can also be regarded as the actuator cylinder producing less thrust for the same power. The opposite also holds, that is, when alleviating the thrust and the $C_T - C_P$ curve shifts to the left (the C_T decrement), this can also be interpreted as an increment in power for the same thrust. This reasoning explains the fact that the aerodynamic quantities for Case 1 and Case 3 show similar behaviour.

5.2.4 From loadform to pitch sequence

This method takes the derived loadforms as target and finds the necessary pitch sequences to obtain each of these. The procedure is as follows. First, a target loadform is inserted in the Mod-Lin ACM, from which the induced velocities (w_x, w_y) are calculated, without iteration. Second, the axial and tangential local velocities are calculated, from which the total airfoil-relative velocity (V_r) and angle of attack (α) are obtained. Note that θ_p is not yet taken into account here. Third, equation (3.13) is substituted into equation (3.15), and rewritten such that a direct expression for $C_{l,tar}$ as a function of $Q_{n,tar}$ is obtained, which takes the form:

$$C_{l,tar} = \frac{1}{\cos\alpha}\left(\frac{2\pi}{\sigma}\frac{V_\infty^2}{V_r^2}Q_{n,tar} - C_d\sin\alpha\right). \tag{5.4}$$

The fourth and final step is to calculate the required pitch ($\theta_{p,req}$) by accounting for pitch in the expression for the lift coefficient: $C_l = C_{l,\alpha}\sin(\alpha - \theta_p)$. Substiting $C_{l,tar}$ for C_l, the required pitch is calculated from

$$\theta_{p,req} = \alpha - \arcsin\left(\frac{C_{l,tar}}{C_{l,\alpha}}\right). \tag{5.5}$$

Some of the obtained pitch sequences are plotted in Figure 5.15, where it is observed that they are rather oscillatory, rapidly varying between positive and negative values. One can imagine the impact of the resulting aerodynamic loads on the fatigue life of the blades, not the mention the necessary capabilities of the pitch mechanism to obtain

such sequences. With the current optimizer, one can only manage the controlability of the obtained sequence indirectly, by adding or changing constraints on the loadform, and checking the resulting pitch curve after the iterations have terminated. This is a rather cumbersome process for ensuring feasible sequences.

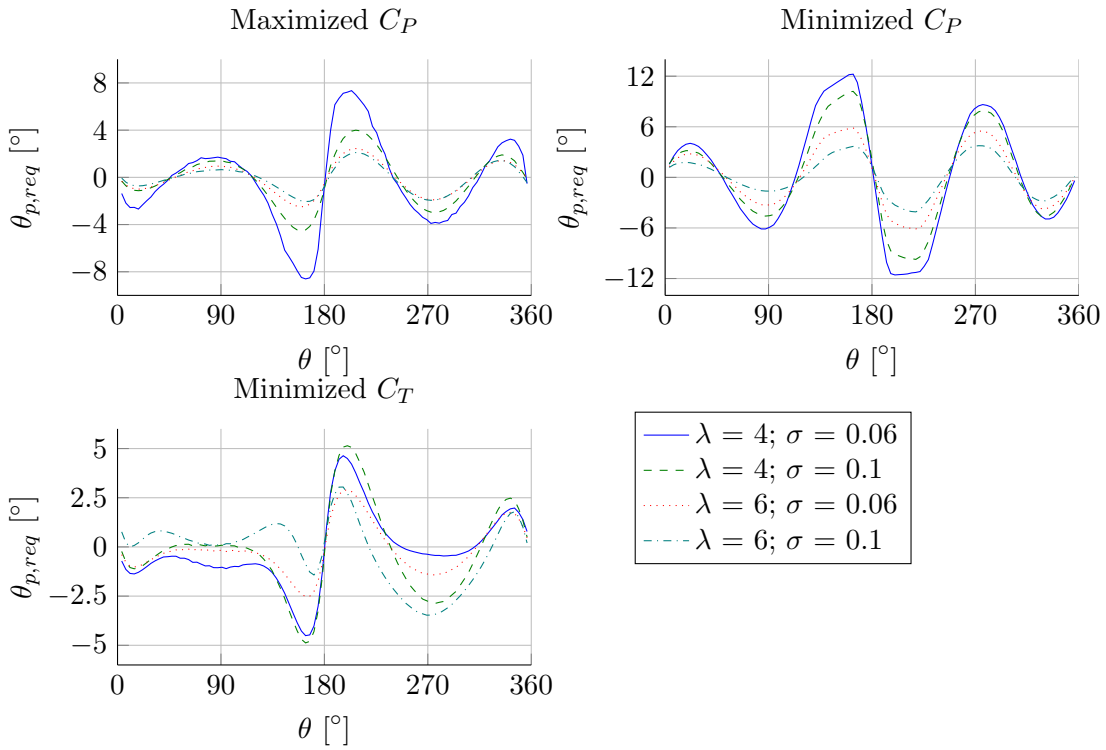

Figure 5.15: *Required pitch sequences to obtain optimized loadforms, with* $f_{\Delta Q_n}^{\text{local}} = 50\%$.

5.3 Chapter conclusions

An inherent feature of the VAWT's energy conversion is its ability to produce a different power under the same loading and vice versa. This chapter aimed at exploring the ideal VAWT's potential in terms of power increase, power alleviation and thrust relief, by utilizing the steady ACM, implemented in Chapter 3, to optimize the nondimensionalized blade loading Q_n on each of the 36 control points along the cylinder surface. In doing so, the following traits and limitations have been exposed.

- A uniform loadform with moderate blade loading gives a higher C_P and lower C_T than the characteristic peaky loadform with a higher maximum loading.
- The optimization potential of the VAWT does not increase linearly with the loadform allowance. This can clearly be observed in Figure 5.16, where the maximum improvements for a rotor with $\sigma = 0.1$ are displayed.
- Provided the same control authority, the VAWT is more efficient in minimizing its C_P than in maximizing it. This is partly due to the fact that a limit exists for

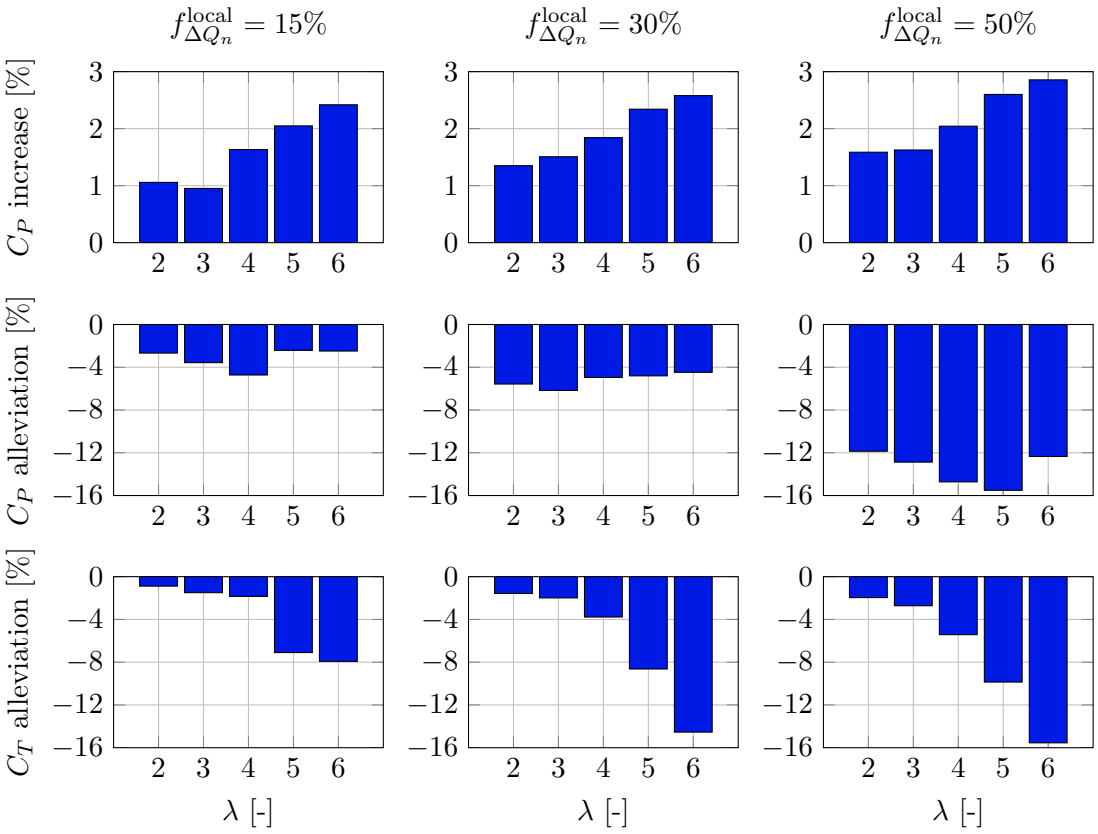

Figure 5.16: *Comparison of perfomance improvements for an ideal rotor with* $\sigma = 0.1$.

the maximum achievable power, i.e., the Betz limit. Additionally, the efficiency of the reference turbine is already close to the Betz limit and therefore allows for only little improvement.

- Loadform optimization does not allow the user to set constraints on the pitch angle directly. Therefore, the feasibility of the obtained target loadforms can only be assessed after the optimization through the inverse method. In case the resulting pitch curves do not satisfy the user's, one has to add or change the constraints on the loadforms and run the optimizer with the new settings, which is a rather cumbersome process of ensuring feasible sequences. Furthermore, since the pitch is not explicitely taken into account during the optimization, this method is limited to the case of an ideal rotor.

- The numerical uncertainty of the Mod-Lin correction factor utilized in the ACM increases with thrust. The user should therefore critically assess any optimized quantities at high values of C_T. The results presented in this chapter indeed show the highest gains for power increase and thrust relief at regions of high loading. Possibly, the ACM overestimates C_P/C_T here (see Figure 5.1, where some loadform shapes even exceed the Betz limit), and thus it makes sense that this is the region where the highest potential is obtained. It can therefore be concluded that the ACM might not be the best optimization tool for an ideal rotor.

Chapter 6

Optimization of a Rotor under Realistic Flow Conditions and Geometry

The previous chapter was an exploratory study into the maximum design potential of a VAWT, for which an ideal rotor was considered. The current chapter aims at optimizing the behaviour of a turbine in more realistic flow conditions, including the effects of drag and a viscous airfoil polar. Instead of inversely obtaining pitch sequences after the *load-form optimization*, the method applied here will be a *direct pitch optimization*. This has two main benefits over former method: 1.) the user can set constraints on pitch allowance during the optimization instead of assessing the feasibility of the inversely obtained sequences after the optimization procedure, and 2.) for each iteration step, influence of the current pitch settings on the angle of attack, blade loadings and power can easily be included.

Contrary to the ideal rotor optimization the ACM expression for the real rotor power, that is, equation (3.23), will be used here. This expression includes both the normal and tangential force effects on power by translating them with the respective pitch angles. Aerodynamic forces follow from the viscous lift and drag polar of the symmetrical NACA0018 airfoil for a Reynolds number $Re = 3\ 000\ 000$, which can be found in Appendix A. In order for the optimizer to have a fast convergence towards the global minima a different set of reference properties is created, including drag and the NACA0018 airfoil properties. An overview of the performance of this reference turbine in terms of C_P and C_T in quasi-steady flow is provided in Figure 6.1. Comparing this behaviour to the ideal case it is observed that maximum power production is no longer found at the highest λ, σ. At low tip-speed ratios, high angles of attack occur and therefore viscosity and drag have a large impact on the power production. For high tip-speed ratios, the local tangential velocity is high, which also results in a large drag force and a reduced power production. This explains the area of maximum C_P at a moderate λ.

The performance of the same reference turbine is plotted for unsteady flow conditions in

Figure 6.2. As explained in Chapter 4 the degree of unsteadiness is partly determined by the number of blades, which arbitrarily chosen as $B = 3$ throughout this chapter. The expected effect of a higher or lower number of blades is discussed in Section 6.2. Comparing the steady to the unsteady performance, a significant reduction is observed in the maximum power region whereas only a small decrease in thrust is concluded.

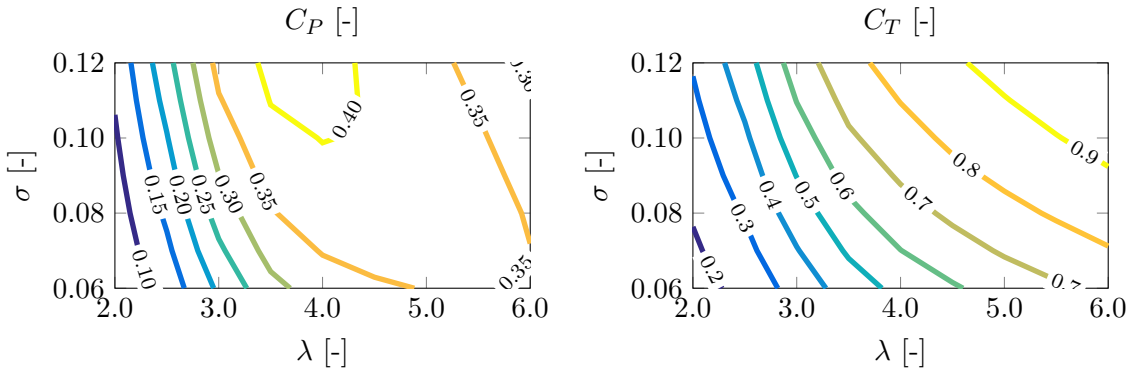

Figure 6.1: *Performance of reference turbine with the NACA0018 airfoil, quasi-steady flow conditions.*

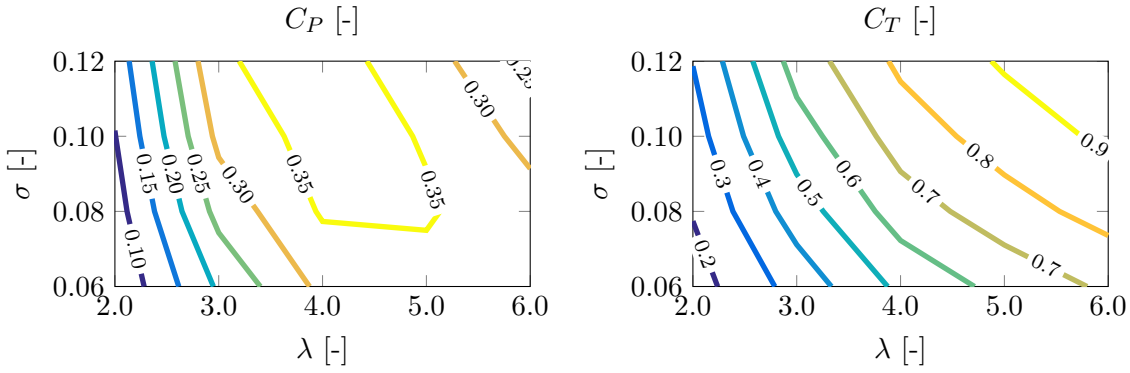

Figure 6.2: *Performance of reference turbine with the NACA0018 airfoil, unsteady flow conditions with $B = 3$.*

After a brief explaination of the implementation of the pitch optimizer, the model will be applied to the described reference turbine to optimize its performance for the following targets: 1.) Maximum power without increasing thrust, 2.) Minimum power, 3.) Minimum thrust without losing power. This chapter is divided into two parts: the first part still assumes an infinite number of blades (so quasi-steady flow contidions), whereas the second takes into account unsteady effects within the optimization routine.

6.1 Direct pitch uptimization for steady flow

Unlike the method of loadform optimization, the initial guess of `fmincon` will now be zero since no pitch is involved in the reference turbine. Therefore, a function must be prescribed to the pitch sequence that ensures the feasibility of the optimization. Desirable

properties for the pitch curve are its smoothness and periodicity. A 10^{th} order Bezier curve is chosen as the design medium. A Bezier curve is a parametric curve that is based on the Bernstein polynomial. The algorithm constructs a curve around $n+1$ control points (n being the order of the polynomial) by performing n linear iterations between those points to obtain a single location on the curve. A total of $m \times n$ iterations has be be executed (m being the chosen number of evaluation points) in order for the algorithm to construct the curve.

The azimuthal Bezier coefficients are linearly spaced along the rotor's circumerence and are fixed throughout the optimization. The distribution of pitch-controlling Bezier coefficients is the optimization function for `fmincon`, and in order to ensure periodicity a constraint is set such that Bezier coefficients at $\theta = 360°$ are equal to those at $\theta = 0°$. So the optimization function is the distribution of Bezier control points about which a pitch curve will be constructed after the iterations have finished. Optimization of Bezier coefficients forms a robust method of (almost) directly optimizing the pitch sequence. In this chapter, the obtained optimum pitch sequences for $\lambda \in [2;\ 6]$ and $\sigma \in [0.06;\ 0.12]$, under different pitch actuation limits will be presented and elaborated on.

Power maximization

For this objective the optimization target is set as $-C_P$. The constraint that kept the C_T from increasing during loadform optimization is implemented here as well. Contour plots of the optimized C_P and its relative improvements, for pitch actuation limits of $\pm 1°$, $\pm 3°$ and $\pm 5°$, are shown in Figures 6.3, 6.4 and 6.5, respectively. A striking phenomenon that occurs for each of the three pitch authorities is the very high relative C_P improvement at low λ. The reason for this is the relatively low reference C_P, allowing for a large design space here. However, since the obtained C_P values are still low, these operation conditions are still uninteresting when aiming for maximizing the VAWT's power production. The lowest C_P improvement is obtained at the initial maximum value. Apparently, an active pitch mechanism is too rough for enhancing the flow characteristics without inducing too much drag. It is therefore concluded that in order to increase the VAWT's maximum power a more refined circulation control method, such as active flap control, is required. An explaination for this is that the method of pitch control still operates on the same lift and drag polar, only increasing or decreasing the geometric angle of attack. Active flap control allows for locally changing the effective airfoil camber, which might result in more efficient aerodynamic behaviour. Additionally, the usage of a different airfoil, with a more desirable drag polar, could also be beneficial for obtaining a higher $C_{P,max}$. Finally, it is observed that even though the maximum power has not increased much, the region in which this power occurs can be expanded by pitching. This results in a larger operational window for power maximization, allowing the VAWT to have a lower σ and operate at a wider range of λ.

A more clear comparison of C_P gain potential for different pitch authorities, tip-speed ratios and solidities is provided in the histogram in Figure 6.6. The small potential for increasing the turbine's $C_{P,max}$ at $\lambda \simeq 4$ and $\sigma > 0.1$ is clearly visible, as it is between 0% and 2.5%. Overall the documented improvements are higher for larger pitch limits, however, for some cases an allowance of $\pm 5°$ results in a smaller ΔC_P than one or both of the other two actuation limits. There is no physical explaination for this behaviour

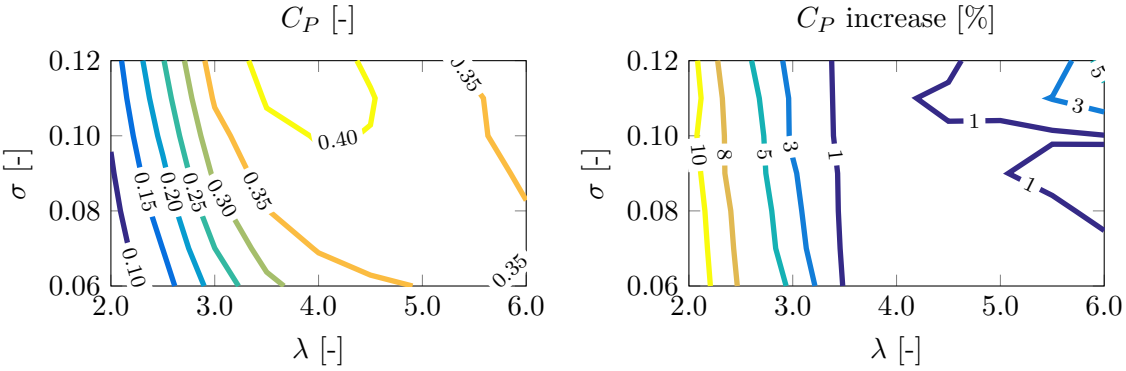

Figure 6.3: *Power increase for* $\theta_p \in [-1°;\ 1°]$.

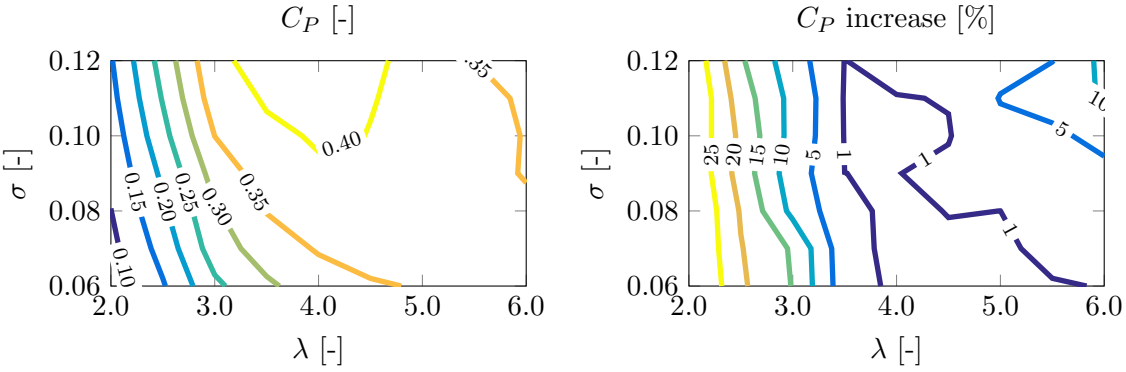

Figure 6.4: *Power increase for* $\theta_p \in [-3°;\ 3°]$.

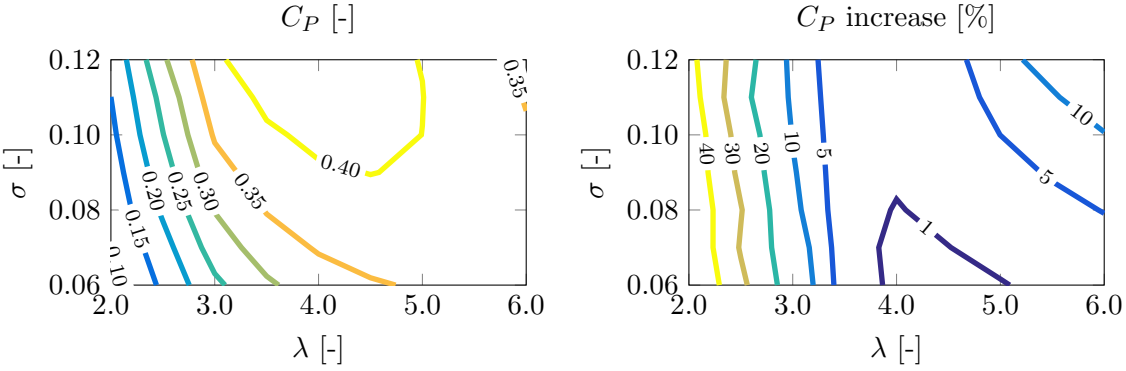

Figure 6.5: *Power increase for* $\theta_p \in [-5°;\ 5°]$.

since a larger actuation limit should always be capable of performing at least as well as smaller values. A more credible explaination for the inconsisent behaviour with respect to the pitch allowance is the fact that the optimizer converges towards a local minimum and the global minimum is not reached in these cases. This can be circumvented by changing the optimizer's step size and tolerances. A qualitative comparison between the results from the loadform optimizer and those of the current direct pitch optimization method points out that the latter aims at a constant performance increase for the entire range of

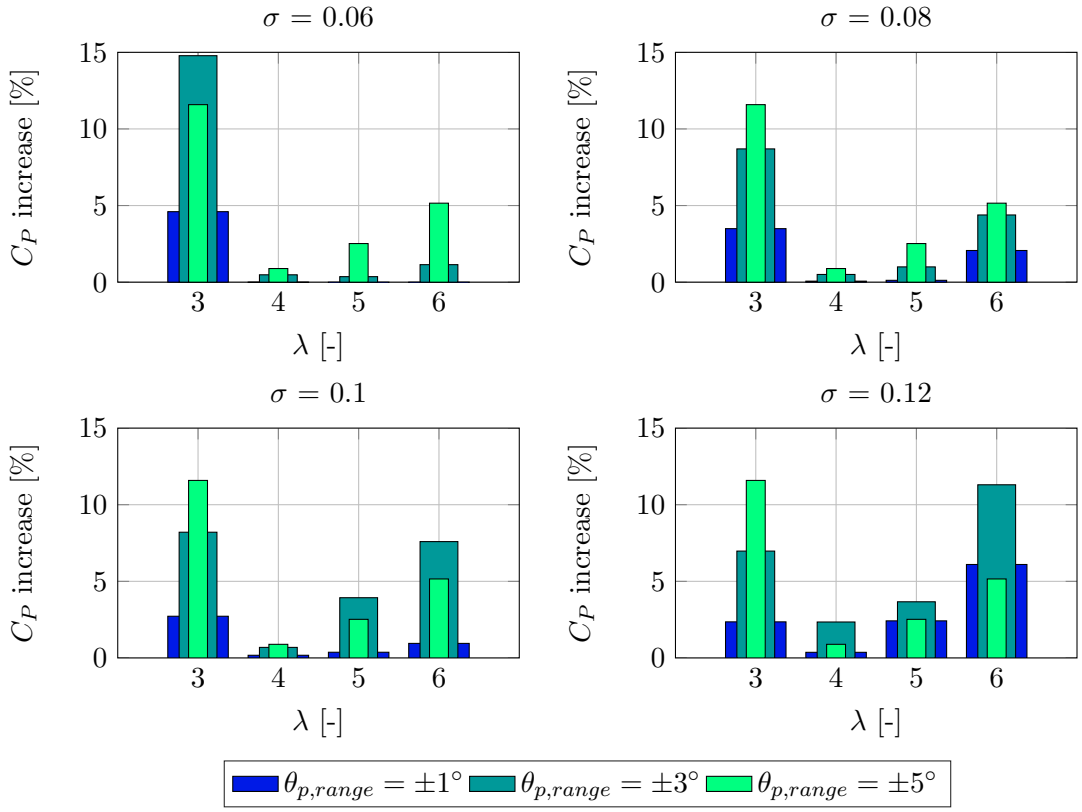

Figure 6.6: *Power maximization.*

tip-speed ratios, whereas the former shows a decrease in performance gain at lower values of λ.

The most extreme obtained pitch sequences for power maximization, i.e. for $\theta_p \in [-5°, 5°]$, are plotted in Figure 6.7. A first note has to be made considering the fact that some sequences are discontinuous at $\theta = 0°/360°$. This implies that an additional constraint is required that ensures smooth behaviour on the periodic interval. This non-smooth behaviour sometimes occurs in the other optimization targets as well. Further observing the pitch sequences, it must be kept in mind that positive pitch angles reduce the inflow angle whereas negative a pitch increases this angle. For $\lambda = 3$ the optimum pitch sequence is close to a sine shape, regardless of the solidity. A peak of 5° is reached around $\theta = 90°$, which corresponds to the blade position where the airfoil direction is perpendicular to the inflow velocity. For a low tip-speed ratio, the tangential velocity is low compared to the normal velocity (which is almost the same as the inflow velocity here) and therefore total inflow angle will be high. The airfoil will be in its stall region, where it looses its lift and has a large drag, so the optimum pitch sequence decreases this inflow angle to increase lift and decrease the drag. Opposite behaviour is observed when the tip-speed ratio is increased. The rotational velocity is high and an increase in inflow angle actually increases the obtained lift force and therefore the overall aerodynamic performance. In Figure 6.7 the pitch allowance is hit only for $\lambda = 3$ at an azimuthal position of 90°. This implies that increasing the pitch limit beyond values of 5° will actually not increase the maximum power production any further.

A better understanding of why the optimum pitch sequences assume the shape they have can be gained by looking at the local load distributions, plotted in Figure 6.8 for $\lambda = 3$ and $\sigma = 0.1$. The most significant improvement is found in the tangential loading on the upwind part of the rotor. The sudden drop that occurs in the reference curve, due to the airfoil entering its stall region, is circumvented by increasing the pitch to its maximum allowance and therefore reducing the angle of attack. This increases the torque, resulting in a higher local power production. Similar reasoning applies to the normal loading enhancement on the upwind part of the rotor, although differences form the reference curve are less pronounced here. Pitching in the downwind region is mainly executed to further reduce the normal load distribution on this part and therefore maintaining the same integral thrust as the reference turbine. The optimizer thus compensates for the gain in the upwind part by further decreasing the local loading in the downwind part. Apparently there is a high energy exchange efficiency in the upwind part of the rotor, for which the optimizer sacrifices some blade efficiency in the downwind part.

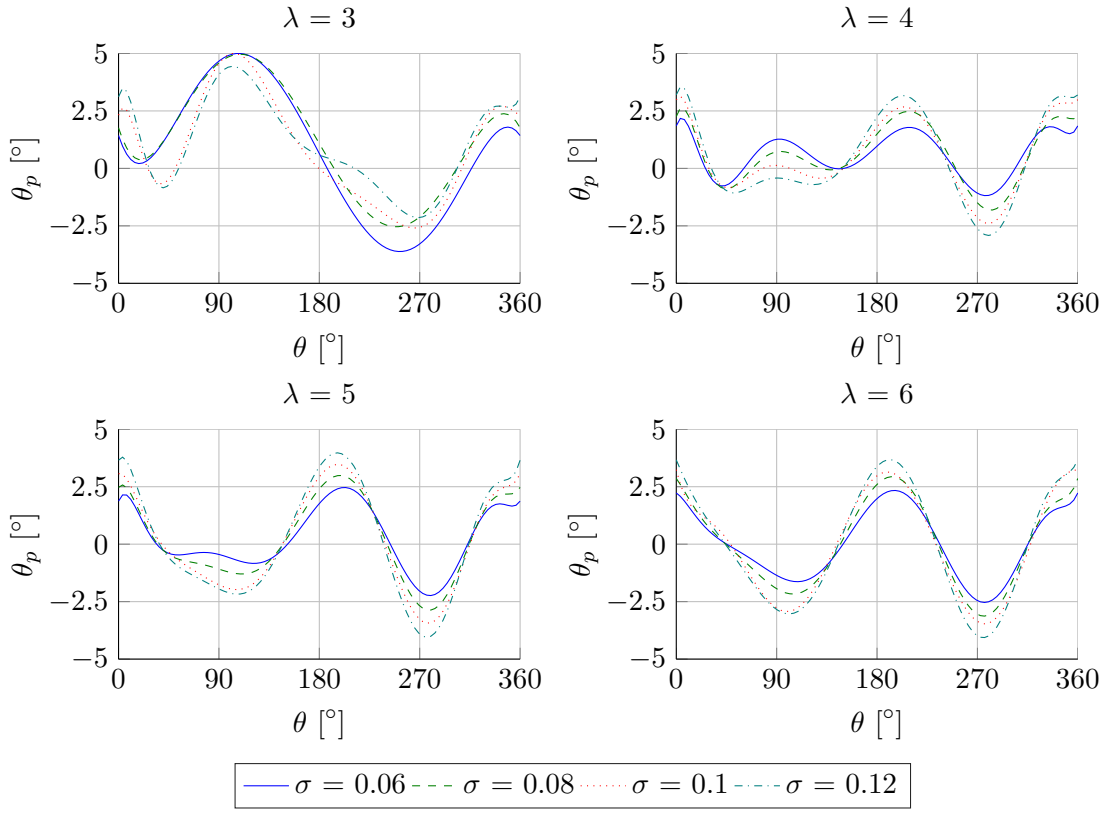

Figure 6.7: *Required pitch sequences to obtain maximum power.*

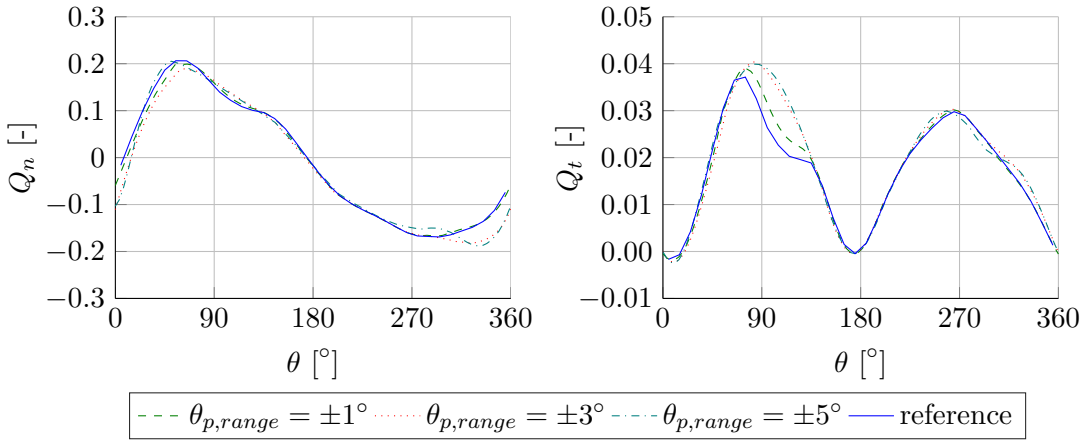

Figure 6.8: *Rotor loadings under optimized pitch sequences for $\lambda = 3$ and $\sigma = 0.1$ (power maximization case).*

Power minimization

For the optimizer to minimize the rotor's power, the design objective of `fmincon` is set as $+C_P$. For this purpose an additional pitch range of $\pm 10°$ is investigated, since it is found that this will result in significantly larger power reductions (unlike the case of power maximization, where respective gains beyond an allowance of $\pm 5°$ were insignificant). Contour plots of the optimization results are given in Figures 6.9, 6.10 and 6.11, for pitch ranges of $\pm 3°$, $\pm 5°$ and $\pm 10°$, respectivily. It is clear that the power alleviations achieved here are significantly higher than those achieved with the loadform optimizer. The reason for this is obvious, namely that the constraint on thrust is completely removed, since not allowing a C_T relief while alleviating C_P makes no sense. The degree to which the optimizer can decrease C_P and C_T is determined by the pitch allowance, so the user can ensure feasible pitch range in the end. An additional constraint that keeps the optimizer from choosing a design point in the generator region ($C_P, C_T < 0$) is implemented.

Increasing the pitch actuation limit results in a larger C_P alleviation. Additionally, it is observed that the highest relative alleviations occur either at low or high tip-speed ratios. For low tip-speed ratios the reference C_P is low and can easily be decreased to zero. For high tip-speed ratios, the optimizer can utilize occuring drag and viscosity effects to decrease its power.

Power alleviations for four pitch ranges - $\pm 1°$, $\pm 3°$, $\pm 5°$ and $\pm 10°$ - are compared in Figure 6.12. Unlike the power maximization case, the figure implies that global minima were found throughout, since higher pitch allowances result in a similar or larger ΔC_P. Furthurmore, it is clear that the potential for C_P alleviation on a VAWT using active pitch control is very high. For most λ, σ a linear relation between the actuation limit and the C_P reducal is concluded. For some cases with $\lambda \in [-10°, 10°]$ a C_P decrement in the range of 100% is documented, which can be attributed to drag due to viscous effects.

Optimum pitch sequences for a θ_p range of $\pm 10°$ are shown in Figure 6.13 for a variety of tip-speed ratios and solidity. For $\lambda = 5$ and 6, the full potential of the power decrement has been achieved without the pitch reaching the actuation limit. For all the tip-speed ratios, the optimum pitch curve is close to a sine with a negative mean value. For $\lambda = 3$, the

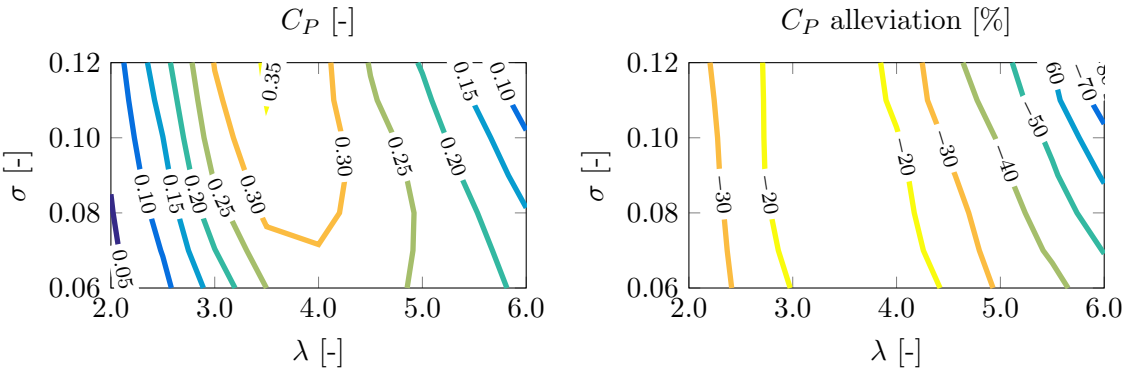

Figure 6.9: *Power alleviation for* $\theta_p \in [-3°;\ 3°]$.

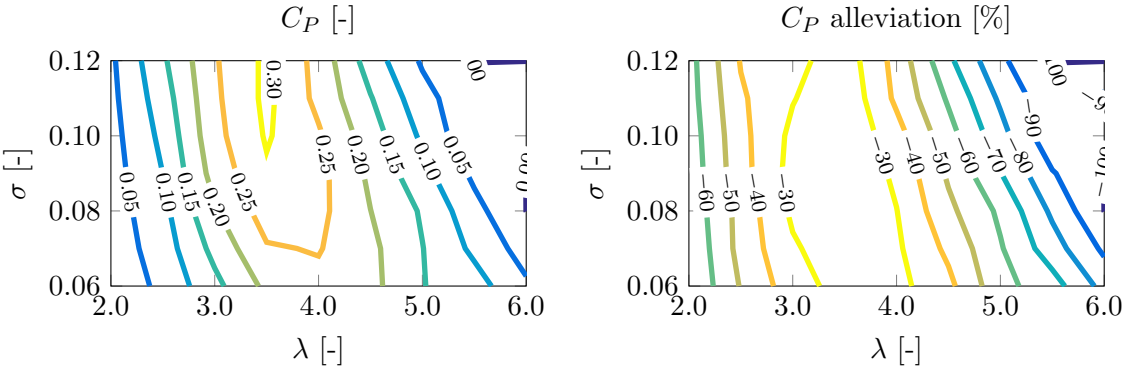

Figure 6.10: *Power alleviation for* $\theta_p \in [-5°;\ 5°]$.

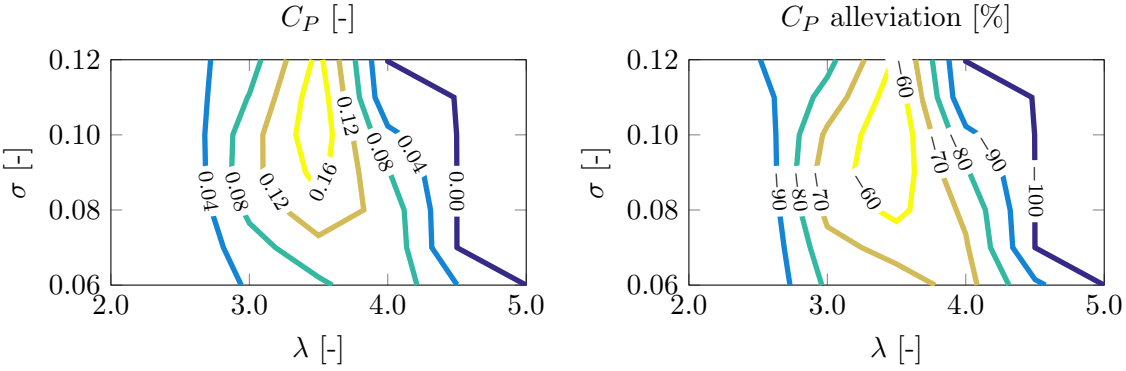

Figure 6.11: *Power alleviation for* $\theta_p \in [-10°;\ 10°]$.

sine wave is mirrored with respect to the other tip-speed ratios. Comparing this sequence to the corresponding curve for the maximization case, it is concluded that the trend is almost completely opposite. For azimuthal positions between 0° and 90°, which is the position on the azimuth where the relative velocity in windward direction is the highest, the optimizer produces a pitch that increases in negative direction up to −10°. Therefore, the total inflow angle is largely increased here and the airfoil operates in its stall region, causing a large drag effect, and therefore decreasing the rotor's power production in its

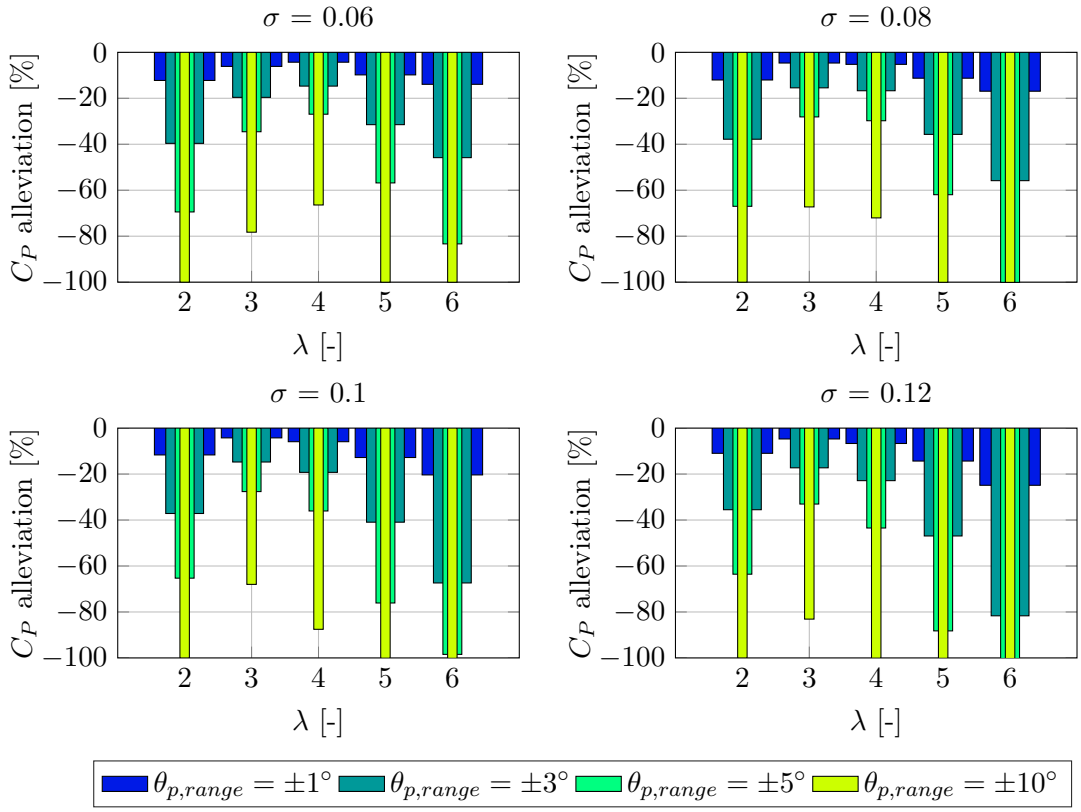

Figure 6.12: *Power minimization.*

most effective part. Beyond this azimuthal position, a deviating behaviour is observed between the different rotor solidities. Apparently, the rotor with the smallest solidity needs to push its pitch angles to higher values in the downwind part than the rotors with larger solidity. A possible explaination for this is that drag and viscosity effects are larger when the total relative blade area is larger, so a smaller angle is required to achieve a C_P decrement.

The opposite behaviour of the optimum pitch sequences for $\lambda = 4$, 5 and 6 with respect to that of $\lambda = 3$ is, again, explained due to the relatively high tangential velocity with respect to the inflow velocity, and the optimizer must decrease its inflow angle on the upwind part in order to reduce the lift and torque produced here. Also, a more similar behaviour of different rotor solidities is observed throughout the rotor's circumference.

Observing the local load distribution shown in Figure 6.14 it can be seen that the load-forms vary more from their respective reference curves than for the C_P maximization. The reason for this is the removal of the constraint on thrust, hence no compensation is required if the optimizer changes the loading in a certain part of the rotor. The loading is decreased almost everywhere on the rotor's azimuth, resulting in a smaller torque and power. The fact that the pitch sequence on the downwind side is not limited by the axial induction for the minimization case is one of the reasons why such high C_P decrements can be obtained.

The induction field of the C_P maximization and minimization case are plotted side-to-side

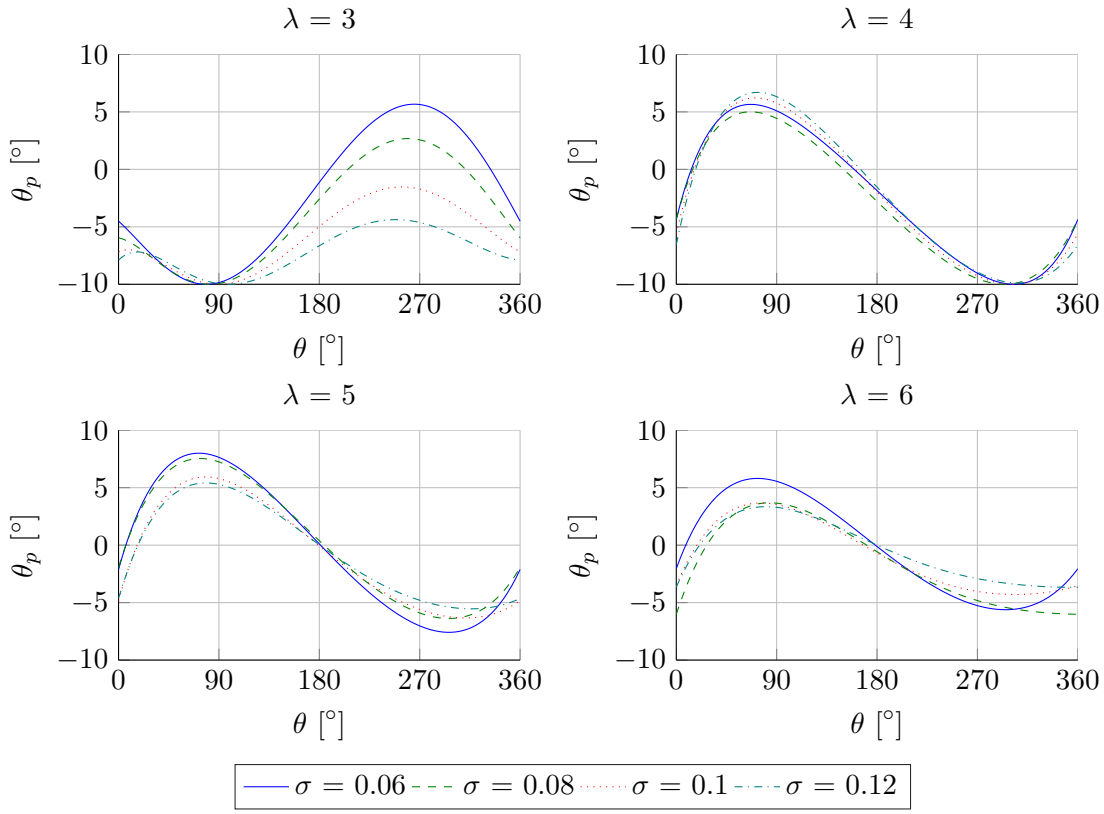

Figure 6.13: *Required pitch sequences to obtain minimum power.*

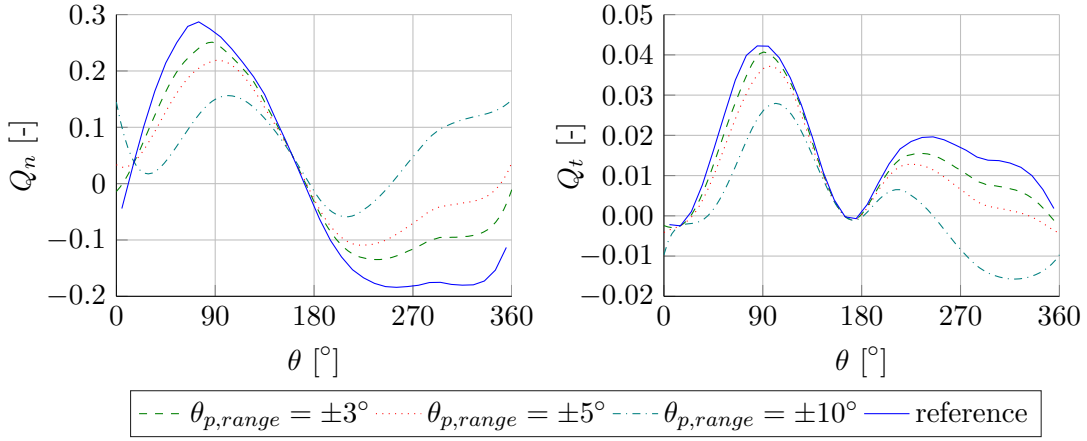

Figure 6.14: *Rotor loadings under optimized pitch sequence for* $\lambda = 4$ *and* $\sigma = 0.1$ *(power minimization case).*

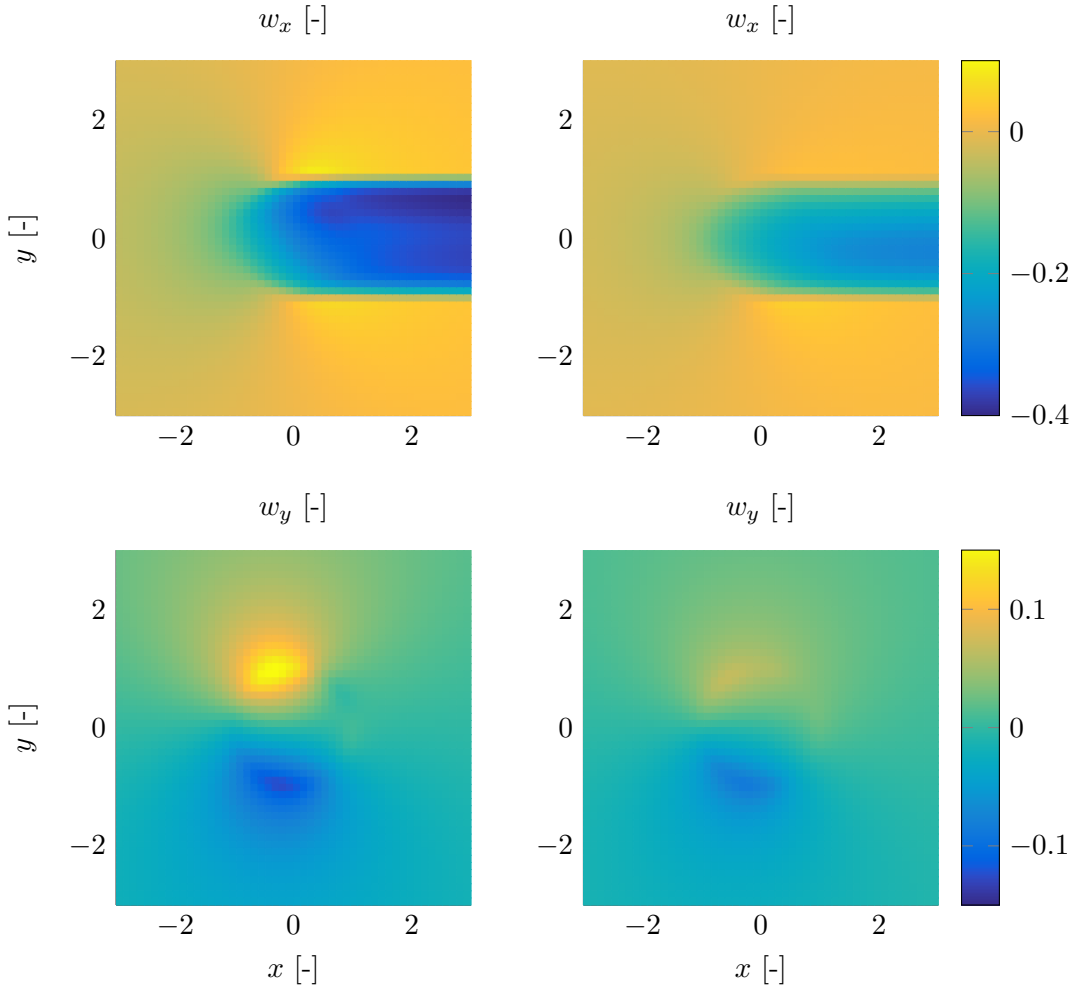

Figure 6.15: *Comparison of induction field for maximized (left column) and minimized (right column) power.*

in Figure 6.15. Comparing the fields it is observed that the optimum pitch sequence for increasing power results in higher induction values in the rotor wake, and therefore a lower wind speed, than the power minimization case. This is an obvious result since increasing the power production will have the rotor extracting more kinetic energy from the flow and therefore lowering its velocity. The relation between turbine's power output and its wake has been extensively used for wind farm optimization of HAWTs, and Figure 6.15 shows that such an optimization case exists for VAWTs as well.

Thrust minimization

The final optimization target investigated here is that of thrust minimization, where the `fmincon` objective is set to $+C_T$. Like in the loadform optimization, a constraint that keeps the optimizer from simply reducing C_P in order to achieve a minimum C_T is required. Observing the contours of the thrust-relieved rotor for different pitch limits in Figures 6.16, 6.17 and 6.18 it is concluded that, in general, rotors with a low solidity will

have a small potential of decreasing their thrust while maintaining power. Furthermore, the thrust relief potential is the lowest when the power is high, that is, for moderate tip-speed ratios around $\lambda = 4$.

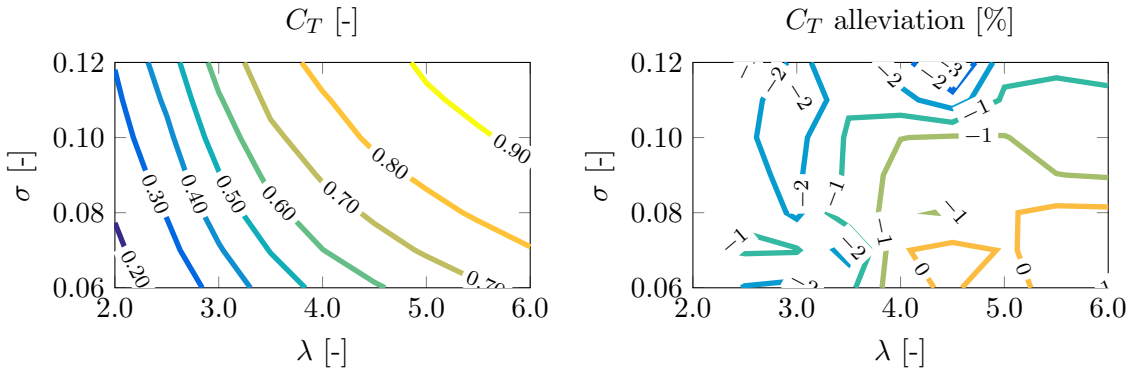

Figure 6.16: *Thrust alleviation for* $\theta_p \in [-1°;\ 1°]$.

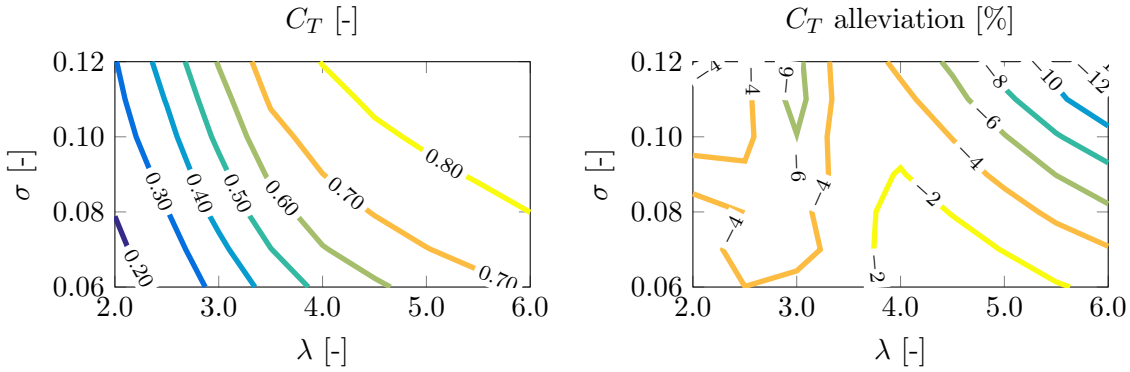

Figure 6.17: *Thrust alleviation for* $\theta_p \in [-3°;\ 3°]$.

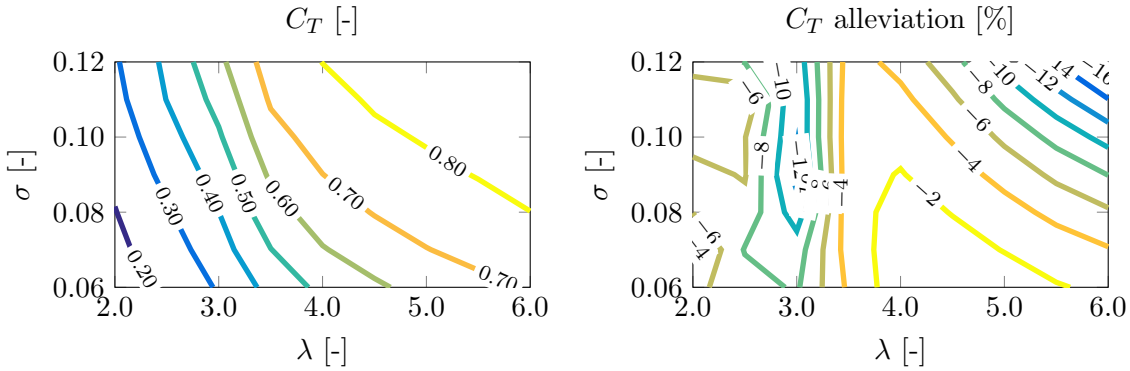

Figure 6.18: *Thrust alleviation for* $\theta_p \in [-5°;\ 5°]$.

Figure 6.19 shows an overview of the C_T decrement using active pitch on a VAWT. Again, global minima are found for all λ, σ, as increasing the pitch actuation limit results in a ΔC_T that is at least as high as for the the lower allowances. Overall, a tip-speed ratio of 3 has the highest potential, which is contributed to the occurance of stall on some

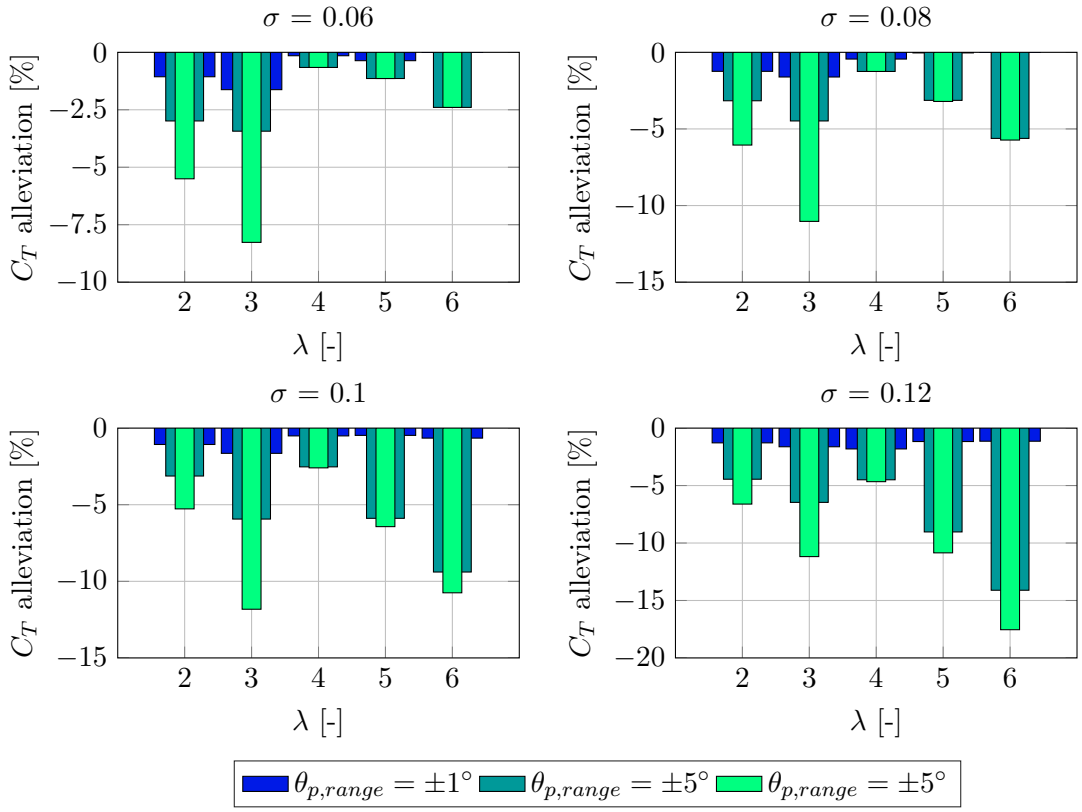

Figure 6.19: *Thrust minimization.*

azimuthal positions. The occurance of stall is beneficial for the optimizer, as it can now easily compensate for power losses simply by pitching the airfoil such that it avoids stall. Another striking feature is the decrement for $\lambda = 6$, which increases significantly with rotor solidity. Apparently, a rotor with a larger solidity is less sensitive to a change in local blade loading in terms of integral power production than a smaller-solidity rotor. This implies that a large-solidity rotor has a broad range of load distributions yielding a certain power, hence the optimizer is free to choose a specific shape within that range that corresponds to the lowest thrust.

The obtained load distributions for different pitch authorities, at a tip-speed ratio of 3, have been plotted in Figure 6.20. It is observed in the Q_n plot that the optimizer loses most of the thrust on the interval $\theta \in [255°, 330°]$. The Q_t plot shows that this is at the expense of the local power production. This loss in power is compensated on the interval $\theta \in [60°, 135°]$, where the airfoil is pitched such that it avoids stall. On this part of the azimuth, the optimizer therefore shows similar behaviour to the power maximization case, since the occurance of stall was also circumvented here.

Figure 6.21 shows a comparison between power maximization and thrust minimization pitch sequences for a $\sigma = 0.1$ rotor, and a large similarity is confirmed for $\lambda = 4, 5, 6$. As mentioned earlier, for lower tip-speed ratios the airfoil will encounter stall, which yields easy compensation for power losses. The pitch behaviour will therefore look similar to the power maximization case on the azimuthal interval where stall occurs, but approach different values on the remaining circumerential positions. For higher rotational speeds,

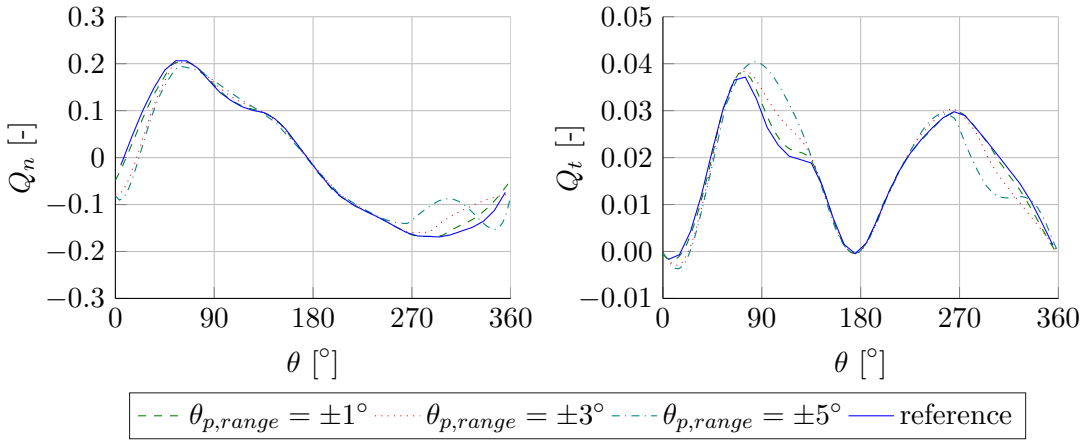

Figure 6.20: *Rotor loadings under optimized pitch sequences for* $\lambda = 3$, $\sigma = 0.1$ *(thrust minimization case).*

where no stall occurs, the thrust minimization pitch sequence roughly follows that of the power maximization case. It will therefore decrease the thrust where possible and compensate for the corresponding power loss by increasing the power on other azimuthal positions in a similar fashion to the power maximization case. The resulting $C_P - C_T$ curves for both cases have been plotted in Figure 6.22, for a solidity of $\sigma = 0.1$, and it is observed that these curves approach each other for moderate rotor loadings, up to the point where $C_{P,max}$ is reached. Beyond this point, the power maximization curve is, by definition, above the reference curve, whereas the thrust minimization curve is translated downwards and to the left. Also note that the lowest C_P, C_T point can actually be translated both upwards and to the left, implying a possibility of higher power for less thrust at the lowest tip-speed ratio ($\lambda = 2$).

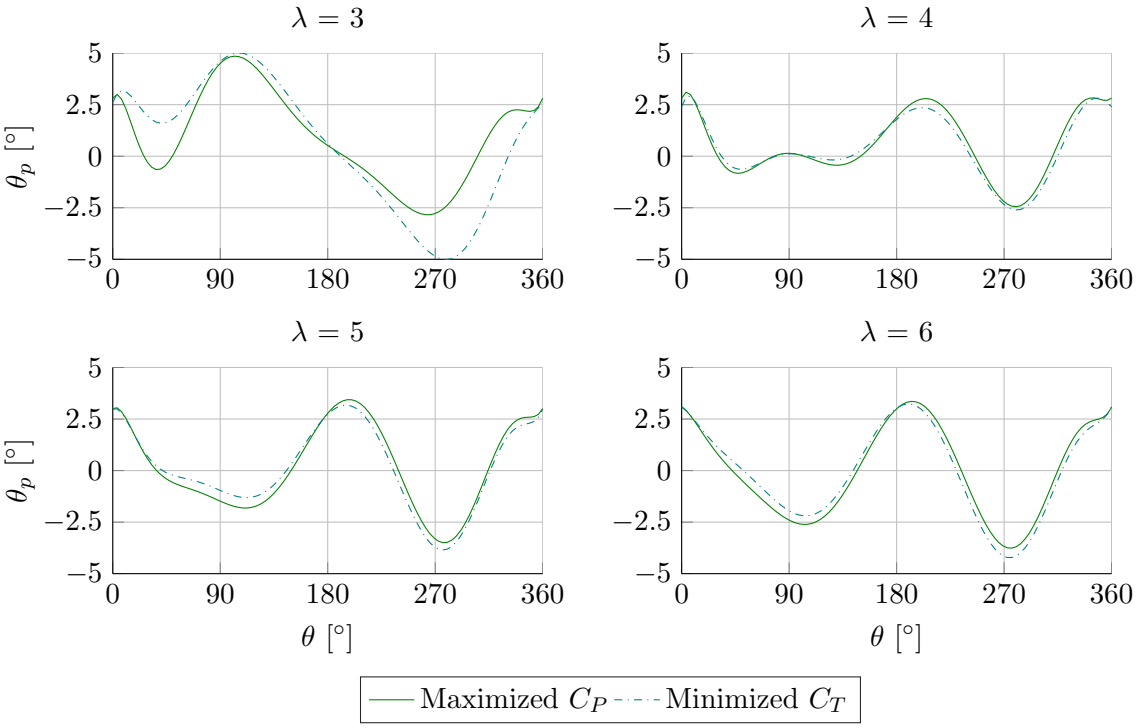

Figure 6.21: *Comparison of maximized C_P and minimized C_T pitch sequences for a rotor with* $\sigma = 0.1$.

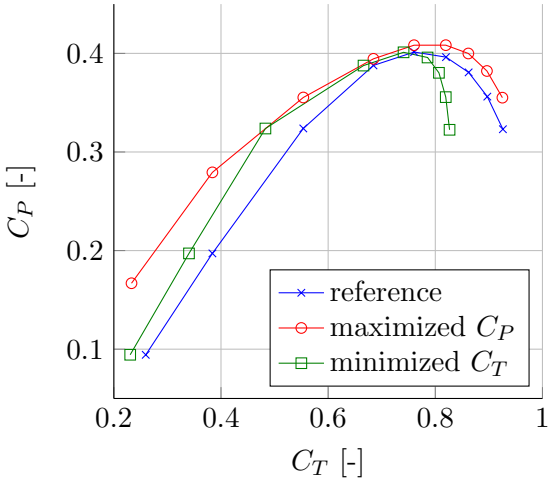

Figure 6.22: *Comparison of maximized C_P and minimized C_T power curves with* $\sigma = 0.1$.

6.2 Impact of unsteady effects on the optimization

In this final section on optimization of the quasi-steady lift and drag coefficients within the direct pitch optimization routine are replaced by their respective unsteady formulations (see equation (4.9) and equation (4.9) in Section 4.1). Since the dynamic coefficients are dependent on their time-history, the routine now has to calculate a time series for every iteration, making the optimizer computationally expensive. For the current unsteady optimization, the model's CPU time is in the order of hours whereas the quasi-steady optimization takes a few minutes only. The necessity of including unsteady effects within the optimization is therefore worth investigating. This section will primarily focus on a comparison between the results of quasi-steady and unsteady optimization. Note that the effect of leading edge separation is excluded here in order to reduce the complexity of the routine. This simplification is justified by the very small impact that the leading edge phenomenon has on the airfoil's aerodynamics, which can be found in Chapter 4. The resulting performance contours and pitch sequences are presented in Appendix C in a similar fashion as the quasi-steady results.

Figure 6.23 shows a single pitch sequence and load distribution for each of the three optimization targets, having maximum pitch allowance ($\pm 10°$). Steady and unsteady optimization are plotted side-to-side to allow for a proper comparison. Starting with the pitch sequences, it is observed that there is a phase shift between the steady and unsteady curve. The phase shift is attributed to the occuring delay of the unsteady aerodynamic loads with respect to the steady ones. Therefore, the unsteady pitch sequence will lag behind the steady curve, as it will encounter the aerodynamic loads at a later instance. A more elaborate description of this lagging phenomenon is given in Section 2.2. For this specific rotor and tip-speed ratio, the phase shifts are quite significant, i.e., $40°$, $45°$ and $20°$ for $C_{P,max}$, $C_{T,min}$ and $C_{P,min}$, respectivily. However, as the reduced frequency decreases, that is, lower λ and σ, the delay between steady and unsteady loads diminishes and therefore the phase shift reduces.

Further observing Figure 6.23 it is visible that the unsteady loading aims at increasing its energy efficiency mainly on the first one-third sector of the rotor ($\theta \in [0°, 120°]$) and compensates for the thrust increase by relieving some loading on the downind side. Similar behaviour is confirmed for other combinations of λ, σ. Apparently the unsteady optimizer recognizes the first $120°$-sector as the only potential for power increasal on a VAWT with an active pitch system. For steady optimization, power gains and thrust compensations are not restricted to specific azimuthal positions. Therefore, a more free interaction between improvements and compensations takes place, yielding a higher potential for power increase. A similar argumentation holds for the thrust minimization case. The power minimization takes place without a constraint on thrust, and is therefore completely free to choose a load distribution of which the integral value is close to zero. Section 6.1 already pointed out that VAWT's are very efficient in reducing their power via an active pitch mechanism. Including unsteady effects within the optimization does not change this potential.

A complete overview of the VAWT's power and thrust potential, both under steady and unsteady optimization, is provided for different rotor solidities in Figure 6.24. The results presented here thus include all three optimization cases. The power and thrust alleviation cases have a negative Δ and the power maximization case is given by the positive values.

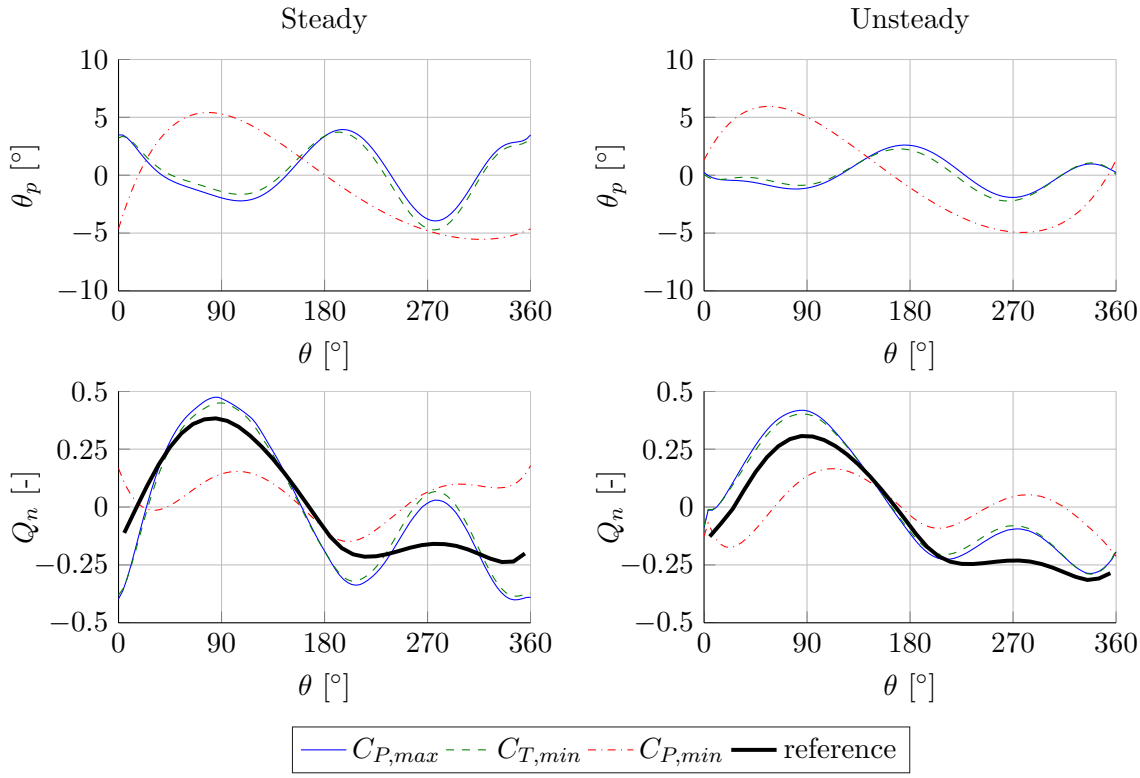

Figure 6.23: *Comparison of pitch sequences and blade loadings under steady and unsteady optimization, with* $\lambda = 5$, $\sigma = 0.12$ *and* $\theta_p \in [-10°;\ 10°]$.

The figure confirms that ignoring unsteady aerodynamic effects throughout the optimization yields a higher estimate for maximum power and minimum thrust potential. Considering the power minimization potential it is visible that, for the tip-speed ratios where $\Delta\, C_P \neq -100\%$, the unsteady optimizer is generally capable of reaching higher power reducals than the steady alternative. This result is to be expected since, next to (viscous) drag, the optimizer can now also utilize the unsteady aerodynamic effects to further reduce the VAWT's efficiency. However, for some rotor solidities at low tip-speed ratios, i.e., $\lambda = 2, 3$, some unexpected results occur in the comparisons of the enhancement potentials, for example: a higher steady power minimization potential at $\lambda = 3$ and $\sigma = 0.06$ and a larger unsteady ΔC_T at $\lambda = 2$ and $\sigma = 0.12$. At low tip-speed ratios the airfoil reaches high angle of attacks and therefore operates within its stall region on some azimuthal intervals. The combination of an unsteady lagging effect on the lift and the airfoil operating in stall makes for an unpredictable optimization, hence the occasional occurance of discrepancies between the expected results and the obtained results at low λ.

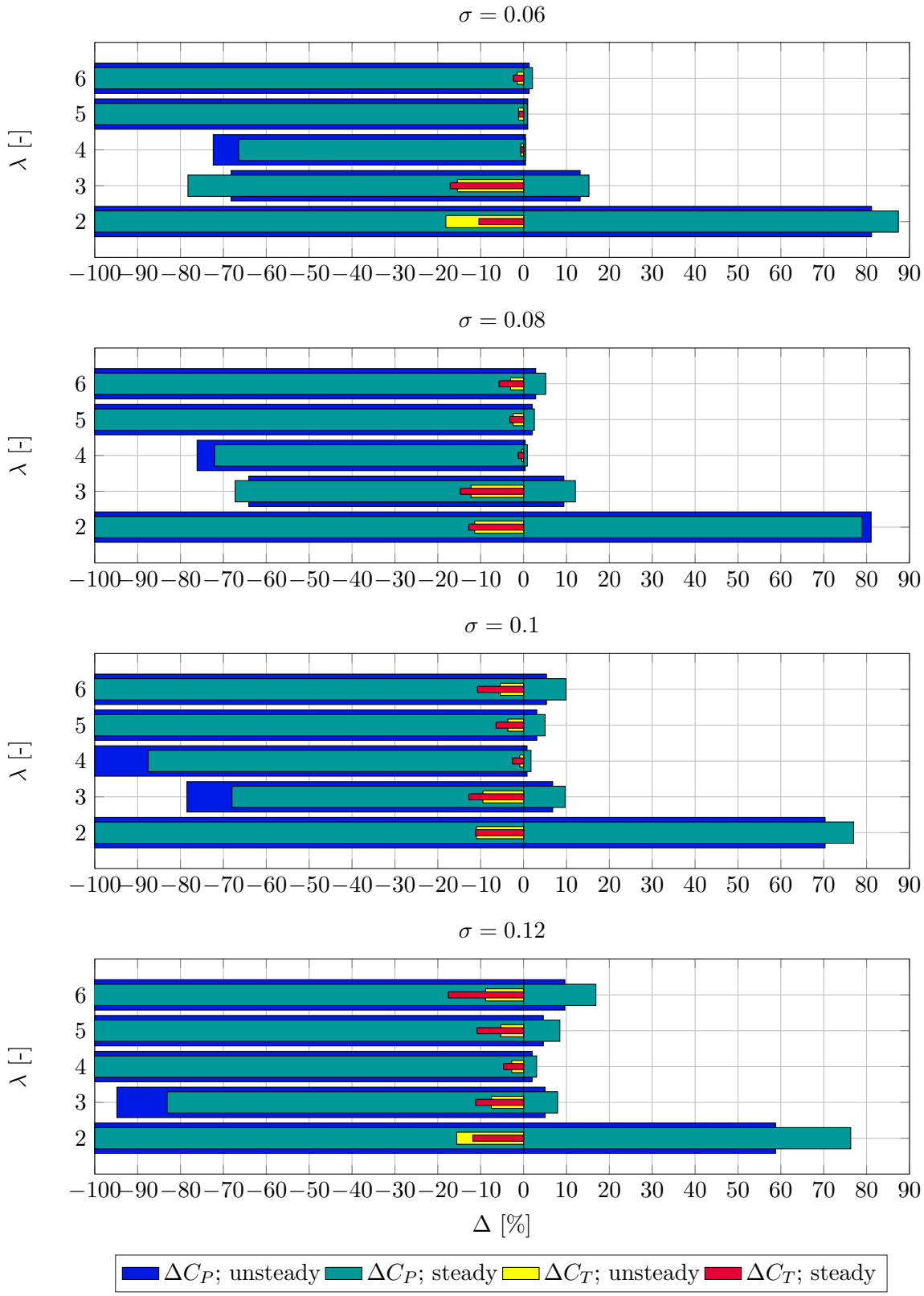

Figure 6.24: *Comparison of power and thrust potential under steady and unsteady optimization, with* $\theta_p \in [-10°;\ 10°]$.

6.3 Chapter conclusions

The primary aim of this chapter was to explore the optimization potential of a VAWT, including the effects of viscosity and drag. Furthermore, the impact of taking unsteady aerodynamics into account during the optimization procedure was investigated. For this purpose, a direct pitch optimizer was implemented in Matlab as this allowed updating the angle of attack accordingly at each iteration step. The main conclusions drawn from this analysis, and their implications on VAWT design and operations, have been listed below.

- The method of direct pitch optimization proves to be an effective method of obtaining feasible, smooth pitch sequences for the various optimization targets. Although it is computationally more expensive than the inverse method, the advantage of being able to directly control the shape of the pitch curve makes this method preferable for investigating the optimization potential under viscous and unsteady flow conditions.

- For the target of power maximization the direct pitch optimizer will expand the optimum operational window rather than increasing the VAWT's maximum power. In practice this means that, for a fixed rotor solidity, the range of tip-speed ratios within which the VAWT's energy extraction is the most efficient is increased with respect to the zero-pitch turbine. One can for instance choose to have the VAWT operating at a relatively low tip-speed ratio to reduce the loadings and thrust, and pitch the blades according to the derived sequences to still have an energy extraction close to the maximum vlaue. Furthermore, a smaller solidity can now be chosen while still achieving the desired power via the active pitch sequence. This reduces the required material for the blades and hence the CoE of the VAWT.

- Unlike the target of power increasal, an active pitch mechanism is very efficient in reducing the power production of a VAWT. For low tip-speed ratios the pitching is such that it acts as a spoiler, driving the airfoil (further) into its stall region. On the other hand, for high tip-speed ratios the pitch sequence practically reduces the absolute value of the angle of attack along the entire circumference, reducing the torque and hence the power. Since there is no constraint, the integral thrust will be reduced simultaneously. An active pitch mechanism therefore proves to be an excellent solution for keeping the VAWT's power below its rated value.

- Optimizing for thrust reduction is only valuable if the reference power is at least maintained. This implies that the power loss due to a local thrust reduction will have to be compensated. The optimizer chooses to perform the power compensation on the most energy efficient part of the rotor, since the required change in loading is minimum here. Therefore, the pitch sequence will roughly follow that of the power maximization case on those intervals. On the remaining azimuthal positions, the optimizer will then have the blade pitching such that it actually minimizes the thrust for as far as the power constraint allows. It is found that a VAWT has potential of somewhat decreasing its thrust at high tip-speed ratios via active pitch control, but only if it has a certain solidity ($\sigma \geq 0.1$).

- Comparing the velocity fields corresponding to the power maximization and minimization cases reveals another optmization target, that is, wake loss minimization. It was found in this chapter that minimizing the VAWT's power extraction from the wind at the same time minimizes the velocity decrease in the wake of the turbine. This implies that, in order to decrease the CoE of a wind farm, there exists an optimum balance between maximum power extraction of a single VAWT and decreasing the wake loss of the respective downwind turbines. It must be noted, though, that this optimization case is not VAWT-specific, as it has extensively been studied for HAWT wind farms already. Exploring this potential for VAWTs is beyond the scope of this thesis since it requires site-dependent statistics on wind strenght and directions, as well as an initial wind farm configuration.

- In order to properly take into account true rotor properties like the number of blades and chord length it is inevitable to consider unsteady aerodynamic effects. In this chapter, an unsteady direct pitch optimization was carried out on three-bladed rotors with different solidities. Overall, it was found that the VAWT's potential for power increasal and thrust reducal decreases with respect to the steady optimization. The reason for this is that the local power can only be increased in the first one-third interval of the rotor's circumference ($\theta \in [0°; 120°]$). On the other hand, reducing the aerodynamic efficiency proves to become easier when taking into account unsteady effects on top of viscosity.

- Dynamic modelling of aerodynamic forces significantly increases the computational effort of the optimizer (from minutes to hours). However, it provides an insight in the optimization potential under unsteady flow conditions due to a finite number of blades; something the quasi-steady optimizer is not capable of.

Chapter 7

Final Remarks

7.1 Conclusions

In this work a new research has been carried out considering active pitch control of a Vertical Active Wind Turbine (VAWT). It was found that this type of circulation control can be very efficient for various optimization targets. The modified-linear (Mod-Lin) Actuator Cylinder Model (ACM) [30] was used as optimization tool, the original version of which utilizes quasi-steady aerodynamic force coefficients. Part of this research was to update these coefficients by a time-series calculation of their dynamic equivalents, for which a Beddoes-Leishman type dynamic stall model was used. Especially the unsteady effect of leading edge separation of an airfoil on a VAWT in operation was a topic that has not extensively been investigated before. Although it was concluded that this specific phenomenon does not have a lot of influence on the VAWT's performance (when using the NACA0018 airfoil), some other interesting results with respect to unsteady aerodynamics and optimization were found, the most relevant of which are listed below.

- Replacing the quasi-steady aerodynamic force coefficients by their dynamic equivalents it is found that the unsteady effects of trailing and leading edge separation are only relevant for lower tip-speed ratios, since the airfoil sometimes operates in its nonlinear region here. In general, unsteady effects become more pronounced when the number of blades is decreased, while maintaining solidity, since the reduced frequency increases.
- The loadform optimization of ideal rotor performance showed that the highest potential in terms of power increase and thrust relief can be found in the area of high λ, σ, that is, where the initial thrust is high. The Mod-Lin ACM, used as optimization tool, is numerically unstable in this region, as it uses a thrust-dependent correction factor. This yields some optimization results that exceed the physical capabilities of a VAWT, such as the Betz limit. It is therefore believed that the optimization results that follow from the loadform optimizer at high loadings will be an overestimiation of the VAWT's true capabilities.

- Comparing the two optimization methods used, loadform optimization and direct pitch optimization, it is found that the former is fast (in the order of seconds) but inconvenient for producing feasible pitch sequences. Direct pitch optimization via Bezier curves is numerically more expensice (in the order of minutes) but allows the user to directly control the limits of the resulting pitch sequences. Pitching the entire blade as a function of azimuthal positions can set large demands on the actuation mechanism, so large oscillations are undesireable. This is why the method of direct pitch optimization via the Mod-Lin ACM is chosen as the main optimization tool in this thesis.

- Using an active pitch mechanism as circulation control method is not effective in increasing the VAWT's maximum power since its impact on the flow characteristics is too crude. Depending on the solidity, the maximum power can be increased up to only $\sim 3\%$ of its initial maximum C_P. For unsteady flow this increase is even less, namely $\sim 2\%$. However, for tip-speed ratios other than the initial optimum λ the pitch mechanism becomes more effective in increasing the VAWT's C_P, which allows the rotor to operate at a different λ and still achieve the initial $C_{P,max}$. The reason why active pitch control is not suited for increasing $C_{P,max}$ is the same reason why it is very effective in reducing the VAWT's power. Depending on λ and σ power alleviations between 70% and 100% are obtained, having a pitch allowance of $\pm 10°$. Unsteady flow effects will only further enhance this behaviour. A large thrust relief also requires a large compensation in terms of power. Therefore a VAWT can alleviate most thrust in those regions where the largest power increases are possible.

- Including the dynamic aerodynamic coefficients within the optimization drastically increases the computational time (from minutes to hours). However, some interesting conclusions can be drawn when analysing results of the unsteady optimization. The first is that the unsteady optimizer aims at increasing the VAWT's local power production only on the rotor section where the angle between the airfoil's chord and the inflow velocity is between $0°$ and $120°$. This is the part where the blade can be pitched for higher aerodynamic gain, without increasing the unsteady and (viscous) drag effects too much. The second is that there is a delaying effect on the obtained pitch sequence due to the response time of unsteady aerodynamic loads. The degree of unsteadiness, i.e., the reduced frequency, determines the magnitude of the delay.

Throughout this thesis and in the above-mentioned conclusion points the results have been referred to as "optimum". This is indeed the case for the chosen and fixed design parameters, such as the applied airfoil, the order of the Bezier polynomial for pitch optimization and the number of blades for the unsteady analysis. These parameters have, for now, been chosen arbitrarily, whereas in reality they have to be included in the design iterations. For instance, a different choice of airfoil might give a higher power maximization potential, but at the same time lead to very significant leading edge separation effects. A higher (or lower) order Bezier polynomial will provide different pitch curve shapes and, therefore, a different optimization potential. The chosen number of blades directly affects the degree of unsteadiness of the optimization. So, yes, the obtained optimum results do prove that there is potential for a VAWT to enhance its performance by active pitch

control, but future research including more design variables and iterations has to point out how significant this potential really is.

7.2 Recommendations

Since the field of VAWT aerodynamic optimization through smart circulation control has not very widely been researched yet, some of the results presented in this thesis will be rather preliminary. This section will present some ideas for future research, in order to further develop the results and verify their actual feasibility on a real VAWT.

- The possibility of an additional modification to the Mod-Lin ACM for highly loaded cases could be investigated. This would be especially relevant when the Mod-Lin ACM is used as optimization tool for an ideal turbine, since the interesting regions for design are those of high loading. For the viscous and unsteady flow cases, the most interesting regions for performance enhancement occur at a lower rotor loading and the Mod-Lin ACM used here will already be an accurate optimization medium.
- Pirrung and Gaunaa [35] suggest certain corrections to the original dynamic stall model, specifically to enhance its accuracy for VAWT applications. Implementation of these corrections will possibly give more accurate results.
- Next to a dynamic stall model, additional aerodynamic models to predict the impact of flow curvature and blade-wake interaction could be investigated to obtain a better insight in the realistic optimization potential of a VAWT with active pitch control.
- A more thorough investigation of the compatibility of the Mod-Lin ACM and the dynamic stall model could be carried out. Focus could, for instance, be on the way both models compute the effective angle of attack, and check whether no double-counting of certain aerodynamic effects occurs.
- Two relatively simple alterations can be made to the direct pitch optimizer that will directly improve its results: 1.) Add an extra constraint to ensure smooth behaviour of the pitch curve on the periodic interval, and 2.) Use a different step size and tolerance for the power maximization case to ensure the optimizer converges towards the global minimum.
- The optimization results shown in this thesis are preliminary in the sense that they are created using an arbitrary active pitch control mechanism. More reliable optimization results will be obtained when the constraints of existing state-of-the-art pitch actuation systems will be used throughout the optimization.
- A verification of the presented optimum pitch sequences should be carried out with a higher-fidelity numerical model.
- Next to the three optimization targets investigated in this thesis, one could think of other interesting desing potentials as well. One example of this has already been revealed in this thesis, i.e., minimizing the VAWT's impact on the velocity field for wind farm optimization. This topic has already been widely researched in the field

of HAWT wind farm optimization. Other optimization targets could be minimizing the angle of attack range (so thicker, more structurally efficient, airfoils could be used) and enhancing the VAWT's self-starting capabilities.

- An investigation into making the optimizer more numerically efficient could be carried out. Now that it is known that the optimum pitch sequences roughly take the form of sinusoidal shapes, the initial guess can be updated such that the routine does not have to create the pitch curves from scratch, reducing the number of required iterations. Additionally, one can look into reducing the computations of the dynamic stall model during the optimization. Perhaps a post-optimization analysis of local power and thrust production will give a similar results. This would, in effect, be the same as treating dynamic stall effects as a correction factor for a finite number of blades.

References

[1] T. S. Beddoes. A Synthesis of Unsteady Aerodynamic Effects Including Stall Hysteresis. *Vertica*, 1, 1976.

[2] D. E. Berg. An improved double-multiple streamtube model for the darrieus type vertical-axis wind turbine. In *In Proceedings of the Sixth Biennial Wind Energy Conference and Workshop*, pages 231–238, Minneapolis, MN, USA, 1 June 1983.

[3] L. Bergami and M. Gaunaa. ATEFlap Aerodynamic Model, a dynamic stall model including the effects of trailing edge flap deflection. Technical report, Risø DTU, February 2012.

[4] L. Bergami, M. Gaunaa, and J. Heinz. Indicial lift response function: an empirical relation for finite-thickness airfoils, and effects on aeroelastic simulations. *Wind Energy*, 2012.

[5] H. Beri and Y. Yao. Double Multiple Stream Tube Model and Numerical Analysis of Vertical Axis Wind Turbine. *Energy and Power Engineering*, pages 262–270, 2011.

[6] R. L. Bielawa. Synthesized Unsteady Airfoil Data with Applications to Stall Flutter Calculations. In *31st Annual Forum of the American Helicopter Society*, Washington DC, May 13-15 1975.

[7] R. E. Brown. Rotor Wake modelling for Flight Dynamic Simulation of Helicopters. *AIAA Journal*, pages 57–63, 2000.

[8] F. O. Carta and N. D. Ham. An Analysis of the Stall Flutter Instability of Helicopter Rotor Blades. *Journal of the American Helicopter Society*, 12(4), 1967.

[9] M. Drela. XFOIL: An Analysis and Design System for Low Reynolds Number Airfoils. Technical report, MIT Dept. of Aeronautics and Astronautics, Cambridge, Massechusetts, 1989.

[10] E. Dyachuk and A. Goude. Simulating Dynamic Stall Effects for Vertical Axis Wind Turbines Applying a Double Multiple Streamtube Model. *Energies*, February 215.

[11] E. Dyachuk, A. Goude, and H. Bernhoff. Dynamic Stall Modeling for the Conditions of Vertical Axis Wind Turbines. *AIAA Journal*, 52(1), 2014.

[12] EWEA. The European Wind Initiative - Wind Power Research and Development to 2020. Technical report, European Wind Energy Association, 2013.

[13] EWETP. Strategic Research Agenda - Market Deployment Strategy. Technical report, European Wind Energy Technology Platform, 2014.

[14] C. J. Simão Ferreira, H. Aa. Madsen, M. Barone, B. Roscher, P. Deglaire, and I. Arduin. Comparison of aerodynamic models for Vertical Axis Wind Turbines. *TORQUE*, 2014.

[15] C. Simão Ferreira. *The near wake of the VAWT: 2D and 3D views of the VAWT aerodynamics*. PhD thesis, Delft University of Technology, 2009.

[16] C. Simão Ferreira and F. Scheurich. Demonstrating that power and instantaneous loads are decoupled in a vertical-axis wind turbine. *Wind Energy*, 2014.

[17] E. Ferrer and R. H. J. Willden. Blade-wake interactions in cross-flow turbines. *International Journal of Marine Energy*, pages 71–83, June 2015.

[18] S. T. Gangwani. Synthesized Airfoil Data Method for Prediction of Dynamic Stall and Unsteady Airloads. *Vertica*, 1(2), 1984.

[19] R. E. Gormont. A Mathematical Model of Unsteady Aerodynamics and Radial Flow for Application to Helicopter Rotors. Technical report, U.S. Army Air Mobility Research and Development Laboratory, 1973. USAAVLABS TR 72-67.

[20] D. W. Gross and F. D. Harris. Prediction of In-Flight Stalled Airloads from Oscillating Airfoil Data. In *25th Annual Forum of the American Helicopter Society*, Washington DC, May 14-16 1969.

[21] M. H. Hansen, M. Gaunaa, and H.A. Madsen. A Beddoes-Leishman type dynamic stall model in state-space and indicial formulations. Technical report, Technical University of Denmark, 2004.

[22] M. Islam, D. S.-K. Ting, and A. Fartaj. Aerodynamic models for Darrieus-type straight-bladed vertical axis wind turbines. *Elsevier*, 2006.

[23] W. Johnson. Comparison of Three Methods for Calculation of Helicopter Rotor Blade Loading and Stresses Due to Stall. Technical report, NASA, 1974.

[24] J. Katz and A. Plotkin. *Low-Speed Aerodynamics*. McGraw-Hill, Inc., 1991.

[25] l. Paraschivoiu. Aerodynamic Loads and Performance of the Darrieus Rotor. *Journal of Energy*, 6(6):406–412, 1981.

[26] J. W. Larsen, S. R. K Nielsen, and S. Krenk. Dynamic stall model for wind turbine airfoils. *Elsevier*, 2007.

[27] J. G. Leishman. *Principles of Helicopter Aerodynamics*. Cambridge University Press, 2000.

[28] J. G. Leishman. Challenges in Modeling the Unsteady Aerodynamics of Wind Turbines. In *Proceedings of the 21st ASME Wind Energy Symposion and the 40th AIAA Aerospace Science Meeting*. American Institute of Aeronautics and Astronautics, 2002. AIAA 2002-0037.

[29] J. G. Leishman and T. S. Beddoes. A Semi-Empirical Model for Dynamic Stall. *Journal of the American Helicopter Society*, 34(3):3–17, 1989.

[30] H. Aa. Madsen. *The Actuator Cylinder - A Flow Model for Vertical Axis Wind Turbines*. PhD thesis, Aalborg University, 9100 Aalborg, Denmark, January 1982.

[31] H. Aa. Madsen, U. S. Paulsen, and L. Vitae. Analysis of VAWT aerodynamics and design using the Actuator Cylinder flow model. In *Proceedings of Torque 2012 : The science of making torque from wind*, 2012.

[32] H. Aa. Madsen, T. J. Larsen, U. S. Paulsen, and L. Vita. Implementation of the Actuator Cylinder Flow model in the HAWC2 code for Aeroelastic Simulations on Vertical Axis Wind Turbines. In *Proceedings of the 51st AIAA Aerospace Sciences Meeting including the New Horizons Forum and Aerospace Exposition*. American Institute of Aeronautics and Astronautics, 2014. AIAA 2013-0913.

[33] P. G. Migliore, W. P. Wolfe, and J. B. Fanucci. Flow Curvature Effects on Darrieus Turbine Blade Aerodynamics. *Journal of Energy*, 4(2):49–55, 1980.

[34] J. C. Murray and M. Barone. The Development of CACTUS, a Wind and Marine Turbine Performance Simulation Code. In *Proceedings of the 49th AIAA Aerospace Sciences Meeting including the New Horizons Forum and Aerospace Exposition*. American Institute of Aeronautics and Astronautics, 2014. AIAA 2011-147.

[35] G. R. Pirrung and M. Gaunaa. Dynamic stall model modifications to improve the modeling of vertical axis wind turbines. Technical report, April 2016.

[36] N. Ramos-García, A. Cayron, and J. Nørkaer Sørensen. Unsteady Double Wake Model for the Simulation of Stalled Airfoils. *Journal of Power and Energy Engineering*, 2015.

[37] F. Scheurich, T. M. Fletcher, and R. E. Brown. Simulating the aerodynamic performance and wake dynamics of a vertical-axis wind turbine. *Wind Energy*, pages 159–177, 2011.

[38] W. Sheng, R. A. McD. Galbraith, and F. N. Coton. A Modified Dynamic Stall Model for Low Mach Numbers. *Journal of Solar Energy Engineering*, 130, 2008.

[39] J. H. Strickland. The Darrieus Turbine: A Performance Prediction Model Using Multiple Stream Tubes. Technical report, Sandia National Laboratories, 1975. SAND75-041.

[40] J. H. Strickland, B. T. Webster, and T. Nuygen. Vortex Model of the Darrieus Turbine: An Analytical and Experimental Study. Technical report, Sandia National Laboratories, 1981.

[41] R. J. Templin. Aerodynamic Performance Theory for the NRC Vertical-Axis Wind Turbine. Technical report, National Research Council of Canada, 1974. LTR- LA-160.

[42] T. Theodorsen. General Theory of Aerodynamic Instability and the Mechanism of Flutter. Technical Report NACA 496, 1935.

[43] B. Thwaites. *Incompressible Aerodynamics*. Clarendon Press, Oxford, 1960.

[44] C. T. Tran and D. Petot. Semi-Empirical Model for the Dynamic Stall of Airfoils in View of the Application to the Calculation of the Responses of a Helicopter Blade in Forward Flight. *Vertica*, 5(1), 1981.

[45] VISCWIND. Viscous effects on wind turbine blades, final report on the JOR3-CT95-0007, Joule III project. Technical report, Technical University of Denmark, 1999.

[46] L. Vita. *Offshore Vertical Axis Wind Turbine with Floating and Rotating Foundation*. PhD thesis, Technical University of Denmark, 2011.

[47] A. Zanon, P. Giannattasio, and C. J. Simão. A vortex panel model for the simulation of the wake flow past a vertical axis wind turbine in dynamic stall. *Wind Energy*, 2012.

Appendix A

NACA0018 Airfoil Polar

Table A.1: *NACA0018 lift, drag moment polar data for $Re = 3\ 000\ 000$, created at Risø*.*

α [°]	C_l [-]	C_d [-]	C_m [-]	α [°]	C_l [-]	C_d [-]	C_m [-]
-180.0	0.0000	0.0250	0.0000	0.0	0.0000	0.0071	0.0000
-175.0	0.1560	0.0557	-0.2000	0.5	0.0495	0.0072	0.0004
-170.0	0.7366	0.1576	-0.4000	1.0	0.0992	0.0074	0.0009
-160.0	0.5503	0.3298	-0.3250	1.5	0.1485	0.0079	0.0014
-140.0	0.980	0.930	-0.325	2.0	0.1978	0.0085	0.0020
-120.0	0.896	1.450	-0.325	2.5	0.2471	0.0092	0.0026
-110.0	0.665	1.625	-0.325	3.0	0.2960	0.0101	0.0032
-100.0	0.354	1.746	-0.325	3.5	0.3444	0.0112	0.0039
-93.2	0.115	1.794	-0.325	4.0	0.3928	0.0125	0.0047
-90.0	0.000	1.800	-0.325	4.5	0.4408	0.0139	0.0056
-80.0	-0.354	1.780	-0.325	5.0	0.4882	0.0155	0.0066
-70.0	-0.665	1.660	-0.325	5.5	0.5351	0.0173	0.0078
-60.0	-0.896	1.500	-0.293	6.0	0.5812	0.0191	0.0090
-50.0	-1.020	1.200	-0.260	6.5	0.6267	0.0212	0.0105
-45.0	-1.050	1.040	-0.240	7.0	0.6708	0.0233	0.0123
-35.0	-0.980	0.703	-0.200	7.5	0.7140	0.0256	0.0143
-30.0	-0.855	0.454	-0.180	8.0	0.7588	0.0281	0.0158
-20.0	-0.8875	0.1619	0.0030	8.5	0.8067	0.0310	0.0164
-19.5	-0.8910	0.1535	-0.0015	9.0	0.8609	0.0345	0.0154
-19.0	-0.8981	0.1442	-0.0065	9.5	0.9116	0.0379	0.0151
-18.5	-0.9211	0.1337	-0.0140	10.0	0.9614	0.0416	0.0148
-18.0	-0.9428	0.1240	-0.0204	10.5	0.9811	0.0437	0.0204
-17.5	-0.9629	0.1149	-0.0260	11.0	1.0009	0.0459	0.0258
-17.0	-0.9983	0.1052	-0.0321	11.5	1.0181	0.0477	0.0322
-16.5	-1.0308	0.0963	-0.0372	12.0	1.0472	0.0509	0.0348
-16.0	-1.0583	0.0883	-0.0411	12.5	1.0616	0.0538	0.0388
-15.5	-1.0797	0.0813	-0.0438	13.0	1.0814	0.0572	0.0414
-15.0	-1.0932	0.0752	-0.0454	13.5	1.0942	0.0609	0.0437
-14.5	-1.0957	0.0700	-0.0458	14.0	1.0969	0.0652	0.0452
-14.0	-1.0969	0.0652	-0.0452	14.5	1.0957	0.0700	0.0458
-13.5	-1.0942	0.0609	-0.0437	15.0	1.0932	0.0752	0.0454
-13.0	-1.0814	0.0572	-0.0414	15.5	1.0797	0.0813	0.0438
-12.5	-1.0616	0.0538	-0.0388	16.0	1.0583	0.0883	0.0411
-12.0	-1.0472	0.0509	-0.0348	16.5	1.0308	0.0963	0.0372
-11.5	-1.0181	0.0477	-0.0322	17.0	0.9983	0.1052	0.0321
-11.0	-1.0009	0.0459	-0.0258	17.5	0.9629	0.1149	0.0260
-10.5	-0.9811	0.0437	-0.0204	18.0	0.9428	0.1240	0.0204
-10.0	-0.9614	0.0416	-0.0148	18.5	0.9211	0.1337	0.0140
-9.5	-0.9116	0.0379	-0.0151	19.0	0.8981	0.1442	0.0065
-9.0	-0.8609	0.0345	-0.0154	19.5	0.8760	0.1552	-0.0015
-8.5	-0.8067	0.0310	-0.0164	20.0	0.8725	0.1651	-0.0060
-8.0	-0.7588	0.0281	-0.0158	30.0	0.855	0.454	-0.180
-7.5	-0.7140	0.0256	-0.0143	35.0	0.980	0.703	-0.200
-7.0	-0.6708	0.0233	-0.0123	45.0	1.050	1.040	-0.240
-6.5	-0.6267	0.0212	-0.0105	50.0	1.020	1.200	-0.260
-6.0	-0.5812	0.0191	-0.0090	60.0	0.896	1.500	-0.293
-5.5	-0.5351	0.0173	-0.0078	70.0	0.665	1.660	-0.325
-5.0	-0.4882	0.0155	-0.0066	80.0	0.354	1.780	-0.325
-4.5	-0.4408	0.0139	-0.0056	90.0	0.000	1.800	-0.325
-4.0	-0.3928	0.0125	-0.0047	93.2	-0.115	1.794	-0.325
-3.5	-0.3444	0.0112	-0.0039	100.0	-0.354	1.746	-0.325
-3.0	-0.2960	0.0101	-0.0032	110.0	-0.665	1.625	-0.325
-2.5	-0.2471	0.0092	-0.0026	120.0	-0.896	1.450	-0.325
-2.0	-0.1978	0.0085	-0.0020	140.0	-0.980	0.930	-0.325
-1.5	-0.1485	0.0079	-0.0014	160.0	-0.5504	0.3298	-0.3250
-1.0	-0.0992	0.0074	-0.0009	170.0	-0.7367	0.1576	-0.4000
-0.5	-0.0495	0.0072	-0.0004	175.0	-0.1560	0.0557	-0.2000
0.0	0.0000	0.0071	0.0000	180.0	0.0000	0.0250	0.0000

*0° to 30°: from XFOIL, 35° to 40°: flat plate measurements, 40° to 180°: baseline "high angle of attack" dataset, -180° to 0°: mirrored $0^\circ - 180^\circ$

Appendix B

Optimization Results

Table B.1: *Optimization results for the ideal rotor, with* $f_{\Delta Q_n}^{\text{local}} = 50\%$.

(λ, σ) [-]	$C_{P,max}$ [-]	$C_{P,min}$ [-]	$C_{T,min}$ [-]	ΔC_P [%]	ΔC_T [%]
$(2, 0.06)$	0.306	0.282	0.334	$[1.04, -6.96]$	-0.91
$(3, 0.06)$	0.412	0.376	0.472	$[1.29, -7.56]$	-1.09
$(4, 0.06)$	0.490	0.435	0.587	$[1.68, -9.71]$	-1.53
$(5, 0.06)$	0.540	0.481	0.676	$[1.58, -9.51]$	-2.77
$(6, 0.06)$	0.573	0.503	0.744	$[1.85, -10.5]$	-3.96
$(2, 0.08)$	0.380	0.339	0.425	$[1.67, -9.08]$	-1.16
$(3, 0.08)$	0.487	0.432	0.584	$[1.41, -9.94]$	-1.74
$(4, 0.08)$	0.552	0.486	0.700	$[1.74, -72.0]$	-3.07
$(5, 0.08)$	0.586	0.506	0.773	$[2.17, -11.9]$	-5.37
$(6, 0.08)$	0.598	0.500	0.810	$[2.09, -14.7]$	-8.47
$(2, 0.10)$	0.437	0.379	0.504	$[1.59, -11.9]$	-1.96
$(3, 0.10)$	0.537	0.461	0.673	$[1.63, -12.9]$	-2.72
$(4, 0.10)$	0.585	0.489	0.771	$[2.04, -14.7]$	-5.43
$(5, 0.10)$	0.602	0.495	0.808	$[2.60, -15.5]$	-9.86
$(6, 0.10)$	0.604	0.515	0.801	$[2.86, -12.3]$	-15.5
$(2, 0.12)$	0.484	0.405	0.577	$[1.88, -14.8]$	-2.16
$(3, 0.12)$	0.571	0.473	0.735	$[2.11, -15.4]$	-4.42
$(4, 0.12)$	0.600	0.496	0.804	$[2.58, -15.2]$	-8.83
$(5, 0.12)$	0.604	0.530	0.802	$[2.91, -9.62]$	-15.4
$(6, 0.12)$	0.603	0.529	0.906	$[3.49, -9.27]$	-8.01

Table B.2: *Optimization results for steady flow, with* $\theta_{p,range} = \pm 10°$.

(λ, σ) [-]	$C_{P,max}$ [-]	$C_{P,min}$ [-]	$C_{T,min}$ [-]	ΔC_P [%]	ΔC_T [%]
$(2, 0.06)$	0.106	0.000	0.142	$[87.4, -100]$	-10.4
$(3, 0.06)$	0.240	0.045	0.281	$[15.3, -78.3]$	-17.1
$(4, 0.06)$	0.326	0.109	0.526	$[0.48, -66.4]$	-0.66
$(5, 0.06)$	0.355	0.000	0.635	$[0.88, -100]$	-1.14
$(6, 0.06)$	0.354	0.000	0.708	$[2.09, -100]$	-2.40
$(2, 0.08)$	0.135	0.000	0.183	$[78.9, -100]$	-12.8
$(3, 0.08)$	0.303	0.089	0.383	$[12.1, -67.3]$	-14.7
$(4, 0.08)$	0.378	0.105	0.651	$[0.89, -72.0]$	-1.25
$(5, 0.08)$	0.389	0.000	0.746	$[2.52, -100]$	-3.21
$(6, 0.08)$	0.364	0.000	0.799	$[5.16, -100]$	-5.73
$(2, 0.10)$	0.167	0.000	0.231	$[77.0, -100]$	-11.2
$(3, 0.10)$	0.355	0.104	0.483	$[9.70, -68.0]$	-12.8
$(4, 0.10)$	0.408	0.050	0.741	$[1.73, -87.5]$	-2.60
$(5, 0.10)$	0.400	0.000	0.807	$[5.03, -100]$	-6.43
$(6, 0.10)$	0.355	0.000	0.827	$[9.91, -100]$	-10.7
$(2, 0.12)$	0.199	0.000	0.272	$[76.3, -100]$	-11.8
$(3, 0.12)$	0.395	0.062	0.576	$[7.94, -83.1]$	-11.2
$(4, 0.12)$	0.423	0.000	0.801	$[3.05, -100]$	-4.66
$(5, 0.12)$	0.399	0.000	0.824	$[8.46, -100]$	-10.9
$(6, 0.12)$	0.334	0.000	0.804	$[16.9, -100]$	-17.5

Table B.3: *Optimization results for unsteady flow, with* $\theta_{p,range} = \pm 10°$.

(λ, σ) [-]	$C_{P,max}$ [-]	$C_{P,min}$ [-]	$C_{T,min}$ [-]	ΔC_P [%]	ΔC_T [%]
$(2, 0.06)$	0.105	0.000	0.128	$[81.2, -100]$	-18.1
$(3, 0.06)$	0.235	0.066	0.286	$[13.2, -68.2]$	-15.4
$(4, 0.06)$	0.315	0.087	0.520	$[0.45, -72.4]$	-0.63
$(5, 0.06)$	0.340	0.000	0.624	$[0.98, -100]$	-1.18
$(6, 0.06)$	0.335	0.000	0.707	$[1.30, -100]$	-1.46
$(2, 0.08)$	0.141	0.000	0.183	$[81.1, -100]$	-11.4
$(3, 0.08)$	0.292	0.096	0.394	$[9.40, -64.1]$	-12.2
$(4, 0.08)$	0.357	0.085	0.646	$[0.38, -76.1]$	-0.44
$(5, 0.08)$	0.362	0.000	0.738	$[2.00, -100]$	-2.43
$(6, 0.08)$	0.329	0.000	0.814	$[2.83, -100]$	-3.03
$(2, 0.10)$	0.168	0.000	0.227	$[70.3, -100]$	-11.0
$(3, 0.10)$	0.334	0.067	0.500	$[6.79, -78.5]$	-9.48
$(4, 0.10)$	0.375	0.000	0.739	$[0.81, -100]$	-0.88
$(5, 0.10)$	0.357	0.000	0.816	$[3.08, -100]$	-3.67
$(6, 0.10)$	0.300	0.000	0.868	$[5.34, -100]$	-5.44
$(2, 0.12)$	0.189	0.000	0.256	$[58.8, -100]$	-15.6
$(3, 0.12)$	0.363	0.018	0.596	$[5.03, -94.8]$	-7.50
$(4, 0.12)$	0.377	0.000	0.798	$[1.99, -100]$	-2.76
$(5, 0.12)$	0.338	0.000	0.863	$[4.61, -100]$	-5.30
$(6, 0.12)$	0.260	0.000	0.884	$[9.64, -100]$	-8.86

Appendix C

Results of unsteady direct pitch optimization

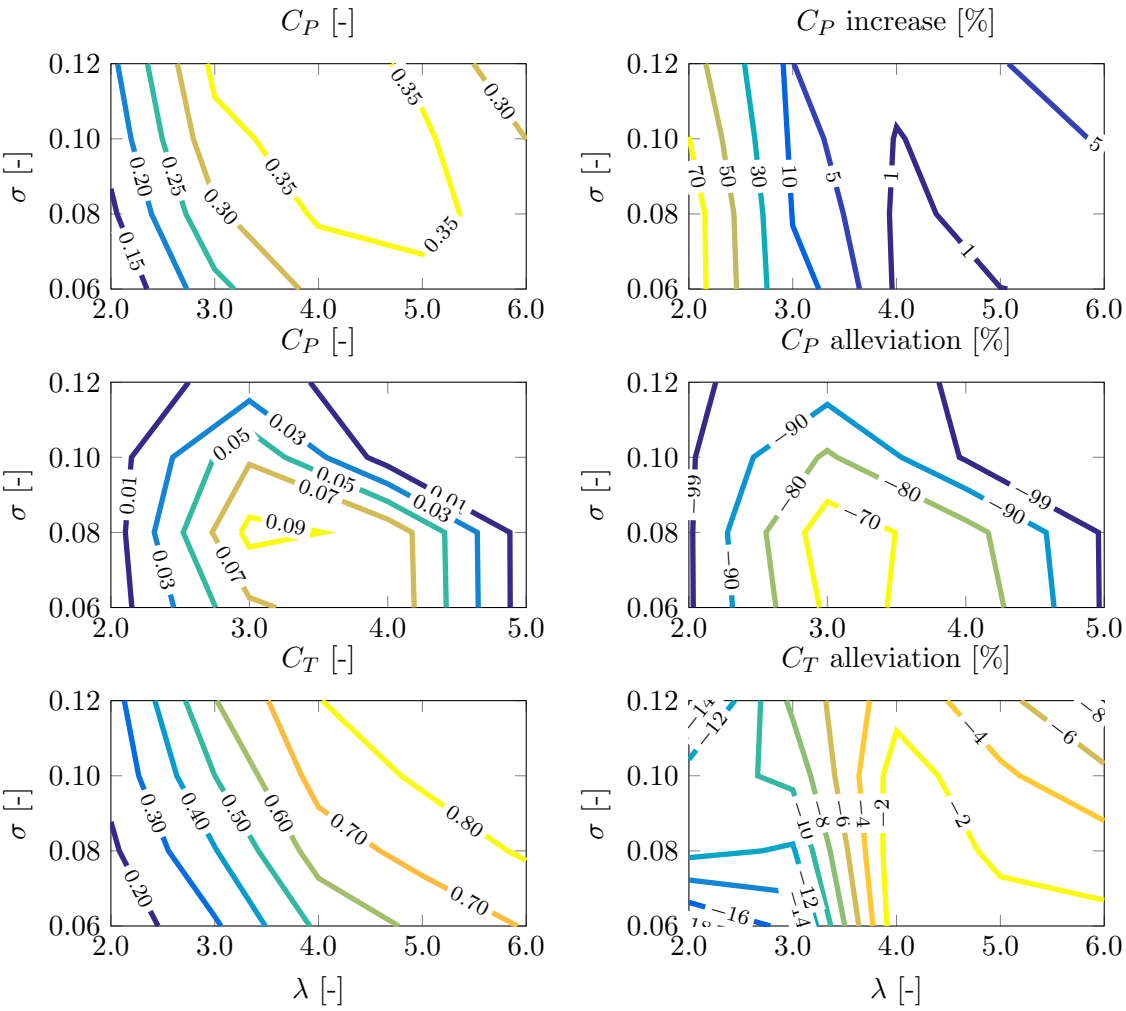

Figure C.1: *Unsteady optimization results with $\theta_p \in [-10°; 10°]$; power maximization (top row), power minimization (middle row), thrust minimization (bottom row).*

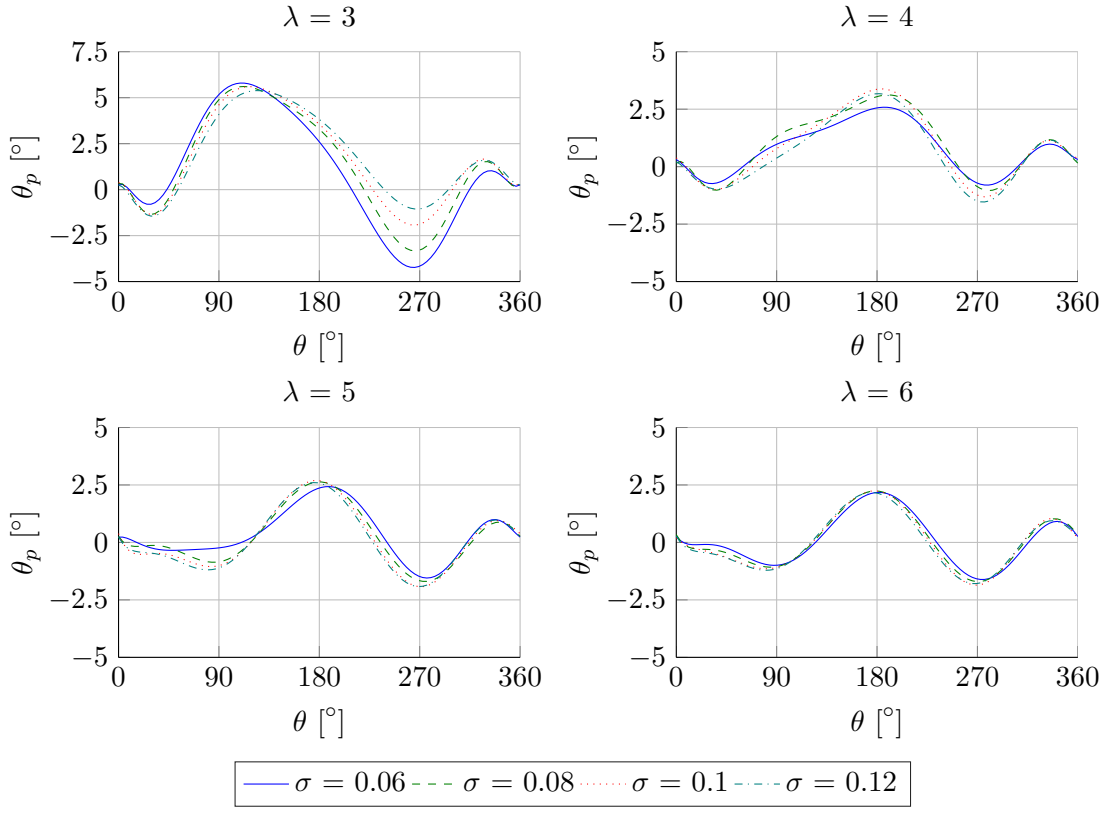

Figure C.2: *Required pitch sequences to obtain maximum power.*

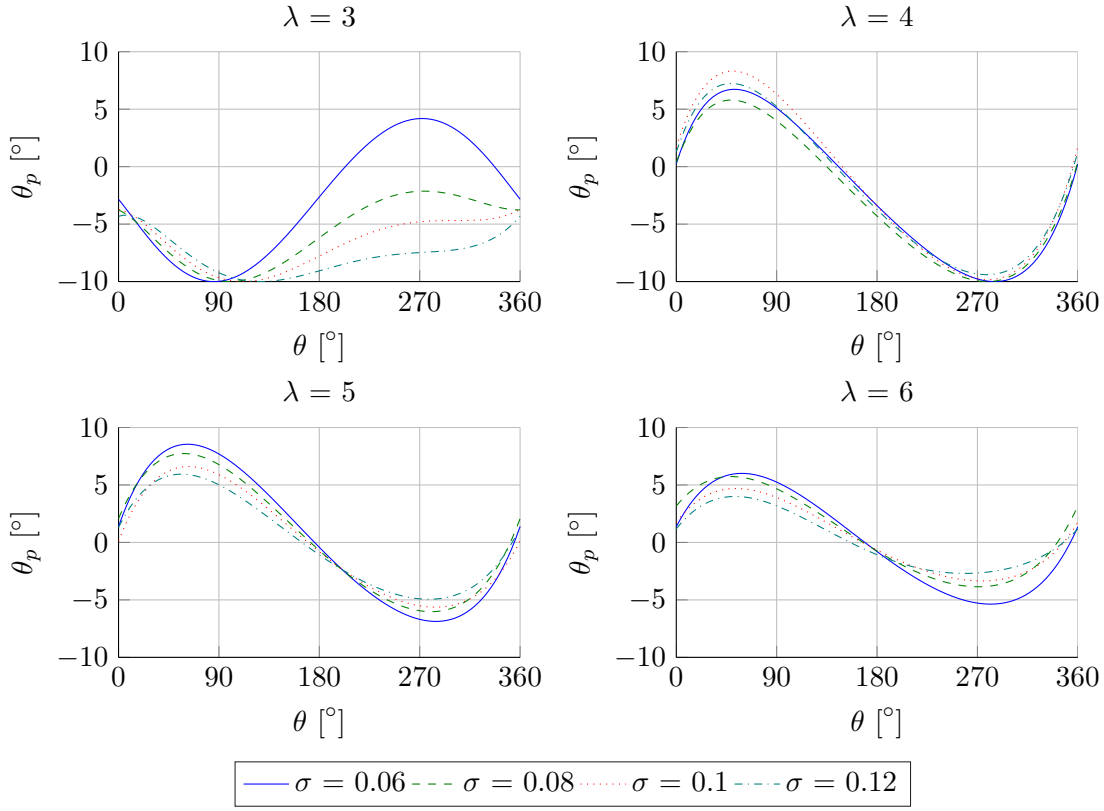

Figure C.3: *Required pitch sequences to obtain minimum power.*

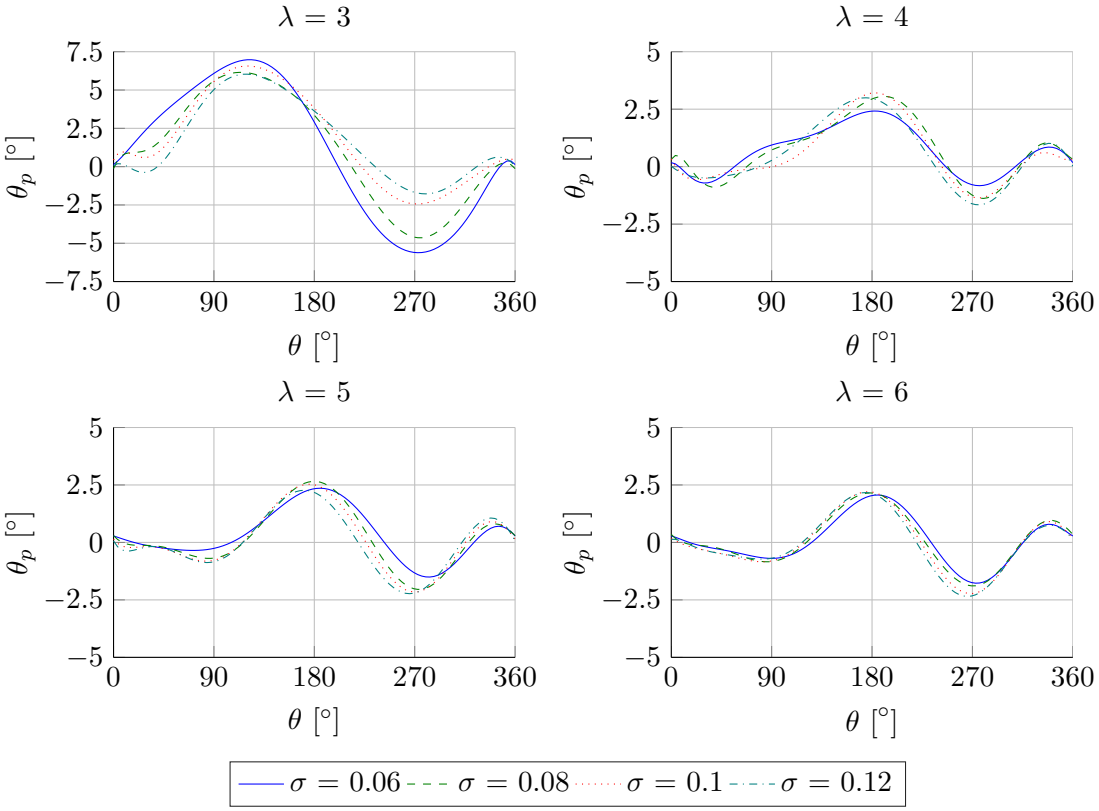

Figure C.4: *Required pitch sequences to obtain mimimum thrust.*